THE POTENTIAL OF USING NATURAL GAS IN HCCI ENGINES:

RESULTS FROM ZERO- AND MULTI-DIMENSIONAL

SIMULATIONS

A Dissertation

by

JUNNIAN ZHENG

Submitted to the Office of Graduate Studies of
Texas A&M University
in partial fulfillment of the requirements for the degree of

DOCTOR OF PHILOSOPHY

May 2012

Major Subject: Mechanical Engineering

THE POTENTIAL OF USING NATURAL GAS IN HCCI ENGINES:

RESULTS FROM ZERO- AND MULTI-DIMENSIONAL

SIMULATIONS

A Dissertation

by

JUNNIAN ZHENG

Submitted to the Office of Graduate Studies of
Texas A&M University
in partial fulfillment of the requirements for the degree of

DOCTOR OF PHILOSOPHY

Approved by:

Chair of Committee,	Jerald A. Caton
Committee Members,	Timothy J. Jacobs
	Eric L. Petersen
	Adonios N. Karpetis
Head of Department,	Jerald A. Caton

May 2012

Major Subject: Mechanical Engineering

ABSTRACT

The Potential of Using Natural Gas in HCCI Engines: Results from Zero- and

Multi-Dimensional Simulations. (May 2012)

Junnian Zheng, B.A., Shanghai Jiao Tong University;

M.S., Texas A&M University

Chair of Advisory Committee: Dr. Jerald A. Caton

With the depletion of petroleum based fuels and the corresponding concerns of national energy security issues, natural gas as an alternative fuel in IC engine applications has become an attractive option. Natural gas requires minimum mixture preparation, and is chemically stable, both of which make it a suitable fuel for homogeneous charged compression ignition (HCCI) engines. Compared to petroleum based fuels, natural gas produces less green-house emissions. However, natural gas is hard to auto-ignite and therefore requires a higher compression ratio, some amount of intake heating, or some type of pre-ignition. In addition, natural gas usually has large differences in fuel composition from field to field, which adds more uncertainties for engine applications.

The current study determines the auto-ignition characteristics, engine performance, and nitric oxides emissions as functions of major operating parameters for a natural gas fueled HCCI engine, and determines differences relative to gasoline fueled HCCI engines which have been studied for many years. These tasks have been done using both zero- and

multi-dimensional engine simulations.

By zero-dimensional simulation, the effects of varying equivalence ratios, engine speeds, compression ratio, EGR level, intake pressure and fuel compositions are determined and analyzed in detail. To be able to account for the in-cylinder inhomogeneous effect on the HCCI combustion, multi-zone models coupled with cold-flow CFD simulations are employed in addition to the single-zone model. The effects of non-homogeneous temperature and equivalence ratio stratification on the ignition timing, combustion phasing, and emissions formation have been studied and discussed. Finally, the preliminary two-dimensional axial-symmetric CFD simulations have been conducted to study the in-cylinder temperature and the species distributions, which provide better visualization of the natural gas auto-ignition process.

DEDICATION

I dedicate this dissertation to my parents, who supported me each step of the way.

ACKNOWLEDGMENTS

I wish to express my deep appreciation to my committee chair, Dr. Jerald Caton, for his constant guidance and support throughout this work. I am very grateful to Dr. Timothy Jacobs who gave me a lot of insight on the experimental side. I would also like to thank Dr. Eric Petersen and Dr. Adonios Karpetis, for their encouragement and support of my dissertation work.

Finally, I want to express my gratitude to Josh, Brandon, Jiafeng, and my other colleagues in the engine lab for their continued support and inspiring ideas on my research work.

TABLE OF CONTENTS

LIST OF FIGURES

LIST OF TABLES

1. INTRODUCTION

Reciprocating internal combustion engines, since their invention and first wide use in the 19th century, have been utilized in ground transportation, marine, power generation, and other applications for over 200 years. Two major types of internal combustion engine are: spark-ignition (SI) engines where the combustion is initiated by a spark and compression-ignition (CI) engines or diesel engines where combustion is initiated by the auto-ignition of the high temperature and high pressure fuel and air mixture. Although both SI and CI engines with petroleum based fuel (typically gasoline and diesel) have been remarkably successful as prime movers in different applications, with the increasing needs for more efficient and lower emission engines, many novel engine concepts have been brought out and studied extensively. In addition, with the increasing cost for petroleum based fuel, tremendous effort to search for alternative fuels has been made in the past several decades. In this section, a brief introduction is provided for the HCCI engine concept and the use of natural gas as an alternative fuel.

This dissertation follows the style of *Journal of Automobile Engineering*.

1.1 Brief overview of HCCI engines

HCCI (homogeneous charge compression ignition) is a very desirable combustion mode which combines the advantages of CI and SI engines: low emissions and high efficiency. In a typical HCCI combustion, fuel is premixed with air before getting into the cylinder by port fuel injection, and then the air fuel mixture is compressed during the compression stroke. Once the mixture reaches its auto-ignition limit, it ignites automatically without the help of spark plug or high pressure injection. The benefits of HCCI combustion include: (1) reduced NO_x emission, since the air/fuel mixture could be very lean in HCCI operations which lowers the peak temperature and thus reduces NO_x production, (2) reduced soot, since there are fewer fuel rich zones in the homogeneous mixture, (3) high thermal efficiency due to several reasons. First, a lean mixture has a relatively higher ratio of specific heats. Secondly, no flame propagation prevents end gas knock and enables the use of higher compression ratio. Third, throttless operation reduces the pumping loss at low load conditions. Forth, there is less in-cylinder heat transfer due to the lower temperature and fast combustion, and finally quick heat release of HCCI combustion ensures the majority of the heat release could occur just after TDC which is closer to the ideal Otto cycle.

However, HCCI engines also face a few challenges. First of all, the biggest challenge of the HCCI engines is the control of the combustion phasing without direct control on the auto-ignition process. Secondly, the auto-ignition process is sensitive to many factors such as intake air temperature and pressure, EGR level, and fuel composition

which make control even more difficult. Third, the operating range of HCCI engines is limited because the high rate of heat release for HCCI combustion creates high intensity of noise and higher potential of knocking, which limits the highest attainable load. Too lean mixture leads to misfire which determines the lower limit of load. In addition, relatively higher unburned hydrocarbon (UHC) and carbon monoxide (CO) emissions are observed resulting from the low combustion temperature and corresponding incomplete oxidations. Furthermore, there is potentially high cycle-by-cycle and cylinder-to-cylinder variations in HCCI engines due to the difficulties in controlling the combustion phasing.

1.2 Natural gas and its application in HCCI engines

Natural gas is a naturally occurring gas mixture which consists of primarily methane and some amount of higher hydrocarbons, nitrogen, and carbon dioxides. Typical composition of a commercial natural gas product is shown in Figure 1. According to the Energy Information Agency's report [1], the world had about 60 years left based on the reserves and the consumption rate in 2010. Natural gas is generally considered as the interim energy solution to alleviate the more frequently occurring oil crisis.
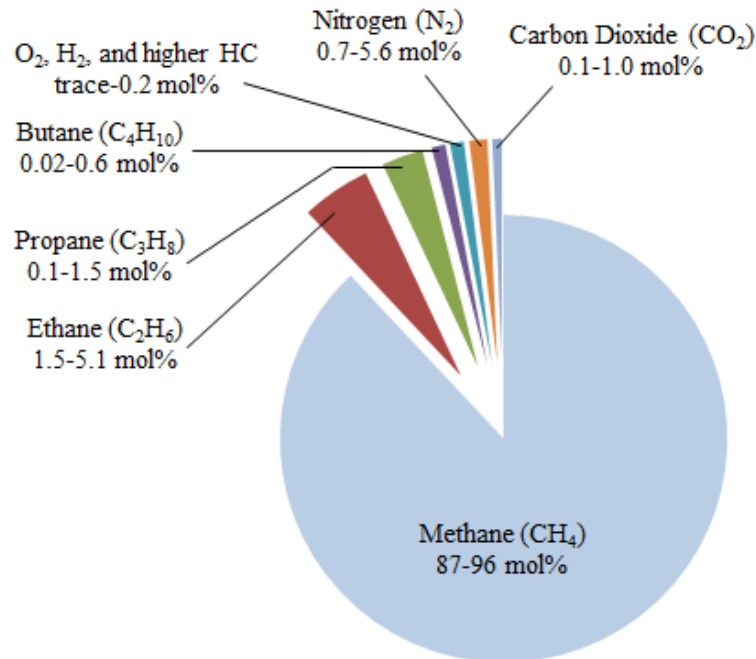
Fig.1   Typical composition of a commercial natural gas product [2]

Due to the cost and supply issues of petroleum based fuel, using natural gas as an alternative fuel has become an attractive option in implementing the HCCI concept for natural gas fueled engines. The advantages of using natural gas include easy mixture preparation, good chemical stability, high heating value, and less greenhouse emissions. However, natural gas also brings a few challenges for HCCI engine operations. Natural gas is known for its high octane number and therefore is hard to auto-ignite. To enable the use of natural gas in HCCI engines, higher compression ratios, significant amount of intake heating, and/or internal EGR (or residual gas trapping) is required to ensure the auto-ignition.

1.3 Use of the engine cycle simulation to study HCCI engines

In modern engine research and study, using hardware experiments alone could be very expensive and time-consuming, and many cause and effect relationships implicit in the test results are often hard to interpret. On the other hand, modeling and simulation approaches, although less precise in predicting the outcome of a specific test, could effectively isolate one variable at a time and conduct parametric studies on it. Therefore a simulation could point out cause-effect relationships more clearly, and a validated model could be a very useful tool to study novel engine concept or engines running with alternative fuels which are still not well known. The idea of using natural gas in HCCI engines is still relatively new and modeling studies are shown to be important to understand many fundamental features of the HCCI engines and how different fuels will fit into this novel engine concept.

Based on how the in-cylinder inhomogeneities and the fluid motions are treated, there are three major types of the model: zero-dimensional (single-zone) models, multi-zone models, and multi-dimensional CFD models. As mentioned earlier, HCCI combustion is not only controlled by the thermodynamics and fluid dynamics in the cylinder, but also largely dictated by the chemical kinetics. So in terms of the complexity of the chemical kinetics employed, there are also three major categories: ignition correlation plus global reaction, reduced kinetics, and detailed kinetics associated with the fuel. A brief discussion is given here to note some of the advantages and shortcomings of these models coupled with different kinetics. More details of the models used in this study are given in

the "Description of Models and Chemical Kinetics" section.

Single-zone models are most computationally efficient and therefore able to employ of the most detailed kinetics which is crucial in modeling chemical kinetics controlled combustion such as HCCI. Single-zone models are particularly useful in parametric studies due to their computational efficiency. The assumption of the homogeneous mixture in single zone models, however, makes it not able to provide any spatial information which is considered important in predicting temperature and emissions formation. Another application of single-zone models is for control purpose where the simulation time becomes crucial especially in real time control situations.
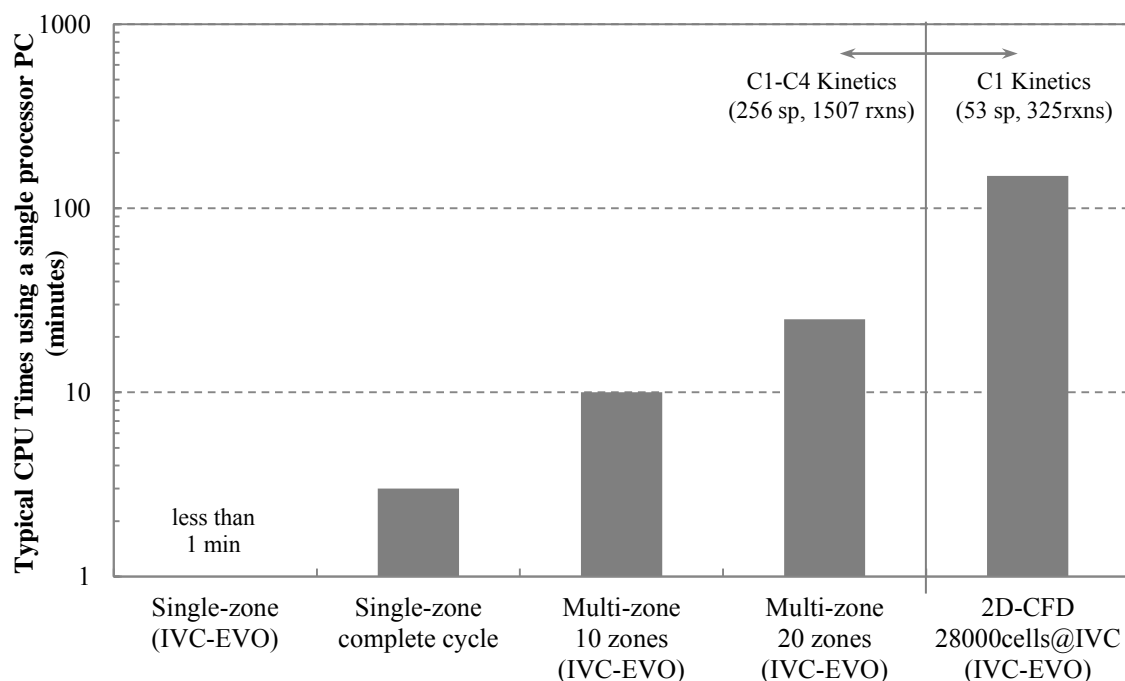
Fig.2   Estimated CPU times for different models with different kinetics

Multi-dimensional models are used to solve the fluid mechanics and chemical kinetics simultaneously and therefore provide the best accuracy in theory. Currently the major limitation of the CFD models is still the high computational intensity, which largely limits the coupling between detailed kinetics and fluid mechanics using fine meshes. A comparison of the computation times for different models has been shown in Fig.2. Even coupled with C1 kinetics, the two-dimensional CFD model still requires almost 100 times more CPU minutes than that of the single-zone model with detailed kinetics.

While computational fluid dynamics (CFD) have been applied to the study of HCCI combustion for simple fuels, it is often too computationally intensive for routine analyses involving practical fuels. Single-zone HCCI combustion models, on the other hand, permit detailed modeling of the chemical kinetics for practical fuel , but could not account for the low temperature region within boundary layers and crevices which are important for accurate unburned hydrocarbon (UHC) and carbon monoxide (CO) predictions. A multi-zone model serves as a compromise. Typically, multi-zone models apply detailed kinetics to multiple zones with different initial conditions which are extracted from the CFD simulations. It could provide better accuracy than a single-zone model and requires significantly less computing time than CFD simulations. The multi-zone model would be useful to study the effect of inhomogeneities on the ignition and combustion characteristics. However, multi-zone models usually require inputs from CFD simulations and therefore need more initialization and calibration effort.

2. BACKGROUND

The concept of HCCI engines has been studied for over a decade both experimentally and numerically. This section mainly notes a few previous studies which focused on the modeling of HCCI engines. For a complete picture of the HCCI engine studies, not only natural gas HCCI engines but also the HCCI engines with other fuels are also reviewed here. The following literature reviews are further divided into a couple of sub-sections: the effect of (1) intake air temperature, (2) equivalence ratio, (3) exhaust gas recirculation, (4) fuel composition, (5) intake air boosting, and (6) combustion chamber geometry.

Many literature studies, such as [3-9], have shown that the intake temperature or initial temperature at IVC has a significant effect on HCCI combustion phasing.

The simulation work by Noda and Foster [3] used a multi-zone model coupled with reduced chemical kinetics to study the H_2 fueled HCCI combustion in a four stroke engine. They've shown that the effect of gas temperature on ignition timing is more dominant than equivalence ratio, and introducing the temperature stratification is a better way to control combustion duration than the air and fuel inhomogeneity. The single zone model from Guo *et al.* [8] was coupled with detailed chemical kinetics. The simulation results have shown that increasing intake air temperature facilitates both the low- and high-temperature reactions, while it has less effect on the NTC delay period than engine speed and air fuel ratio. Both Jun *et al.* [5] and Ricklin *et al.*'s [6] modeling works have proved that the start

of combustion in HCCI engine is a strong function of the intake charge temperature.

In terms of emissions, single zone simulations by Ricklin *et al.* [6] have shown that CO would decrease with the increase of cyclic maximum temperature which is partly determined by intake temperature. On the other hand, from Dec *et al.* [4], the intake temperature, intake pressure, compression ratio, and engine speed are computationally and experimentally shown to have little effect on the UHC and CO emission at low load conditions. However, single zone models are not very accurate with UHC and CO emissions prediction due to the lack of crevice or boundary layer model. More multi-zone or multi-dimensional modeling is needed to study on this case.

The importance of equivalence ratio on HCCI combustion has been recognized by many researchers. Some of the major findings are summarized in the following paragraph.

The parametric studies on equivalence ratio by Jun *et al.* [5], both numerically and experimentally, have shown that lower equivalence ratio leads to retarded ignition timing and longer combustion duration. The multi-zone model coupled with detailed kinetics by Grenda [10] has confirmed that the increase of 0.2 in equivalence ratio advances about 10 crank angle degrees in the start of combustion. Machrafi *et al.* [11] performed single zone simulations and indicated that the equivalence ratio has a little greater influence on the low-temperature reactions than the main combustion. The CFD model coupled with reduced chemical mechanism by Neol *et al.* [12] compared in-cylinder pressure curves at different equivalence ratios. The results have shown the equivalence ratio's influence on combustion timing and indicated that the HCCI combustion process is not efficient for the

equivalence ratios lower than 0.3 at fixed intake temperature equal to 350K. The multi-zone simulation done by Amano *et al.* [13] has also indicated that the zone with the richest air/fuel mixture and the zone with highest temperature have the greatest impact on combustion phasing. In addition, the distribution of the equivalence ratio and temperature in the cylinder will affect the pressure rise rate.

Sequentially coupled multi-zone and CFD model with detailed kinetics of Curran was developed by Aceves *et al.* [14]. The model shows very good agreement with the experiments for a wide range of load from equivalence ratio ranging from 0.04 to 0.26. The CO emission increases as Φ decreases until $\Phi=0.1$, after which the CO decreases but the UHC emissions increase. At $\Phi=0.26$, lots of CO originates from crevices and boundary layers which are too cold for complete oxidation. As Φ reduces to 0.16, there exists a broad boundary layer with not hot enough temperature which leads to high concentration of CO. At $\Phi=0.10$, the combustion temperature continues to decrease so that even the center of the cylinder is not hot enough to oxidize CO to CO_2. Highest CO concentration is observed. Finally at $\Phi=0.04$, the temperature is so low that only the core region could react to CO. In the meantime, the broad boundary layer burns partially into intermediate hydrocarbons which results in the increase of HC.

Many researchers have reported the great influence of EGR on HCCI engines.

Using a 0.6 liter engine in the experiments and a corresponding single zone model, Machrafi *et al.* [11] studied the effect of EGR on the HCCI auto-ignition in terms of the thermal, diluting, and chemical effects. The diluting effect was studied by adding N_2 or

CO_2 into the intake mixture. The thermal effect was represented by the difference of heat capacity of these two diluents. The chemistry effect was studied by the NO, CO, and CH_2O addition. Both the diluting and thermal effect has been shown to delay both the cool flame and main ignition. The chemistry effect has been considered to be the dominant factor determining whether the auto-ignition was delayed or advanced, since the chemistry effects influence the amount of OH radicals present in the system. Neol *et al.* [12] has applied a CFD code coupled with reduced kinetics of n-heptane to study the HCCI combustion in a diesel engine. The authors have pointed out that cases with EGR have steep rate of heat release and higher EGR level extends the combustion duration and enables slow oxidation process. Multi-zone simulation results from Grenda [10] have shown that 20% change in EGR percentage leads to about a 10 crank angle degree change in the start of ignition.

Tominaga *et al.* [15] applied a sequentially coupled, non-reacting CFD and multi-zone model to study three different EGR setups: premix, port 1 (densely near the wall), and port 2 (densely nearly the center of cylinder). For the port 1 case, more exhaust gas is distributed in the high temperature zones (center) and the EGR effect is exaggerated. For the port 2 case, more exhaust gas is distributed near wall and low temperature zones and thus the EGR effect becomes less significant.

Another sequentially coupled multi-zone and CFD model was applied by Babajimopoulos *et al.* [16] to compare two method of introducing internal EGR: negative valve overlap (NVO) and rebreathing. The results have shown that the NVO method yields

less homogeneous mixture than the rebreathing method as the internal EGR percentage increases. The temperature is obviously stratified in all cases while the concentration distribution becomes noticeable in high internal EGR cases.

Different fuels show very different characteristics under HCCI conditions. For example, some types of fuels, such as natural gas, have only one stage of heat release in the HCCI combustion, while other types of fuels, such as gasoline and diesel fuel have a low temperature reaction stage and a high temperature reaction stage during HCCI-like heat release. Similar results have been discussed previously.

Fiveland *et al.* [17] studied the sensitivity of natural gas composition on the HCCI combustion using a single zone thermo-chemical model. 10% - 50% burned duration were well predicted while 50%-100% burned duration were significantly under-predicted by the single-zone model comparing to the experiment data. The results have shown that the addition of ethane, propane, and butane lower the auto-ignition threshold, and the increase of ethane, propane, or butane percentage in the mixture advances the ignition timings while maintaining other parameters unchanged. The possible uncertainties for both the experiment and the simulation were analyzed, and the authors state that 1-3 CA discrepancies between measurement and prediction is very acceptable due to those uncertainties.

From a series of multi-zone simulations, Kongsereeparp and Checkel [18] have pointed out that the addition of reforming gases (i.e., CO and H_2) advances SOC for the high-octane fuel (CNG) and retards SOC for the low-octane fuel (n-heptane). The SOC

change in the high-octane fuels mainly results from the altered mixture thermal properties by the addition of the reforming gases (RG). On the other hand, the RG addition strongly interferes with the cool flame chemistry of the low-octane fuels and thus affects the ignition timings of the main combustion. Using a single-zone model coupled with detailed chemical kinetics, Elkelawy *et al.* [19] have found that in the natural gas fueled HCCI combustion, the H_2 addition helps decreasing the ignition temperature needed and extending the limit of equivalence ratio to below 0.2. In addition, the ignition timing for the natural gas HCCI combustion is proportionally advanced with the increase of the hydrogen fraction in the fuel mixture. They attributed the effect of H_2 addition to the increased OH radicals during H_2 combustion.

The study of Ng and Thomson [20] applied a single zone model with detailed chemical kinetics to predict the effect of ethanol reforming (reform C_2H_5OH to CO and H_2) and hot EGR on lean ethanol HCCI combustion. The results have shown that ethanol reforming expands the lower limit of the initial temperature (at IVC), required to achieve HCCI combustion. Also, the fuel reforming increases the combustion temperature and NO_x emission as well, while increasing the portion of exhaust gas recirculation and reducing equivalence ratio have the opposite effect.

Since the limited operating range is one of the biggest challenges for an HCCI engines to be widely used in automotive industry, intake air boosting, including turbocharging and supercharging, becomes an important method to extend the operating range of HCCI engine.

By coupling a one-dimensional cycle simulation in GT-Power with a single-zone correlation-based combustion model, Mamlis *et al.* [21] compared four different boost strategies for homogeneous charge compression ignition engines. Single turbocharger, supercharger, small-small series turbochargers, and small-medium series turbochargers have been compared. Among the four strategies, the single turbocharger setup had the highest efficiency while the supercharger setup was the most robust to control intake conditions. The twin-turbo setups don't improve efficiencies due to the increased pumping, but do increase the highest attainable load.

Kulzer *et al.* [22] conducted drive cycle (NEDC and FTP 75) simulations of boosted HCCI engine. The fuel efficiency was estimated to be up to 17% in NEDC and FTP 75 could be reached. Simulations by Guo *et al.* [8] have shown that the effect of turbocharging on the low temperature reactions is relatively weak, but it greatly affects the main heat release phase.

Employing CFD simulations, effect of engine combustion chamber geometry on HCCI combustion has been studied by some researchers.

Using a coupled multi-zone and KIVA model, Lee *et al.* [23] have found that the overall heat transfer greatly depends on the stroke/bore (S/B) ratio, and higher S/B ratios have higher overall thermal efficiency, especially at low loads. A higher S/B ratio decreases the ringing intensity due to the enhanced thermal stratification, longer burn duration, smoother heat release, and lower pressure rise rate. The lowest S/B ratio has the highest combustion efficiency as a result of reduced thermal stratification and faster

combustion. Kong *et al.* [24] studied the effect of geometry generated turbulence by a coupled CFD and multi-zone model. They found that square-bowl piston case generates higher turbulence levels and results in higher heat transfer compared to the disc shaped piston. Therefore longer combustion duration has been observed for the case with square shaped piston due to higher heat loss.

Using experiments and a single zone model with detailed kinetics, Machrafi *et al.* [11] studied the influence of inlet temperature, equivalence ratio, and the compression ratio on combustion phasing, including the cool flame and main combustion, in a PRF fueled HCCI engine. The increase of compression ratio has the same effect on both the cool flame and main combustion in terms of advancing the phasing. Guo *et al.* [8] also indicated that increasing the compression ratio advances the phasing of both the low-temperature reaction and main combustion stage.

Kerschgens *et al.* [25] applied an interactively coupled CFD and multi-zone method to study three different piston bowl geometry: reduced diameter bowl, original bowl, and stretched diameter bowl. The results show at the most advanced injection timing, the narrow bowl leads to incomplete combustion because some of the fuel is trapped in the deep bowl and not burned thoroughly. The stretched diameter bowl reduces the cylinder tumbling and thus leads to more stratified fuel concentration, and finally causes the increase of the CO emissions. The original bowl is considered the best in this specific study.

3. OBJECTIVES

As summarized in the previous section, many studies have been completed on the use of natural gas in HCCI engines. Few of them, however, have systematically compared natural gas with other fuels such as gasoline in terms of the HCCI operations. The current work is aimed at comparing the use of natural gas, gasoline, and dimethyl ether (DME) in HCCI combustion, and providing better understandings of the auto-ignition, engine performance, and emissions characteristics for natural gas fueled HCCI engines. This objective is going to be accomplished by applying both zero- and multi-dimensional simulations coupled with chemical kinetics. A zero-dimensional (single-zone) model employing detailed chemical kinetics is used to determine the general trends of auto-ignition characteristic, engine performance, and nitric oxides emissions as functions of major operating parameters for a specific HCCI engine. Results for natural gas, gasoline, and DME surrogate are obtained, compared and analyzed.

In addition to the single-zone simulation, a multi-zone model coupled with non-reacting (cold flow) CFD simulation is employed to be able to account for the effect of in-cylinder inhomogeneities on the HCCI combustion. By the cold flow engine CFD simulations, the temperature and equivalence ratio distributions will be obtained and then used to initialize the multi-zone model. From the multi-zone simulations, the effects of inhomogeneous temperature and equivalence ratio field on ignition timing, combustion phasing, and emissions formation are going to be studied and discussed.

Finally, a two-dimensional computational fluid dynamics (CFD) model is employed to study the in-cylinder temperature and species distribution. The temperature and equivalence ratio stratification play a very important role during the ignition and combustion process. So the prediction of the in-cylinder spatial distribution prediction could provide better understanding of the auto-ignition and combustion process.

4. DESCRIPTION OF MODELS AND CHEMICAL KINETICS

In this section, detailed descriptions are first provided for the single-zone, multi-zone, and two-dimensional CFD model. The specifications of the engine being studied are then given, followed by a brief summary of the fuel surrogates and chemical mechanisms employed in this study.

4.1 Single-zone (zero-dimensional) model

Natural gas HCCI combustion in IC engines is simulated using a single zone model with detailed chemical kinetics in CHEMKIN PRO [26]. The basic assumption of the model is homogeneous temperature and species composition distribution throughout the cylinder. Only the closed portion of the cycle (from IVC to EVO) is simulated and no valve event or gas exchange process is considered in this model. The thermodynamic system described by the model is shown in figure 3. In the cylinder, there are four independent properties including volume (V), pressure (P), temperature (T), and species concentration (Y_k). Also there is heat transfer to the cylinder wall and work transfer by the piston. Formulations for solving the thermodynamic system are briefly described below.
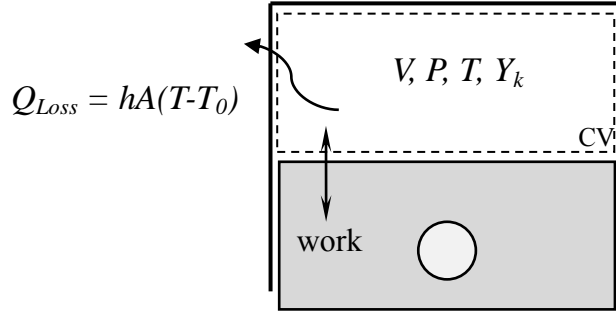
Fig.3   Schematic diagram of the single-zone thermodynamic model

The species conservation for the systems is [26],

$$\left(\rho V\right)\frac{dY_k}{dt} = \left(\dot{\omega}_k V\right)W_k \tag{1}$$

where ρ is the mass averaged density, Y_k and W_k are the mass fraction and molecular weight

of the kth species in the system, and $\dot{\omega}_k$ is the molar rate of production of the kth species

by gas-phase chemical reaction per unit volume. The energy equation for the system is

[26],

$$\frac{dU}{dt} = -\dot{Q}_{loss} - P\frac{dV}{dt} \tag{2}$$

After a few rearrangements using mass balance and the relation between internal

energy and enthalpy, the transient energy equation for the gas temperature is obtained [26],

$$\frac{dU}{dt} = \frac{d\left(H - PV\right)}{dt} = \frac{dH}{dt} - P\frac{dV}{dt} - V\frac{dP}{dt} \tag{3}$$

$$\frac{dH}{dt} = \frac{d\left(\rho V \bar{h}\right)}{dt} = \rho V\left(\sum_{k=1}^{K_g} Y_k c_{pk}\frac{dT}{dt}\right) + \rho V\left(\sum_{k=1}^{K_g} h_k \frac{dY_k}{dt}\right) + \sum_{k=1}^{K_g} Y_k h_k \frac{d\left(\rho V\right)}{dt} \tag{4}$$

$$\left(\rho V\right)\bar{c}_p\frac{dT}{dt} = -V\sum_{k=1}^{K_g}\left(h_k \dot{\omega}_k\right)W_k + V\frac{dP}{dt} - \dot{Q}_{loss} \tag{5}$$

where $\bar{h}$ and $\bar{c}_p$ are the mass averaged enthalpy and specific heat at constant

pressure of the gas mixture, h_k and c_{pk} represent the enthalpy and specific heat at constant

pressure for kth species, and K_g is the total number of species in the system. Note that in equations (3) and (4), the enthalpy H includes the enthalpy of formation (H_f°) and the sensible enthalpy (H_t). The last term in equation (4) is eliminated because that the total mass of the system doesn't change.

The production rate of each species, $\dot{\omega}_k$, appears in the energy equation and is directly solved from the preselected kinetics. In Chemkin, each species is associated with thermodynamic data that are used to determine equilibrium constants and the reverse-rate for the corresponding reactions. Elementary reactions involving K_g species can be represented in the general form,

$$\sum_{k=1}^{K_g} v'_{ki}\, x_k \Leftrightarrow \sum_{k=1}^{K_g} v''_{ki}\, x_k \qquad (i=1,\dots,I) \qquad (6)$$
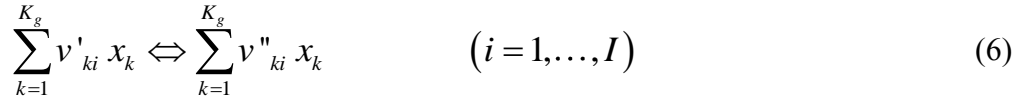
where v'_{ki} and v''_{ki} indicates forward and reverse stoichiometric coefficients for the ith reaction, and x_k is the chemical symbol of the kth species. Then the expression for the production rate $\dot{\omega}_k$ can be obtained,

$$\dot{\omega}_k = \sum_{i=1}^{I}\left[\left(v''_{ki}-v'_{ki}\right)\left(k_{fi}\prod_{k=1}^{K_g}[X_k]^{v'_{ki}} - k_{ri}\prod_{k=1}^{K_g}[X_k]^{v''_{ki}}\right)\right] \qquad (k=1,\dots,K) \quad (7)$$

where k_{fi} and k_{ri} are the forward and reverse rate constants of the ith reactions, and $[X_k]$ is the molar concentration of the kth species. The forward rate constants for the reactions are generally the inputs of the model, and are assumed to have the following Arrhenius temperature dependence:

$$k_{fi} = A_i T^{\beta i}\exp\left(-\frac{E_i}{R_c T}\right) \qquad (8)$$

Instantaneous spatially-averaged heat transfer to the cylinder wall is calculated

using a version of the Woschni correlation [27]. This version has been adjusted for HCCI

combustion [26], as shown below,

$$Nu_h = a \cdot \mathrm{Re}^b \cdot \mathrm{Pr}^c = 0.035 \mathrm{Re}^{0.8} \tag{9}$$

where $a = 0.035$, $b = 0.8$, $c = 0$ is chosen for this study.

$$\mathrm{Re} = \frac{\rho w B}{\mu} \tag{10}$$

where the local average gas velocity w is correlated as follows,

$$w = \left[\left(C_{11} + C_{12} \frac{v_{swirl}}{\bar{v}_p} \right) \bar{v}_p + C_2 \frac{V_d T_r}{p_r V_r} (p - p_m) \right] \tag{11}$$

where V_d is the displaced volume; p is the instantaneous cylinder pressure; p_r, V_r, T_r are the

pressure, volume and temperature at the reference state; p_m is the motored cylinder pressure

at the same crank angle as p. In this study, C_{11}=2.28, C_{12}=0.308, C_2=0.54, and v_{swirl}=0 is

used. More detailed description of this heat transfer correlation can be found in [27].

This model does not include the gas exchange process or friction. Since gas

exchange and friction do not have a direct effect on the in-cylinder thermodynamics or

chemical kinetics, these two limitations are not significant for the purposes of the

single-zone simulation.

4.2 Multi-zone model

As mentioned in the introduction section, multi-zone models typically require

non-reacting (cold flow) fluid mechanics simulation to provide the initial temperature and

concentration distributions in the cylinder. With these initial distributions, appropriate

number of zones can be determined and those zones can be established and initialized with

different temperatures and concentrations, as shown in figure 4. Figure 4 shows an

example of the setup procedure where the continuous temperature distribution from the

CFD simulation is converted to the zonal conditions in the multi-zone model. After the

zonal initial conditions are set up, the detailed chemical kinetics can be applied and solved

in all zones fully coupled.
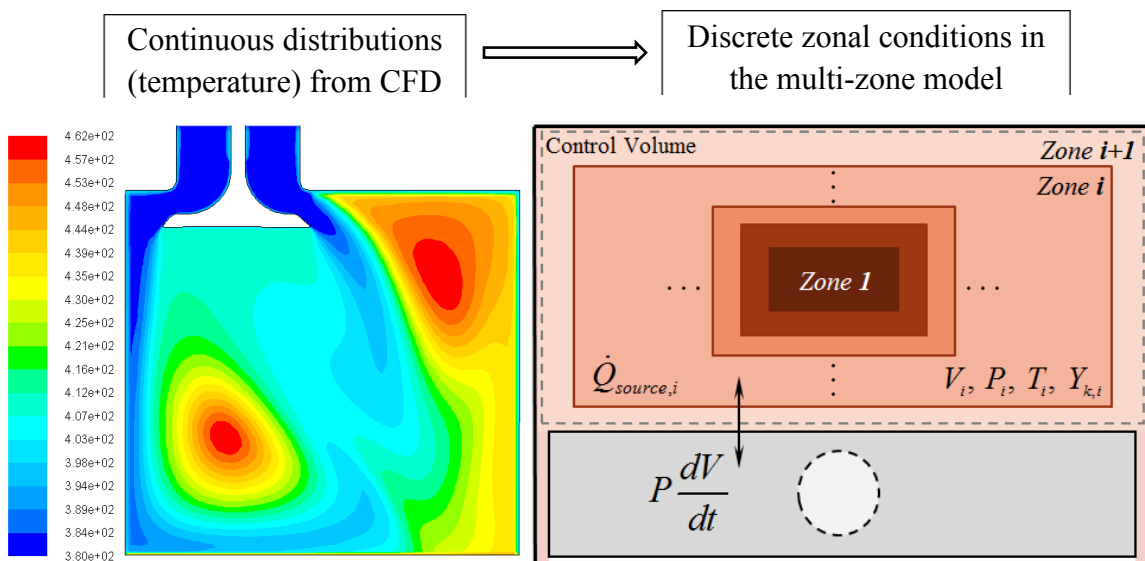
Fig.4   Illustration of the multi-zone model setup procedure, temperature distribution from CFD (left) and zonal conditions in multi-zone model (right)

The assumptions [26] pertaining to this model formulation are as follows. First of

all, all zones are assumed to have the same, uniform pressure. Second, the mass or heat

transfer between zones is assumed to be negligible and the only interaction between the

zones is the compression work. Third, the total volume of the zones must equal the cylinder

volume computed by the slider-crank relationship used in the single-zone internal-combustion engine model. This constraint is used to determine the zonal and cylinder pressure [26].

The governing equations for the multi-zone model are similar to those for the single-zone model, except for the additional superscript "i" which represent the zone number, as shown in equation 12 (conservation of species) and equation 13 (energy equation) [26].

$$\left(\rho^i V^i\right)\frac{dY_k^i}{dt} = \left(\dot{\omega}_k^i V^i\right)W_k^i \qquad for\ i = 1, 2, .., N\ zones \tag{12}$$

$$\left(\rho^i V^i\right)\bar{c}_p^i\frac{dT^i}{dt} = -V^i\sum_{k=1}^{K_g}\left(h_k^i\dot{\omega}_k^i\right)W_k^i + V^i\frac{dP}{dt} - \dot{Q}_{loss}^i \qquad for\ i = 1, 2, .., N\ zones \tag{13}$$

The details of solving these equations for all zones fully coupled are given in Appendix I and the Chemkin user manual [26].

4.3 Two-dimensional non-reacting CFD simulation

The computational fluid dynamics simulations of non-reacting (cold flow) intake flow are performed in FLUENT. In figure 5, a two-dimensional mesh has been generated to include the intake valve. The calculations are carried out from the intake valve opening (IVO) to the intake valve closing (IVC), which is about 230 degree crank angles for the specific engine used in the current study. This is a moving mesh problem and there are ~3000 cells at IVO and ~10000 cells at IVC. The assumptions of this cold flow simulation are summarized as follows.

1. The computational domain is two-dimensional (planar 2D) in order to reduce the CPU time and enable a certain amount of parametric studies.

2. Heat transfer occurs between the gas and the boundaries, including the cylinder liner, piston, cylinder head, and intake valve. The boundary temperatures are assumed to be at some constant values.

3. The turbulence considered in the simulation employs the k-ε model based on RANS (Reynolds averaged Navier-Stokes equation).

4. Initially the temperature and concentration are assumed to be homogeneous in the computational domain. The inlet flow is also assumed to have constant temperature and species concentration over time.

The detailed governing equations in the computational fluid dynamics are shown in Appendix II.
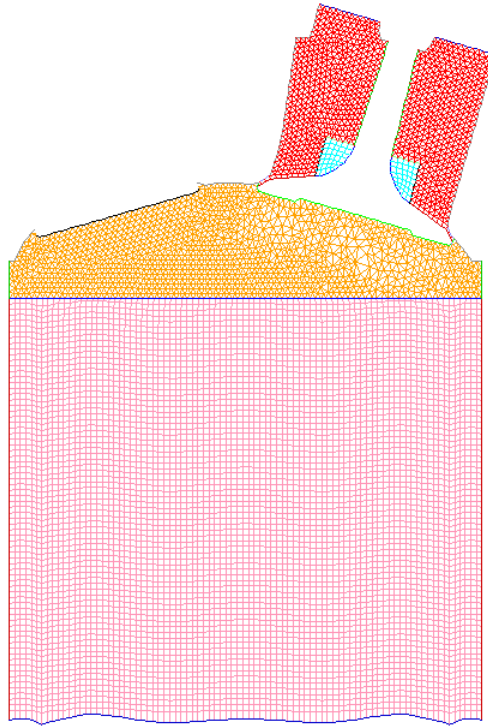
Fig.5   Two-dimensional mesh for the non-reacting intake flow simulation

4.4 Two-dimensional combustion CFD simulation

Similar to the non-reacting case, the CFD simulations of the HCCI combustion are carried out in FLUENT. Again, in order to reduce the computational intensity, the flow field in the cylinder is assumed to be axial-symmetric, and only a 2-D flow field is solved as shown in figure 6. Uniform quadratic mesh is generated throughout the 2-D flow field, and includes ~28000 cells at IVC.

Calculations were carried out from intake valve closure (IVC) to exhaust valve opening (EVO). The k-ε model based on RANS (Reynolds averaged Navier-Stokes equation) is employed for turbulence computation. Due to the limitation of computer resource, a few assumptions, which simplify the model, were necessary. These

assumptions are summarized and discussed below.

All the species are assumed to be homogeneously mixed at the molecular level at the start of the calculation, which is IVC in the present study. This is a reasonable approximation considering the use of an intake mixer, early port injection, and zero external EGR in the experiments. For conditions with a large amount of residual gases, this assumption could be problematic and need to be eliminated by modeling the valve events and the flow through valves.

(a)   (b)
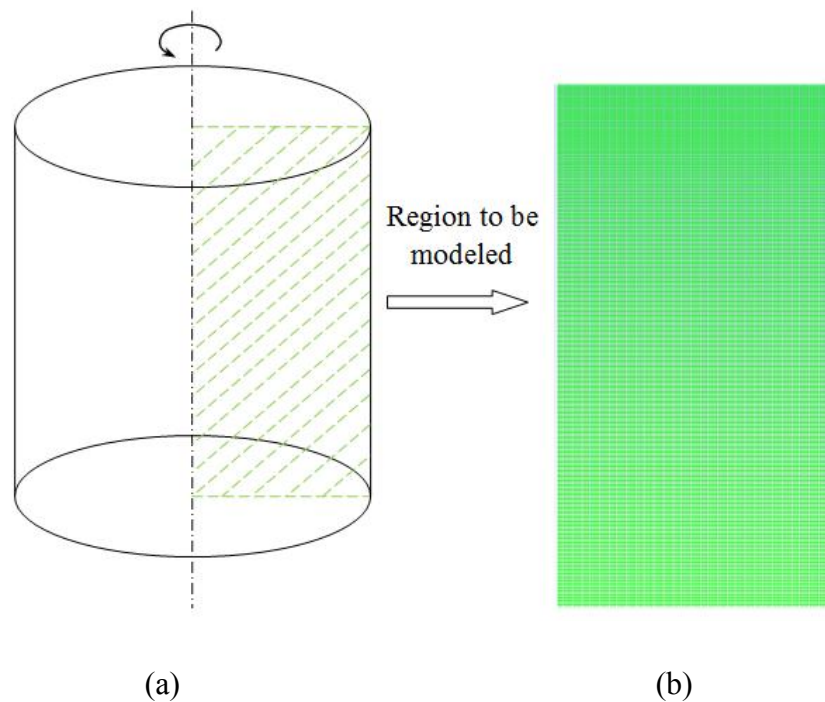
Fig.6   (a) 2-D Axial-symmetric modeling of the engine cylinder, and (b) the actual mesh in Fluent (~28000 cells at IVC)

The sub-grid scale turbulence-chemistry interaction is not modeled in the current study. The mean values of temperature and concentrations in each cell are used in the chemical kinetics calculation. For the HCCI case resolved with fine grid, the sub-grid fluctuation is not expected to be significant. In addition, in HCCI combustion the timescale for chemical kinetics is usually much larger than the timescale for sub-grid turbulent mixing (dissipation of the small turbulence eddies), reaction rate could be well predicted by chemical kinetics only.

The temperature at the start of the simulation (IVC) is assumed to be 20-40K higher than the reported intake manifold temperature [27]. This increment is due to the heating effects of the residual gases and compression from BDC to IVC. To match the calculations to the experimental data (which will be shown in the model validation section), the temperature at IVC was adjusted. The same increment was used for all cases.

4.5 Engine specifications

The engine being modeled is a 1.1 liter single-cylinder four-stroke engine and the specifications are summarized in Table 1.

Table 1 Engine parameters used in the model [28]

Engine	Yanmar TS230R single cylinder
Bore	112 mm
Stroke	115 mm
Displacement volume	1.132 Liter
Compression ratio	18.8
Connecting rod to Crank radius ratio	3.43
Intake valve opening (IVO)	355° CA
Intake valve closing (IVC)	588° CA
Exhaust valve opening (EVO)	125° CA

4.6 Fuel surrogates and chemical mechanisms

The compositions of surrogates for natural gas, gasoline, and dimethyl ether are listed in Table 2. Although the actual fuels have many compositions, the surrogate compositions are representative. The chemical mechanisms used in the single-zone, multi-zone, and CFD model are also summarized in Table 2.

Table 2 Fuel surrogates and their chemical mechanisms used in this study

Fuel	Surrogate (mole fraction)	Mechanism used in the single- and multi-zone model	Mechanism used in the CFD model
Natural Gas	88% CH_4, 6% C_2H_6, 4% C_3H_8, 2% C_4H_{10} [28]	C^3 natural gas [29] 256 species, 1507 reactions	Gri-mech 3.0 [30] 53 species, 325 reactions
Gasoline	20% $C_6H_5CH_3$ 17% C_7H_{16} 63% C_8H_{18} [31]	Gasoline [31] 891 species, 3902 reactions	N/A
Dimethyl Ether	100% CH_3OCH_3	Zhao *et al.* DME [32] 55 Species, 315 reactions	N/A

Since the NO_x emission characteristics for HCCI combustion are going to be discussed in this study, a brief description of the NO_x sub-mechanism is necessary. The NO_x kinetics contained in GRI-mech 3.0 includes 17 species and 71 reactions, and the one in C^3 natural gas mechanisms is from Sivaramakrishnan *et al.* [33] which includes 29 species and 218 reactions. These two mechanisms share some of the core reactions which are described next.

The reactions included in the extended Zeldovich mechanism (also known as the thermal mechanism) are shown in Table 3. Due to the strong triple bond of the N_2 molecule, these reactions are significant only when there is a high enough temperature and sufficient time. The extended Zeldovich mechanism has been successfully applied to predict the nitrogen oxides emissions for engine conditions [27]. Table 4 shows the main reaction responsible for the prompt mechanism. The prompt mechanism is important when there is fuel-bound nitrogen or when the combustion temperature is too low to activate the thermal mechanism [34]. The prompt mechanism might be significant for the nitrogen oxides emissions in HCCI engines, since the HCCI combustion usually features low temperature combustion. Table 5 lists the reactions related to the so called nitrous oxide mechanism. This mechanism depends on a few termolecular reactions involving N_2O and the subsequent decomposition to nitric oxide. The nitrous oxide mechanism is significant at low temperatures and for lean premixed mixtures [34, 35], and therefore is also important to be included for the HCCI combustion.

Some other NO_x formation mechanisms such as the NNH route are also included in

the detailed kinetics. The details of these routes are not shown for they have little contribution to the NO_x formation at the conditions examined in the current work. For the NNH route, studies by [36-38] indicated that the NNH route was found important for rich hydrogen flames, relative short residence times (<1ms), and relative low temperatures (<2100 K). At the conditions examined in the current study, the residence time typically ranges from 2 ms to 10 ms and peak temperatures are over 2200K. Results illustrating the contributions of the different mechanisms are shown in the Results and Discussion section.

Table 3 The extended Zeldovich mechanism (thermal mechanism, rates from [33])

Reactions	A_i	β_i	E_i/R_c
$N + NO \longleftrightarrow N_2 + O$	2.70×10^{13}	.00	355.00
$N + O_2 \longleftrightarrow NO + O$	9.00×10^{9}	1.00	6500.00
$N + OH \longleftrightarrow NO + H$	3.36×10^{13}	.00	385.00

Table 4 The prompt mechanism (rates obtained from [33])

$CH + N_2 \longleftrightarrow HCN + N$	3.12×10^{9}	.88	20130.00
$HCN + O \longleftrightarrow NCO + H$	1.38×10^{4}	2.64	4980.00
$NCO + H \longleftrightarrow NH + CO$	5.40×10^{13}	.00	.00
$NH + H \longleftrightarrow N + H_2$	3.20×10^{13}	.00	330.00
$NH + OH \longleftrightarrow N + H_2O$	2.00×10^{9}	1.20	.00
$N + OH \longleftrightarrow NO + H$	3.36×10^{13}	.00	385.00

Table 5 The nitrous oxide (N_2O) intermediate mechanism (rates obtained from [33])

$N_2O + M \longleftrightarrow N_2 + O + M$	7.91×10^{10}	0.00	56020.00
$N_2O + O \longleftrightarrow N_2 + O_2$	1.40×10^{12}	0.00	10810.00
$N_2O + O \longleftrightarrow 2NO$	2.90×10^{13}	0.00	23150.00
$NO + NH \longleftrightarrow N_2O + H$	3.65×10^{14}	-0.45	0.00
$NO + NCO \longleftrightarrow N_2O + CO$	1.90×10^{17}	-1.52	740.00

5. MODEL CALIBRATION AND VALIDATION

In this section, predicted pressure curves from simulations are compared to the experimental data and followed by a brief discussion on the model calibration and validation for different models.

5.1 Validation of the single-zone and multi-zone model

The single-zone and multi-zone models have been validated by the experimental work done by Jun et al. [28]. The operating conditions at which the prediction and measurements are compared are summarized in Table 6. The temperatures at IVC are used to calibrate the start of combustion for both the single-zone and multi-zone simulations. Figures 7-9 show the measured and predicted pressure traces as a function of crank angle at different equivalence ratios.

The single-zone simulation (figure 8) predicts the start of combustion reasonably well using detailed chemical kinetics. The peak pressures, however, are obviously over-predicted and the combustion durations are under-predicted. This is mainly due to the assumption of a homogeneous mixture throughout the cylinder. Because of that, all of the air/fuel would be ignited at the same time and the combustion rate is significantly elevated. In general, for the higher equivalence ratio cases, the single-zone simulation captures the main feature of the HCCI combustion. As the mixture become very lean, the single-zone model starts to fail to predict the slower and weaker combustion associated with lean

mixtures. The multi-zone results (figure 9) have generally better agreement with the measurement than single-zone simulations. The longer combustion durations and lower peak pressures in the experimental data are better captured in the multi-zone simulations.

Table 6 Initial conditions for the 0D simulation and the experiments from [28]

Parameters	Single- and multi-zone Model	Experiment by Jun et al. [28]
Engine speed (RPM)	800	800
IVC timing	-132 aTDC	-132 aTDC
Intake manifold temperature (K)	N/A	380
Intake manifold pressure (bar)	N/A	1.6
Temperature at IVC (K)	417	N/A
Pressure at IVC (bar)	1.6	N/A
Wall Temperature (K)	450	N/A
Equivalence Ratio	0.2 - 0.45	0.2 - 0.45
Natural gas composition (mole fraction)	88%CH_4 6%C_2H_6 4%C_3H_8 2%C_4H_{10}	88%CH_4 6%C_2H_6 4%C_3H_8 2%C_4H_{10}
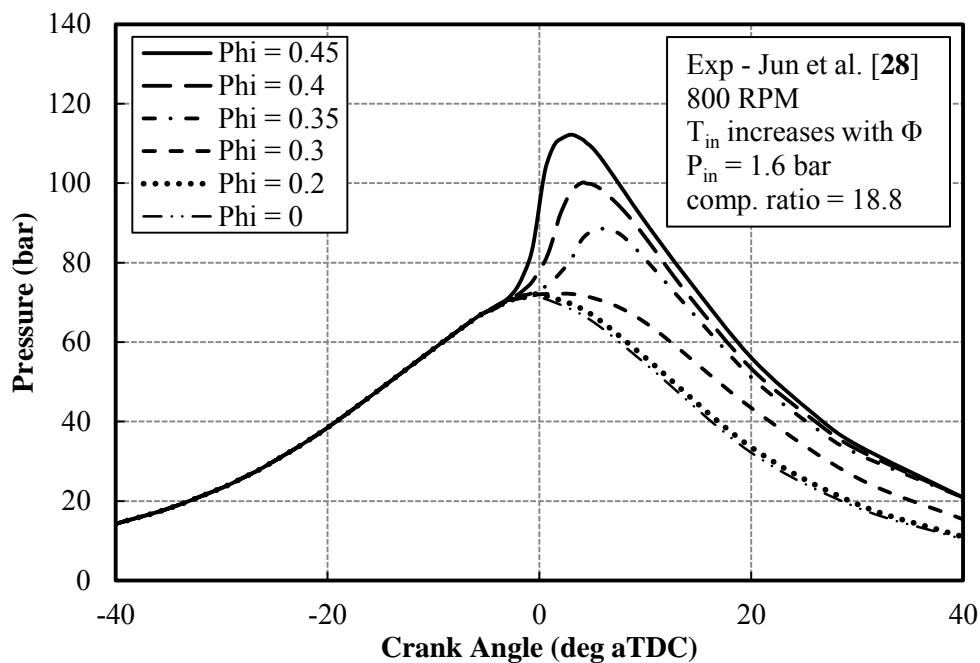
Fig.7   Measured pressure traces as a function of crank angle at different equivalence ratios. Experimental data from Jun et al. [24].
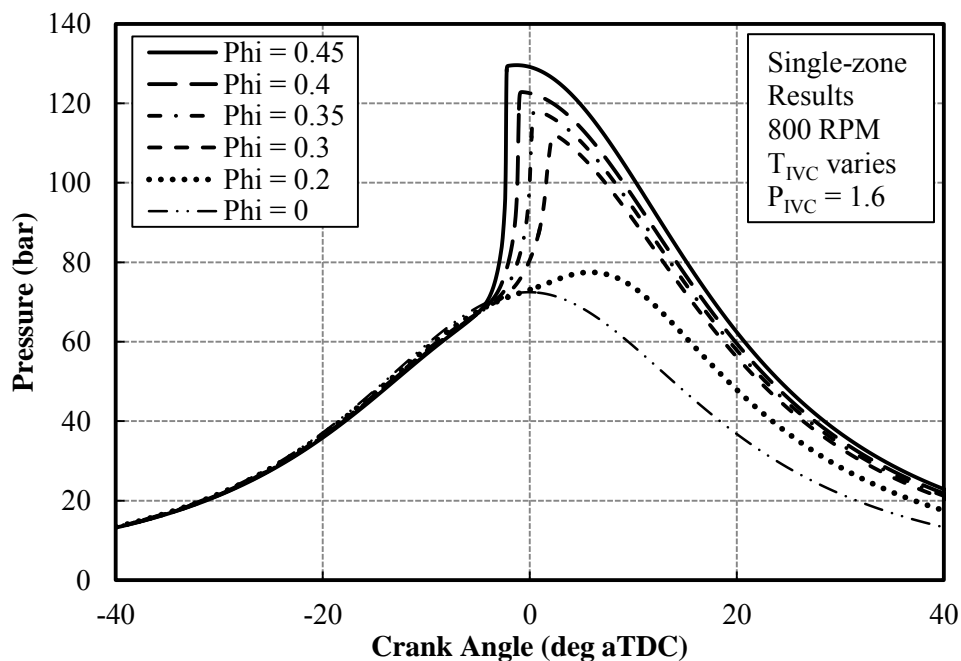
Fig.8   Predicted pressure as a function of crank angle at different equivalence ratios
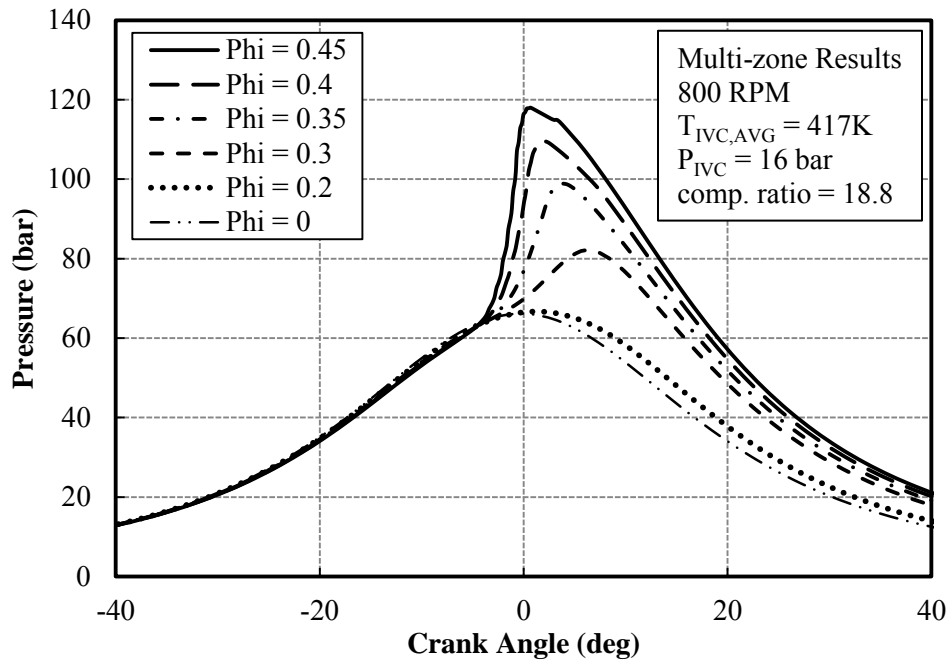
Fig.9 Predicted pressure as a function of crank angle at different equivalence ratios from the multi-zone simulations

5.2 Calibration and validation of the two-dimensional combustion CFD model

Table 7 summarizes the operating conditions of the 2-D combustion CFD simulation and the experimental work done by Jun *et al.* [28], which is used to validate the model. Since in the experiments only intake manifold temperature is measured, temperature at IVC is estimated to be 30K higher based on the heating effect of hot residual gases and hot cylinder wall. Pressure at IVC is assumed to be the same as that in intake manifold. Since the chemical kinetics did not include C_4H_{10} kinetics, a slightly different natural gas surrogate is used.

Figure 10 shows the predicted pressure curves from two-dimensional CFD simulations for different equivalence ratios. Comparing figure 10 with the experimental

data (figure 8), there are still some discrepancies in the start of combustion, pressure rise rate, and peak pressure values. These differences might result from three aspects: (1) treating the combustion chamber as a two-dimensional field rather than three-dimension, (2) assuming homogeneous temperature and concentration at the start of simulation, and (3) using C1 kinetics rather than C4 kinetics. These drawbacks are the necessary compromises for an affordable CPU time. Since the main purpose of the 2D CFD study is to better visualize the HCCI combustion process, the agreement between the prediction and measurement is acceptable.

Table 7 Initial conditions for the 2-D CFD simulation and the experiments from [28]

Parameters	CFD Model	Experiment by Jun et al. [28]
Engine speed (RPM)	800	800
IVC timing	-132 aTDC	-132 aTDC
Intake manifold temperature (K)	N/A	380
Intake manifold pressure (bar)	N/A	1.6
Temperature at IVC (K)	410	N/A
Pressure at IVC (bar)	1.6	N/A
Wall Temperature (K)	400 for cylinder 550 for piston	N/A
Equivalence Ratio	0.2 - 0.45	0.2 - 0.45
Initial Turbulence Kinetic Energy (m^2/s^2)	0.01	N/A
Initial Turbulence Dissipation Rate (m^2/s^2)	0.01	N/A
Initial Swirl Velocity (m/s)	0.01	N/A
Natural gas composition (mole fraction)	90%CH_4 6%C_2H_6 4%C_3H_8	87.5%CH_4 6.5%C_2H_6 4%C_3H_8, 2%C_4H_{10}
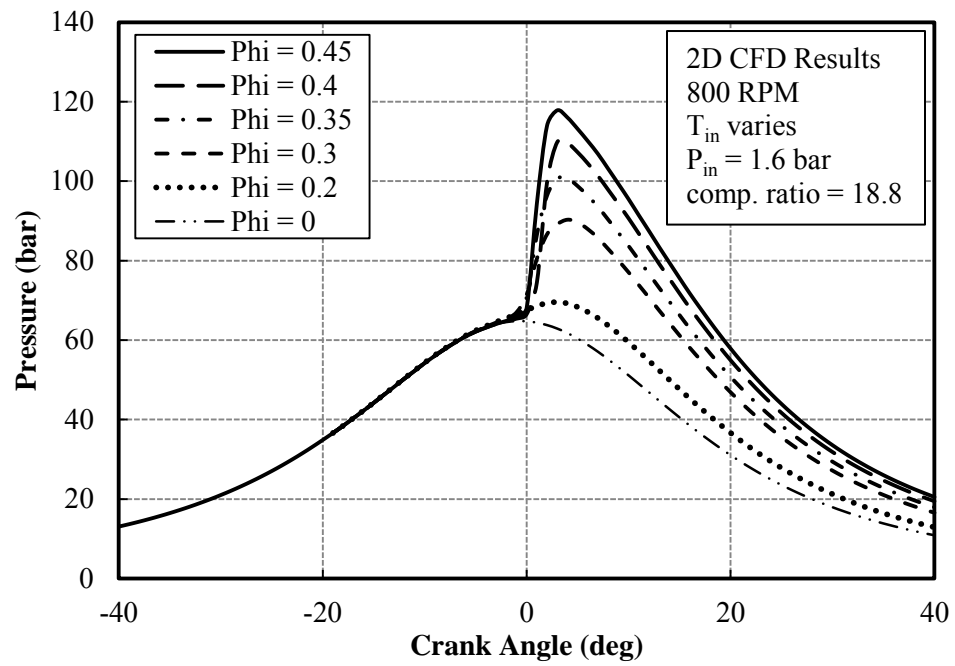
Fig.10 Predicted pressure as a function of crank angle at different equivalence
ratios from the 2D-CFD simulations

6. RESULTS AND DISCUSSION

The results from single-zone, multi-zone, two-dimensional non-reacting CFD, and combustion CFD simulations are presented and discussed in this section. In section 6.1, the single-zone simulation results including the effect of operating parameters on HCCI combustion and emission characteristics are provided and analyzed in two different settings. This part not only shows the results for natural gas but also compares them with the gasoline cases and the dual fuel cases with additional dimethyl ether (DME) addition. Next in section 6.2, the temperature and concentration distributions obtained from the cold-flow CFD simulations are shown and discussed, followed by the multi-zone simulation results illustrating the effect of these stratifications on the natural gas HCCI combustion. Finally in section 6.3, the results from the two-dimensional combustion CFD model are presented to better visualize the HCCI combustion process.

6.1 Results from single-zone simulations

In this sub-section, the single-zone results are presented and include the following: (1) the minimum initial temperature ($T_{IVC,min}$) approach, (2) the effect of operating conditions on $T_{IVC,min}$, (3) the best efficiency temperature ($T_{IVC,beff}$) approach, (4) the effect of operating conditions on $T_{IVC,beff}$, (5) the comparison of natural gas and gasoline at best efficiency conditions, and (6) the potential of NG/DME duel fuel operation

6.1.1   <u>Minimum initial temperature approach</u>

As described earlier in this paper, the characteristics of HCCI combustion, e.g. start of combustion (SOC), is largely dictated by the chemical kinetics. Chemical kinetics are greatly influenced by the thermodynamic conditions in the combustion chamber, and the temperature is the most influencing thermodynamic property. So at the start of the simulation (IVC), a range of initial temperatures are examined to find the minimum initial temperature, $T_{IVC,min}$, which is necessary for complete combustion. As an example, figure 11 shows the fraction of burned fuel at EVO as a function of initial temperature at IVC. Figure 12 shows the in-cylinder pressure curves as a function of crank angle for different initial temperatures at IVC. Figures 11 and 12 illustrate the process to determine $T_{IVC,min}$. In the present study, complete combustion is defined as 99% or more of the fuel is consumed. The resolution of this $T_{IVC,min}$ search process is set to 1 K. Theoretically, $T_{IVC,min}$ represents the lower limit of successful HCCI combustion. As shown, for initial temperatures below $T_{IVC,min}$, ignition is not successful and the result is essentially a "motoring" cycle.
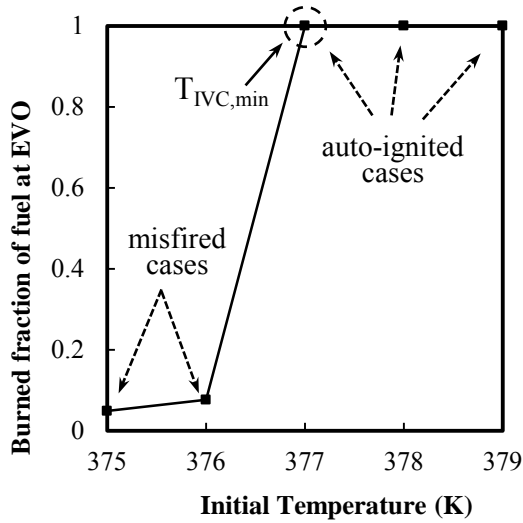
Fig.11 Determine $T_{IVC,min}$ by examining burned fraction at EVO
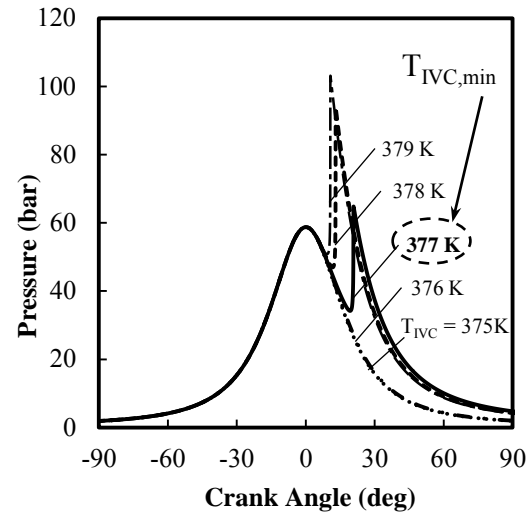
Fig.12 Confirm $T_{IVC,min}$ by comparing pressure curves

6.1.2   Effect of operating conditions on the minimum initial temperature

So, to study the effect of operating conditions on the $T_{IVC,min}$ and auto-ignition threshold, parametric studies were conducted (Table 8). For each case, $T_{IVC,min}$ is determined. The differences in $T_{IVC,min}$ by using different fuels are compared in figures 13-16. Figure 17 compares the temperatures and pressures at the start of combustion (1% heat release) for different fuels.

Table 8 Parametric studies for investigating $T_{IVC,min}$ in single-zone simulations

Cases	$T_{IVC,min}$ Varying (K)	P@IVC (bar)	Equivalence Ratio	Engine speed (RPM)	Compression Ratio
Base case	$T_{IVC,min}$	1.0	0.3	800	18.8
P_{IVC}	$T_{IVC,min}$	0.6 – 2.0	0.3	800	18.8
Φ	$T_{IVC,min}$	1.0	0.2 – 0.7	800	18.8
N	$T_{IVC,min}$	1.0	0.3	800 – 4000	18.8
CR	$T_{IVC,min}$	1.0	0.3	800	10 – 22

Figure 13 shows the minimum required temperature at IVC as a function of compression ratio for natural gas, gasoline, and DME. The area above each curve indicates the operating conditions at which the combustion efficiency predicted by the single-zone model is higher than 99%. On the other hand, the area below each curve implies the cases with low combustion efficiency or misfire cases. All three fuels need more and more help of intake heating for successful HCCI combustion as compression ratio decreases. This is because the compression work is reduced as compression ratio decreases and the auto-ignition threshold needs to be reached by a higher initial temperature. Apparently, n-heptane needs the least intake heating due to its high cetane number. Natural gas requires the highest initial temperatures among three fuels because of its high octane number (lower cetane number), and iso-octane is in between. Similar trends with respect to the fuel are also observed in the following figures (14-16).

Figure 14 shows the minimum required temperature at IVC ($T_{ivc,min}$) as a function of equivalence ratio for using natural gas, gasoline, and DME as fuels. With the increase of

equivalence ratio, a higher initial temperature is required for auto-ignition to occur. Two

factors are affecting the $T_{ivc,min}$ with equivalence ratio (Φ) variations: (1) the change in ratio

of specific heats (Υ), and (2) the change in the auto-ignition threshold (flammability). Fuel

species have lower specific heat ratios than air, so a higher Φ leads to a lower the overall

specific heat ratio. If assuming isentropic compression, a lower specific heat ratio results in

a lower temperature due to compression which requires a higher initial temperature to

reach the auto-ignition threshold. In addition, the change in equivalence ratio would also

affect the flammability of the fuel/air mixture. As equivalence ratio reduces, the threshold

of the HCCI combustion of the fuel/air mixture increases and therefore a higher initial

temperature is required for successful auto-ignition, as seen in figure 14. Also in figure 14,

natural gas requires the highest initial temperature among the three fuels.
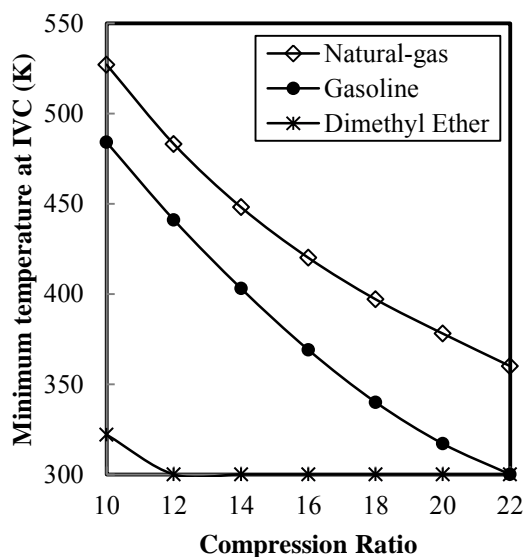
Fig.13 $T_{IVC,min}$ as a function of compression ratio for natural gas, gasoline and dimethyl ether
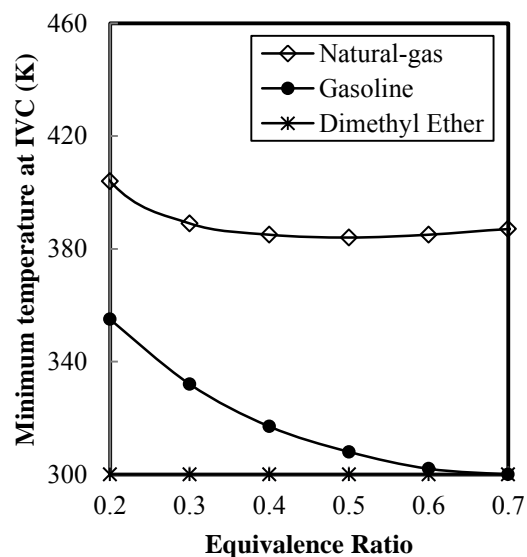
Fig.14 $T_{IVC,min}$ as a function of equivalence ratio for natural gas, gasoline and dimethyl ether

Figure 15 shows the minimum required temperature at IVC ($T_{ivc,min}$) as a function of engine speed which is varied from 800 to 4000 rpm at the increment of 800. When the engine speed is increased, the residence time for all reactions reduces, which means there is less time for the reactants to react with each other. This indicates the characteristic time of the reactions related to ignition must be shorter to make the chain branching happen. So the auto-ignition threshold is increased due to the shortened characteristic time. Then the minimum initial temperature is correspondingly increased to ensure successful auto-ignition. Although less relative heat transfer is expected at higher engine speed, the overall effect of increasing speed is still to increase the minimum initial temperature. Figure 16 shows the minimum required temperature at IVC ($T_{IVC,min}$) as a function of pressure at IVC for three different fuels. As initial pressure increases, a lower initial temperature is required for successful HCCI combustion because the auto-ignition threshold is reduced. This effect can be seen for iso-octane and natural gas cases.
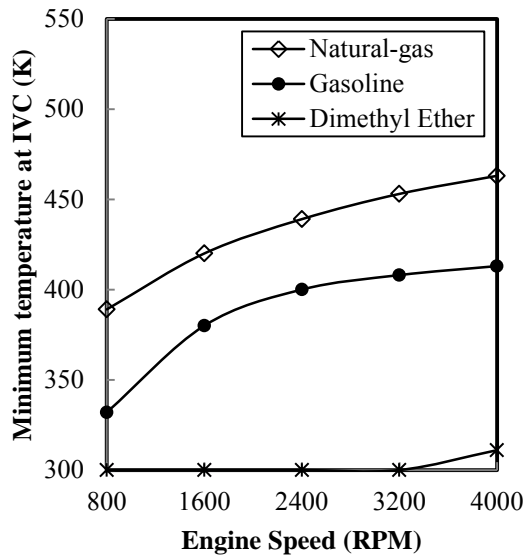
Fig.15 $T_{IVC,min}$ as a function of engine speed for natural gas, gasoline and dimethyl ether
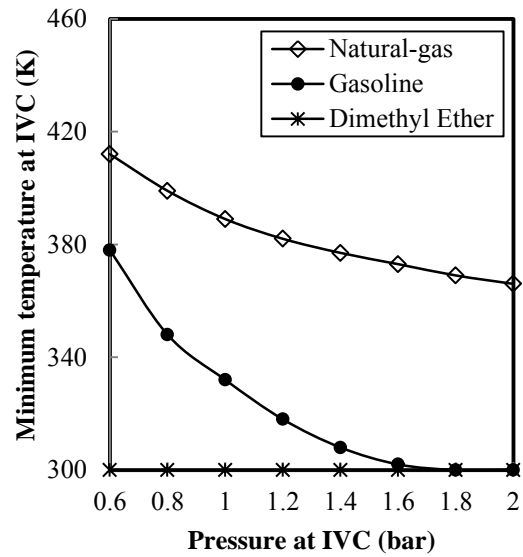
Fig.16 $T_{IVC,min}$ as a function of pressure at IVC for natural gas, gasoline and dimethyl ether

Figure 17 shows the temperatures and pressures at the start of combustion (SOC, defined as 1% heat release) at different operating conditions for all three fuels. At the start of combustion (SOC) for natural gas cases, the temperature approximately ranges from 1000K to 1200K and pressure ranges from 20bar to 60bar. In comparison, temperature and pressure ranges for gasoline is around 900K-1100K and 20bar to 55bar. The cases with DME as fuel have the lowest temperatures and pressures at SOC among three fuels, ranging from 750K to 900K and 20bar to 45bar. The differences in pressure and temperature at SOC between the fuels are again mainly due to their difference in the flammability, represented by the octane rating. Another observation from figure 17 is that for a specific fuel the pressure at SOC is more dispersed (ranging from 20bar to 60bar for natural gas) than the temperature at SOC for different conditions. This implies that the

pressure threshold for auto-ignition is not as important as the temperature threshold.
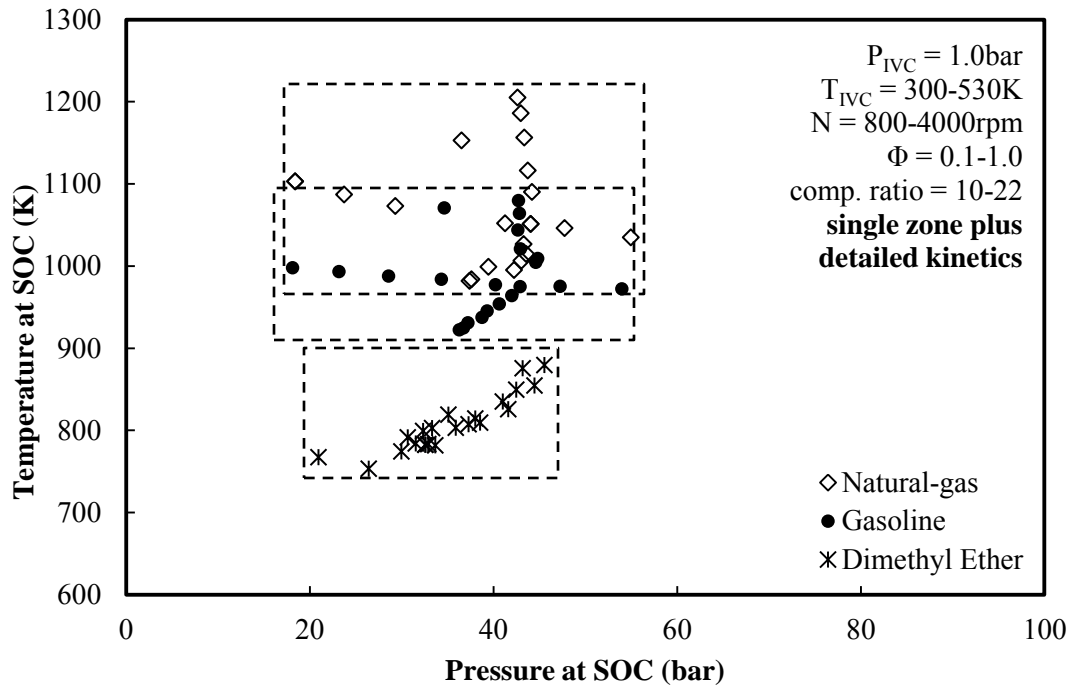
Fig.17 Temperature and pressure at start of combustion for different conditions and fuels

6.1.3 Best efficiency temperature approach

Similar to the approach used to find the minimal initial temperature, temperatures at IVC which lead to the best indicated efficiency are determined as $T_{IVC,beff}$ for different operating conditions and different fuels using the single-zone model, as shown in figure 18. The resolution of this $T_{IVC,beff}$ search process is again set to 1 K. $T_{IVC,beff}$, in theory, represents the intake temperature at IVC for the combustion phasing in HCCI engines while other operating conditions are kept unchanged.
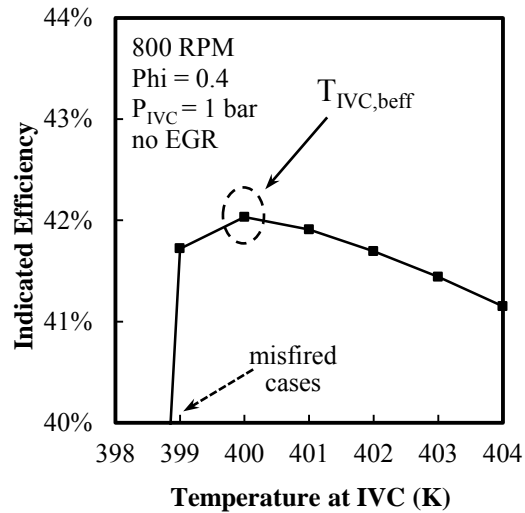
Fig.18 Determine the $T_{IVC,beff}$ by comparing indicated efficiencies
for a sweep of temperatures at IVC

6.1.4 <u>Effect of operating conditions on the best efficiency temperature</u>

In order to compare the effect of operating parameters for using natural gas and

gasoline as fuel in HCCI engines, the parametric studies shown in Table 9 are completed

and four parameters are examined: equivalence ratio, engine speed, EGR level, and

pressure at IVC. Figures 19-22 have shown the effect of each parameter.

Table 9 Parametric studies for investigating $T_{IVC,beff}$ in single-zone simulations

Cases	$T_{IVC,beff}$ Varying (K)	P@IVC (bar)	Equivalence Ratio	Engine speed (RPM)	EGR Fraction
Base case	$T_{IVC,beff}$	1.0	0.4	800	0
P_{IVC}	$T_{IVC,beff}$	0.6 – 2.0	0.4	800	0
Φ	$T_{IVC,beff}$	1.0	0.8 – 1.5	800	0
N	$T_{IVC,beff}$	1.0	0.4	800 – 4000	0
EGR	$T_{IVC,beff}$	1.0	0.4	800	0 – 0.4
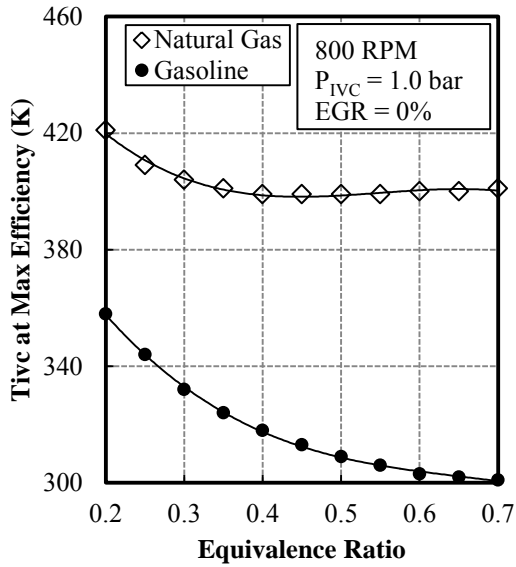
Fig.19 $T_{IVC,beff}$ as a function of equivalence ratio for natural gas and gasoline surrogate
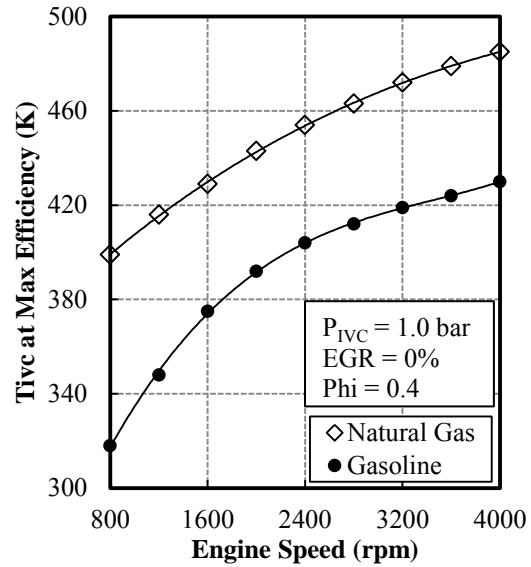
Fig.20 $T_{IVC,beff}$ as a function of engine speed for natural gas and gasoline surrogate
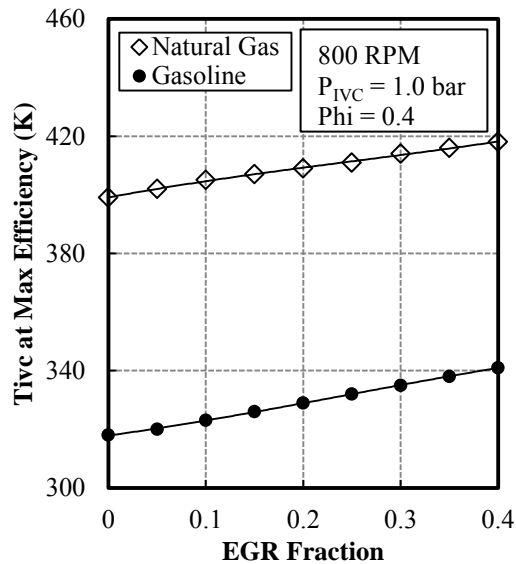
Fig.21 $T_{IVC,beff}$ as a function of EGR fraction for natural gas and gasoline surrogate
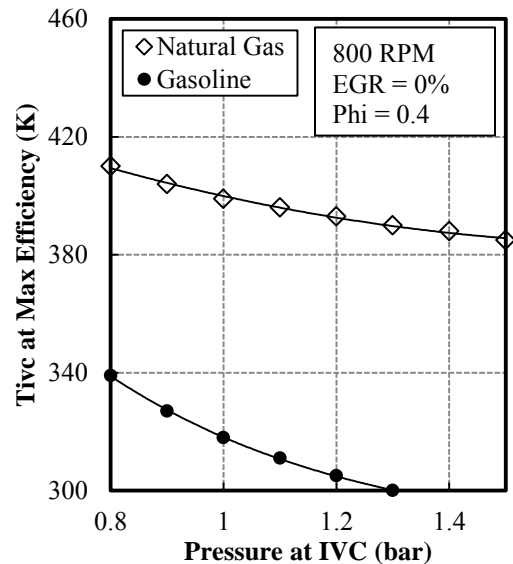
Fig.22 $T_{IVC,beff}$ as a function of pressure at IVC for natural gas and gasoline surrogate

In figure 19, $T_{IVC,beff}$ for natural gas and gasoline are shown as a function of equivalence ratio. The trend of $T_{IVC,beff}$ is generally similar to the trend of $T_{IVC,min}$, which is

that higher equivalence ratio reduces the temperature needed at best efficiency. The drop in $T_{IVC,beff}$ as equivalence ratio increases is more significant than for gasoline. This is because that the absolute mass of n-heptane (17% volume) in the gasoline, which has a much lower auto-ignition temperature, increases as the equivalence ratio goes up. More chemical energy is released by the early auto-ignition of n-heptane and facilitates the auto-ignition of iso-octane and toluene in the gasoline. This effect is relatively smaller for natural gas since the mass fractions of propane (6% volume) and butane (2% volume) are much less and their auto-ignition temperatures are closer to methane and ethane. Comparing with $T_{IVC,min}$, the $T_{IVC,beff}$ are around 20K higher for the natural gas cases and 5K higher for the gasoline cases. This further implies that natural gas HCCI engines have much higher requirement on the intake temperature which needs to be achieved either by intake heating or residual gas trapping.

Figure 20 shows the $T_{IVC,beff}$ for natural gas and gasoline as a function of engine speed. Quite similar trend as in the study of $T_{IVC,min}$, higher engine speed requires higher initial temperature to compensate for the reduction in the residence times of the reactions. The engine speed has almost the same effect on natural gas and gasoline as shortening of residence times equally applies to any reactions.

Figure 21 shows the $T_{IVC,beff}$ for natural and gasoline as a function of exhaust gas recirculation fraction. Here EGR is cooled to the same temperature as the initial temperature at IVC and equivalence ratio is kept constant for different EGR levels. At higher EGR, more combustion energy is absorbed by higher amount of CO_2 and H_2O

presented in the cylinder and therefore a higher initial temperature is needed to reach the best efficiency point.

Figure 22 shows the $T_{IVC,beff}$ for natural and gasoline as a function of pressure at IVC. Both for natural gas and gasoline, the increase in pressure at IVC reduces the temperature needed for best efficiency point. The main reason of this is that higher pressure increases the absolute mass of the species with lower auto-ignition temperatures (n-heptane in gasoline, propane and butane in natural gas) and these species release more chemical energy before the other species auto-ignite. Also high pressure could affect certain reactions which have strong pressure dependence.

6.1.5   Engine efficiencies for using natural gas in comparison with gasoline

This section continues to compare natural gas with gasoline in terms of the indicated efficiency and volumetric efficiency at the best efficiency point ($T_{IVC} = T_{IVC,beff}$) under various operating conditions. Some of the fuel properties are shown in Table 10.

Table 10 Lower Heating values, stoichiometric A/F ratios, and adiabatic flame temperatures for natural gas and gasoline surrogate

Fuel surrogate	Lower heating value (kJ/kmol)	Lower heating value [39] (kJ/kg)	Stoichiometric A/F ratio, molar	Stoichiometric A/F ratio, mass	Adiabatic flame temp.† (K)
Natural gas	9.35×10^5	49626	10.98	16.79	2596
Gasoline	4.71×10^6	43927	54.95	14.78	2636
† Constant volume and internal energy, stoichiometric, initially at 300K and 1bar					
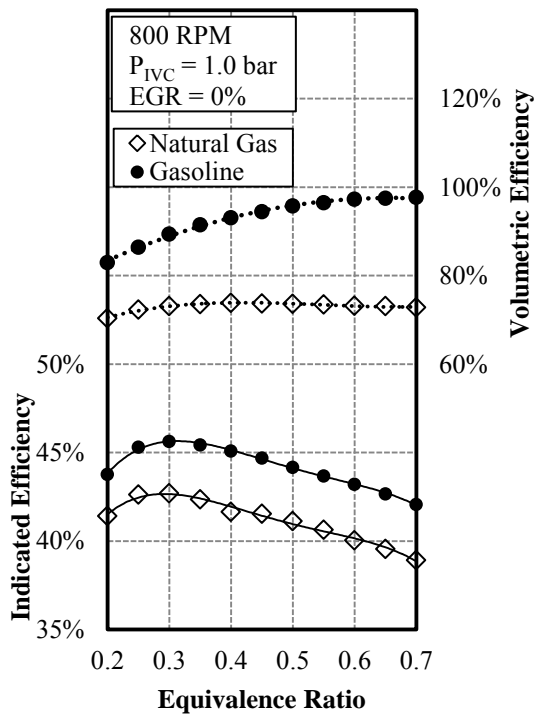
Fig.23 Indicated efficiency and volumetric efficiency as a function of equivalence ratio for natural gas and gasoline surrogate
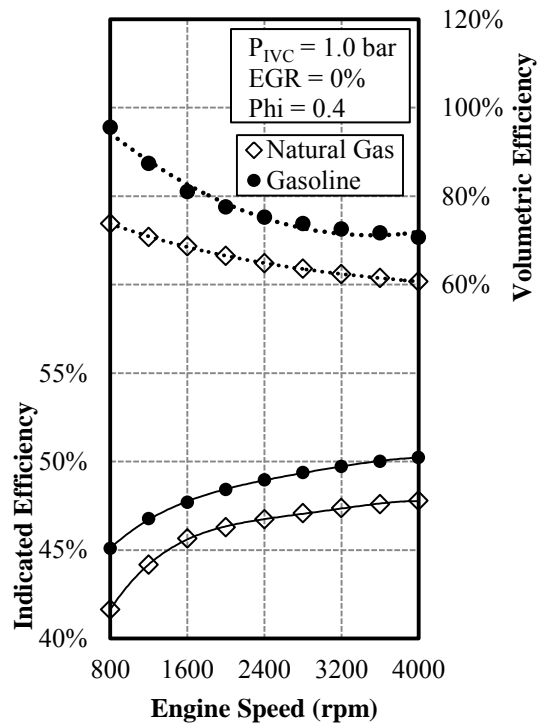
Fig.24 Indicated efficiency and volumetric efficiency as a function of engine speed for natural gas and gasoline surrogate

Figure 23 shows the indicated and volumetric efficiencies as functions of equivalence ratio for both natural gas and gasoline cases. For all of the equivalence ratios studied, about 3% difference in indicated efficiencies is observed between the two fuels. The efficiencies for the natural gas cases are lower largely due to the higher heat loss and lower specific heat ratio. Higher heat transfer is a direct result of higher $T_{IVC,beff}$ (recall figure 19) and the resulting higher combustion temperature. Lower specific heat ratio is caused by the higher mole fraction of the fuel species since natural gas has much lower molar stoichiometric air-fuel ratio than gasoline. A reduction of specific heat ratio reduces the amount of energy that can be extracted by the piston. Another observation from the plot

is that the indicated efficiency first goes up and then drop as equivalence ratio increases. At very low equivalence ratio, the chemical kinetics and combustion become slower and less complete which hurts the thermal efficiency. As the equivalence ratio increases, though combustion efficiency is improved, the heat loss as well as the fraction of heat loss out of total fuel energy is greater as result of a higher combustion temperature. In addition, higher equivalence ratio leads to lower specific heat ratio which reduces the thermal efficiency. So the indicated efficiency reaches a peak around Φ equal to 0.3. In terms of the volumetric efficiency, it is straightforward that the gasoline cases are higher and the differences are larger at higher equivalence ratios, since volumetric efficiency is strongly affected by the intake temperature. This observation poses another issue for using natural gas in HCCI engines which is the relatively lower torque output at the same equivalence ratio due to the low volumetric efficiency.

Figure 24 shows the indicated and volumetric efficiencies as a function of engine speed. The indicated thermal efficiency for both natural gas and gasoline increases as the engine speed increases. This increase is again related to the amount of heat transfer. Although $T_{IVC,beff}$ are higher (figure 20) at higher speeds, less time is allowed for transferring heat from the gas to the walls as the real time of one cycle become shorter as engine speed increases. The overall effect is to reduce the fraction of heat loss out of total fuel energy and to improve the thermal efficiency. The volumetric efficiency, however, decreases with the increase of engine speeds. Again this is directly dictated by the higher $T_{IVC,beff}$ needed at higher speeds. So running HCCI engines, either with gasoline or natural

gas, at higher speeds could improve thermal efficiency but at the penalty of torque output.

Figure 25 shows the indicated and volumetric efficiencies as a function of EGR fraction. The indicated thermal efficiency approximately remains nearly constant as the EGR level changes for both natural gas and gasoline cases. This might be attributed to the balance between lowered combustion temperature due to the EGR dilution effect and increased $T_{IVC,beff}$ (figure 21). Volumetric efficiency slightly drops as the EGR fraction increases and $T_{IVC,beff}$ increases.

Fig.25 Indicated efficiency and volumetric efficiency as a function of EGR fraction for natural gas and gasoline surrogate
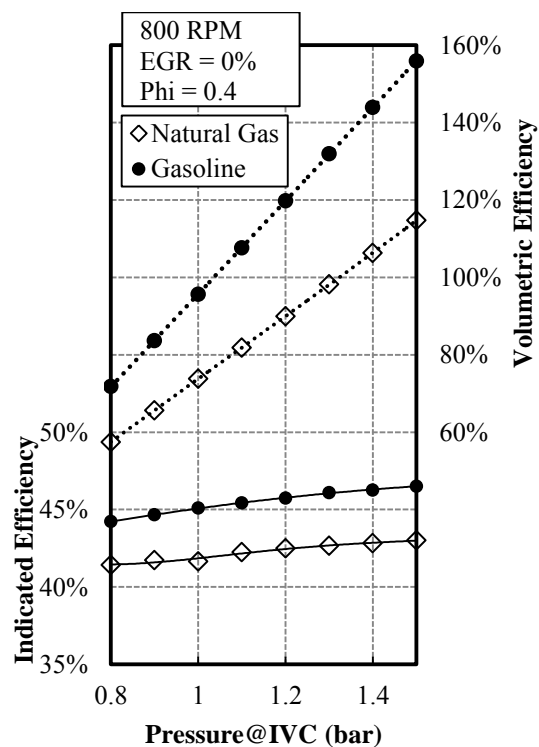
Fig.26 Indicated efficiency and volumetric efficiency as a function of pressure at IVC for natural gas and gasoline surrogate
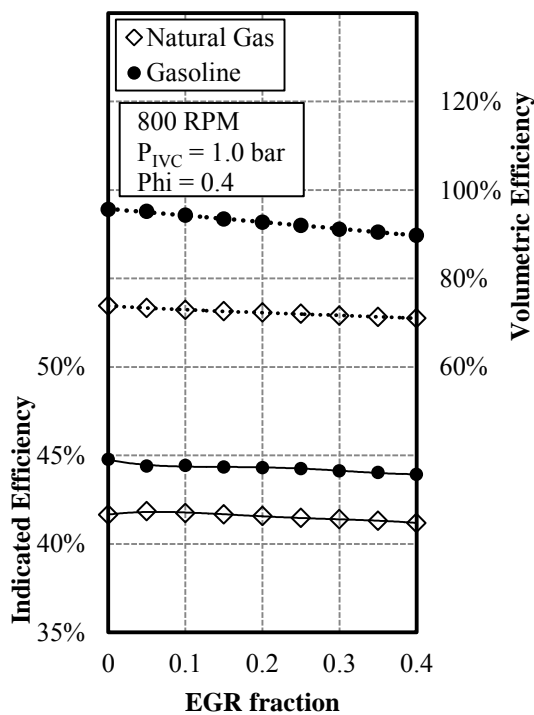
Figure 26 shows the indicated and volumetric efficiencies as a function of intake pressure at IVC. Having higher intake pressure slightly increases the indicated efficiency as a result of lower $T_{IVC,beff}$ and corresponding lower heat loss. Furthermore, increasing intake pressure greatly improves the volumetric efficiency due to the increase in the mass of air/fuel mixture. These results imply that intake boosting is an attractive option to have for HCCI engines fueled with natural gas or other high-octane fuels.

6.1.6   <u>Potential of using natural gas and dimethyl ether mixture</u>

As shown and discussed in the previous sub-sections, the biggest challenge for using natural gas in HCCI engines is the high intake temperature required for auto-ignition and complete combustion. Comparing with gasoline which has been used in current HCCI engines, natural gas needs 30-100K higher for intake temperature depending on the operating conditions. As analyzed, increased intake temperature causes the lower thermal efficiencies and volumetric efficiencies. So adding another fuel to reduce the auto-ignition requirements would make natural gas more practical to be used in HCCI engines.

Table 11 below lists the auto-ignition temperatures for some hydrocarbon species [40]. Among them dimethyl ether is one of the promising candidates for dual fuel operation with natural gas, not only because it has low auto-ignition temperature but also it can easily mix with natural gas as both of them are in gas phase at ambient condition. The potential advantage of using the mixture of DME and natural gas are shown and discussed in the following.

Table 11 Auto-ignition temperatures for various fuel species [40]

Species	Molecular formula	Auto-ignition temperature (K)	Phase at ambient condition
methane	CH_4	853	gas
ethane	C_2H_6	788	gas
propane	C_3H_8	743	gas
iso-butane	C_4H_{10}	735	gas
n-butane	C_4H_{10}	678	gas
iso-octane	C_8H_{18}	720	liquid
n-heptane	C_7H_{16}	488	liquid
toluene	$C_6H_5CH_3$	808	liquid
dimethyl ether	CH_3OCH_3	623	gas

Table 12 Fuel composition for natural gas and dimethyl ether mixture

Mole fraction	Dimethyl Ether (CH_3OCH_3)	Methane (CH_4)	Ethane (C_2H_6)	Propane (C_3H_8)	Butane (C_4H_{10})
100% natural gas	0	0.88	0.06	0.04	0.02
95% natural gas 5% dimethyl ether	0.05	0.836	0.057	0.038	0.019
90% natural gas 10% dimethyl ether	0.1	0.792	0.054	0.036	0.018
85% natural gas 15% dimethyl ether	0.15	0.748	0.051	0.034	0.017

Table 13 Lower heating values, stoichiometric A/F ratios, and adiabatic flame
temperatures for different blends of natural gas and dimethyl ether

Mixture (surrogate)	Lower heating value (kJ/kmol)	Lower heating value (kJ/kg) [39]	Stoichiometric A/F ratio, molar	Stoichiometric A/F ratio, mass	Adiabatic Flame Temp.† (K)
100% natural gas	9.35×10^5	49626	10.98	16.79	2596
95% natural gas 5% DME	9.83×10^5	48584	11.15	15.90	2600
90% natural gas 10% DME	1.03×10^6	47543	11.31	15.11	2605
85% natural gas 15% DME	1.07×10^6	46502	11.48	14.43	2609
† Constant volume combustion Stoichiometric mixture Initial temperature and pressure at 300K and 1bar					

Three proposed blends of natural gas and DME are summarized in Table 12, and the corresponding change in lower heating value and stoichiometric A/F ratio are shown in Table 13. Figures 27-30 show the change in $T_{IVC,beff}$ for the different blends at various operating conditions and figures 31-34 show how indicated efficiency and volumetric efficiency are affected by the different blends. These results are discussed in detail in the following.

Figure 27 shows the $T_{IVC,beff}$ as a function of equivalence ratio for pure natural gas and three proposed blends with DME. As the mole fraction of DME increases, lower $T_{IVC,beff}$ is required to reach the best efficiency point. The reduction in $T_{IVC,beff}$ decreases as equivalence ratio increases. This is mainly attributed to the increase in the mass of dimethyl ether with the increase of either the DME's mole fraction or the equivalence ratio.

More energy is released by the oxidation of DME in the early stage of auto-ignition and this increases the gas temperature as well as increases the radicals needed for methane, ethane, and other species to initiate the chain reactions. Here DME serves as the role of n-heptane in the gasoline surrogate. Figure 28 shows the corresponding indicated and volumetric efficiency as a function of equivalence ratio. Adding DME to natural gas does not improve the indicated thermal efficiency probably due to the balance between lowered initial temperature and the longer combustion duration and more heat loss associated with that. The volumetric efficiencies, however, are greatly improved by adding DME especially with higher DME fraction or at higher equivalence ratios. This would be the major advantage of adding DME into natural gas.
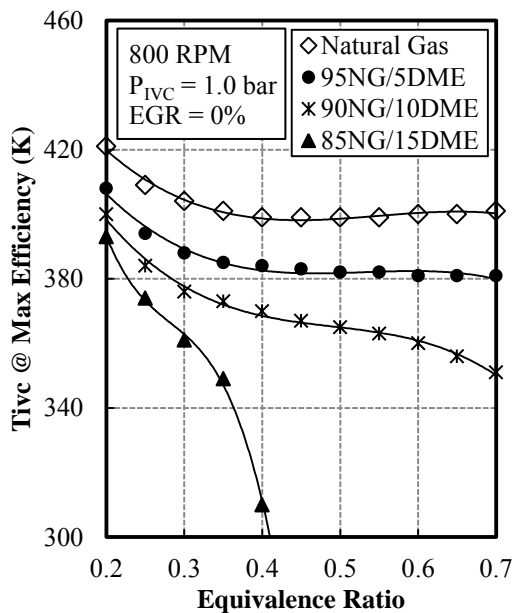
Fig.27 $T_{IVC,beff}$ as a function of equivalence ratio for natural gas and dimethyl ether mixtures
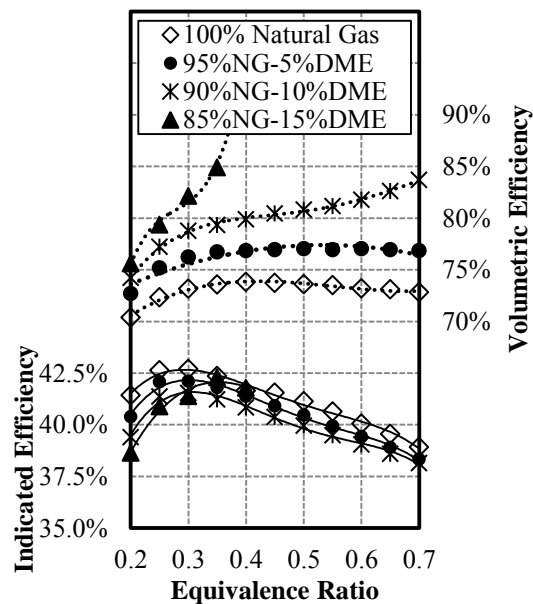
Fig.28 Indicated and volumetric efficiency as a function of equivalence ratio for natural gas and DME mixtures

Figures 29 and 30 continue to show the effect of adding DME on engine performance as functions for all engine speeds. In figure 29, the effect of engine speed is quite linear to the different blends studied except for the 15% DME case at 800 RPM. There exists a threshold of DME fraction and going beyond this threshold the initial temperature requirement will be greatly reduced. Too high DME fraction, however, is also not desirable since the $T_{IVC,beff}$ is going to be below the atmospheric temperature. For the efficiencies comparison in figure 30, consistent results are observed as the engine speed increases.

Fig.29 $T_{IVC,beff}$ as a function of engine speed for natural gas and dimethyl ether mixtures
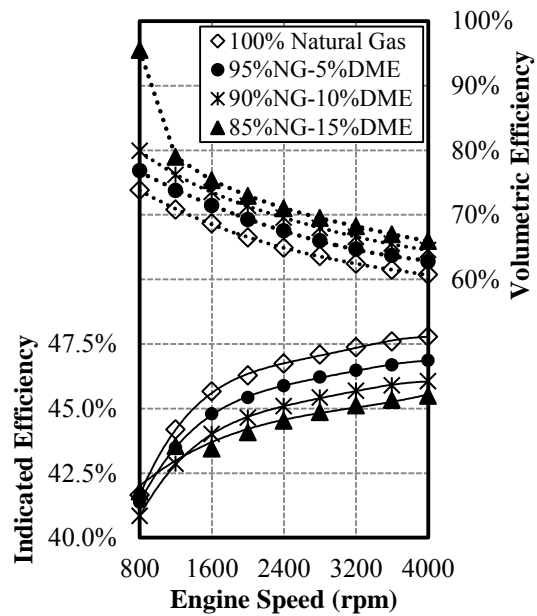
Fig.30 Indicated and volumetric efficiency as a function of engine speed for natural gas and dimethyl ether mixtures

Figure 31 shows the $T_{IVC,beff}$ for pure natural gas and different blends with DME as functions of EGR fraction varying from 0.1 to 0.4. As mentioned earlier in this section, not considering the intake heating effect, higher EGR fraction is going to increase $T_{IVC,beff}$. This effect remains true for different natural gas and dimethyl ether blends. When DME fraction is higher, this increase in $T_{IVC,beff}$ is more significant. This is because more mass of DME is replaced with exhaust gases for a given pressure and temperature at IVC. Figure 32 shows the indicated and volumetric efficiency for different blends of natural gas and DME as a function of EGR fraction. The volumetric efficiency increases with the increase of DME fraction and the decrease of EGR fraction. The indicated efficiency generally decreases as the DME fraction increases. When the DME fraction is greater than certain value (15% in volume here), however, the indicated efficiency is higher due to the dramatic drop of the initial temperature at IVC ($T_{IVC,beff}$). Similar results can be observed in other parametric studies.
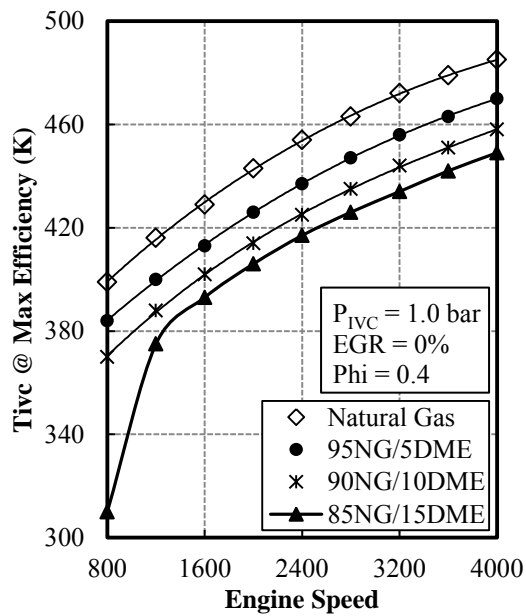
Fig.31 $T_{IVC,beff}$ as a function of EGR fraction for natural gas and dimethyl ether mixtures
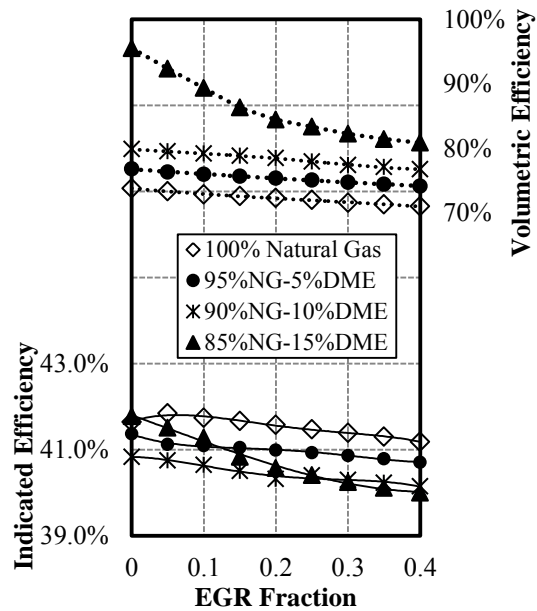
Fig.32 Indicated and volumetric efficiency as a function of EGR fraction for natural gas and dimethyl ether mixtures

Figure 33 shows the $T_{IVC,beff}$ as a function of pressure at IVC for various blends of natural gas and DME. Figure 34 shows the corresponding indicated efficiency and volumetric efficiency as a function of pressure at IVC. Similar to increasing equivalence ratio, increasing intake pressure increases the mass of dimethyl ether which then in turn leads to a reduction in intake temperature requirement. This effect is even greater for the cases with higher DME fractions. The 15% DME case, as an example, requires intake temperature to be about 360K for best efficiency when $P_{IVC} = 0.8$ bar, and requires almost no intake heating as the pressure at IVC increases to 1.0 bar, which is a reduction of 60K in $T_{IVC,beff}$. Comparably in figure 34, the volumetric efficiency and indicated efficiency increase with pressure at IVC and this increase is greater for higher DME fraction cases.
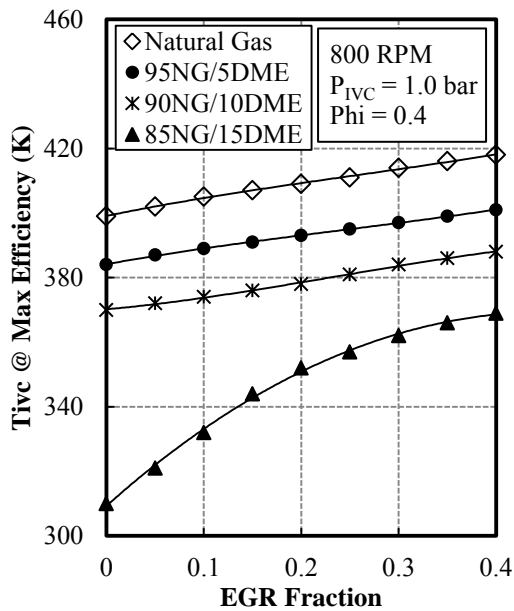
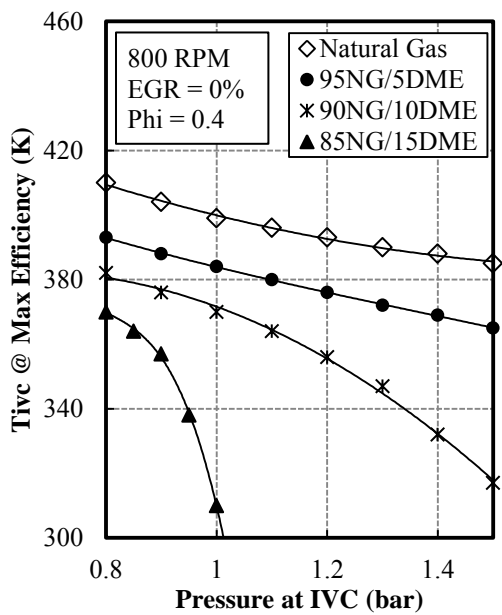**Fig.33** $T_{IVC,beff}$ as a function of pressure at IVC for natural gas and dimethyl ether mixture
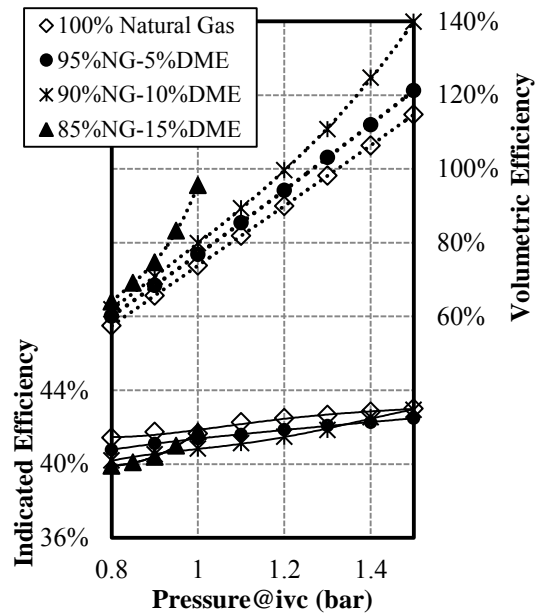
Fig.34 Indicated and volumetric efficiency as a function of pressure at IVC for natural gas and dimethyl ether mixture

6.1.7   NO$_x$ emissions characteristics of natural gas HCCI engines

At best efficiency point

Figures 35-38 show the effects of operating parameters on NO$_x$ emission characteristics at the best efficiency point, i.e. T$_{IVC}$ is equal to T$_{IVC,beff}$. Figure 35 shows the NO$_x$ emission corrected at 15% O$_2$ as a function of equivalence ratio for natural gas, gasoline, and different blends of natural gas and DME. First, the NO$_x$ concentration of all the fuel and fuel blends studied increases as the increase of equivalence ratio. As the equivalence ratio increases, the combustion temperature increases consequently and therefore the NO$_x$ formation via thermal mechanism is greatly enhanced. This increase in the NO$_x$ concentration, from a few ppm to several thousand ppm as the equivalence ratio changes from 0.2 to 0.7, is dramatic for all the fuels presented in the plot. Secondly, different fuels produce different NOx emission at the same equivalence ratios. The calculation using pure natural gas shows the highest NO$_x$ prediction, while the calculation using gasoline shows the lowest NO$_x$. As more and more DME is present in the natural gas/DME blend, less NO$_x$ prediction is observed. The difference in NO$_x$ emission due to the fuels could be largely attributed to the difference in T$_{IVC,beff}$ for different fuels. The natural gas cases require the highest T$_{IVC,beff}$, the gasoline cases need lowest T$_{IVC,beff}$, and adding DME to natural gas lowers T$_{IVC,beff}$ (as observed in figures 19 & 27 in this section). As the combustion temperature is in direct proportion to the initial temperature (T$_{IVC}$), the case with higher initial temperature will have higher NO$_x$ production. Similar trends are found in figures 36-38 in the following.
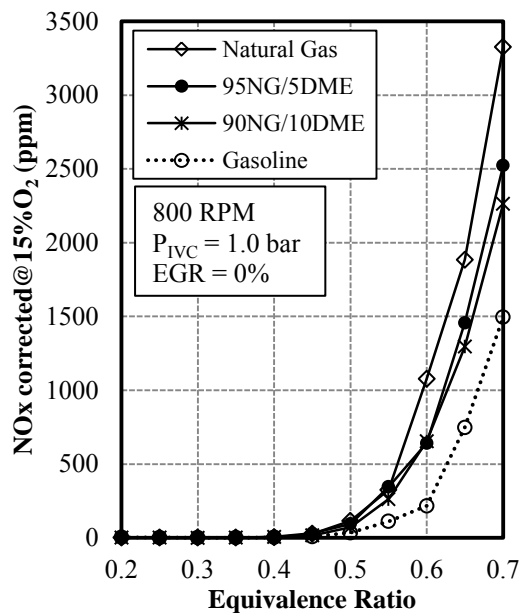
Fig.35 NO$_x$ concentration corrected at 15% O$_2$ as a function of equivalence ratio for various fuels and fuel blends
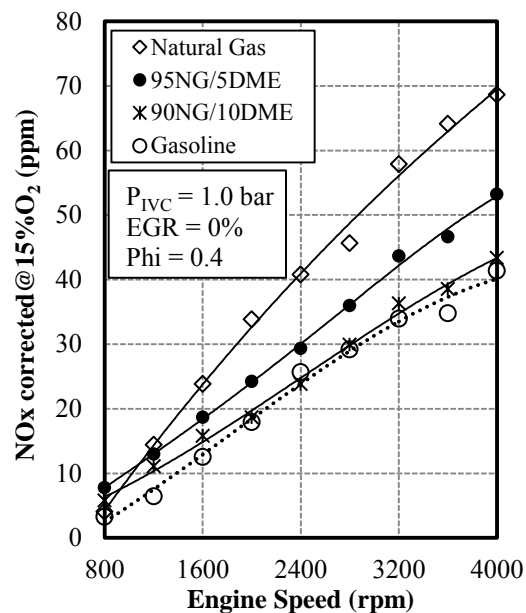
Fig.36 NO$_x$ concentration corrected at 15% O$_2$ as a function of engine speed for various fuels and fuel blends

Figure 36 shows the NO$_x$ emission corrected at 15% O$_2$ as a function of engine speed for natural gas, gasoline, and different blends of natural gas and DME. As the engine speed increases, the NO$_x$ prediction equally increases for all the fuels studied. There are two factors affecting the NO$_x$ formation while the engine speed is changing. On the one hand, higher engine speed causes higher T$_{IVC,beff}$ and less time for heat transfer (figures 20 & 29) which will lead to the increase in combustion temperature and NO$_x$ formation. On the other hand, higher engine speed leads to less residence time for NO$_x$ formation reactions which tends to reduce NO$_x$ concentration. The overall effect with these two factors competing with each other is still to increase the NO$_x$ with the increase in engine speed.
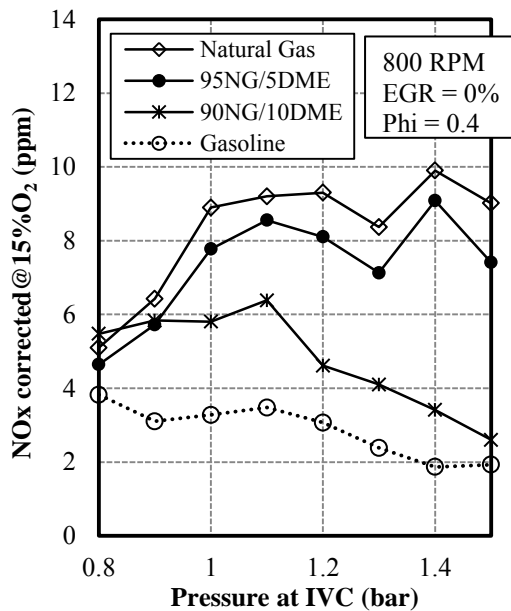
Fig.37 NO$_x$ concentration corrected at 15% O$_2$ as a function of pressure at IVC for various fuels and fuel blends
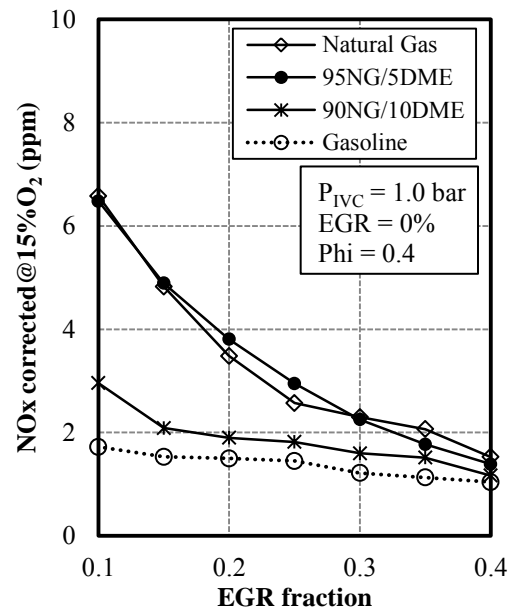
Fig.38 NO$_x$ concentration corrected at 15% O$_2$ as a function of EGR fraction for various fuels and fuel blends

Figure 37 shows the NO$_x$ emission corrected at 15% O$_2$ as a function of engine speed for natural gas, gasoline, and different blends of natural gas and DME. The effect of intake pressure on NO$_x$ is related to the T$_{IVC,beff}$ and the change in combustion phasing. These two factors almost balance out under the operating condition studied and make the effect of intake pressure on NO$_x$ relatively weak.

Figure 38 shows the NO$_x$ emission corrected at 15% O$_2$ as a function of engine speed for natural gas, gasoline, and different blends of natural gas and DME. The NO$_x$ emission reduces as the EGR fraction increases. Since the level of NO$_x$ for the baseline case is relatively low, the effect of EGR seems not significant. The EGR is very effective in reducing combustion temperature and NO$_x$ emission at other operating conditions.

<u>Contributions of different NO mechanisms</u>

As described in section 4.6, there are three major mechanisms responsible for most of the NO formation. To illustrate the importance of these NO mechanisms, using the single zone simulations, figures 39-42 show the percent contributions of the different NO mechanisms to the total NO emissions at different operating conditions. The operating conditions varied in this parametric study are summarized in Table 14.

Figure 39 shows the percent contribution of thermal, prompt, and nitrous oxides intermediate mechanism to the total NO emission as a function of engine speed. As engine speed increases, based on the kinetics, the ignition timing is retarded and the imep values at different engine speeds are different. Figure 40 shows similar results as a function of initial pressure at intake valve closing. As observed in these plots, the NO production from thermal mechanism accounts for over 70% for most of the conditions studied. The N_2O intermediate mechanism accounts for up to 30% of the total NO and is the second most important NO source. This could be attributed to the use of relatively lean mixtures (Φ=0.4) in the examined conditions. Because of the lean condition and no local rich zones from the homogeneous charge, prompt NO mechanism becomes insignificant in these conditions and only accounts for around 5% of the total NO. As observed, these three mechanisms do not always add up to 100%. Since not all the NO related reactions are categorized into these three mechanisms, other reactions still contribute to the formation or destruction of NO. But their contributions are relative small and probably too trivial to be grouped as another mechanism.

Table 14 Parametric studies for investigating NO mechanisms in single-zone simulations

Cases	P@IVC (bar)	Equivalence Ratio	Engine speed (RPM)	EGR Fraction	Other Parameters
Base case	1.0	0.4	1000	0	Same engine spec:
P_{IVC}	0.6 – 1.5	0.4	1000	0	Bore = 112mm Stroke = 115mm
Φ	1.0	0.3 – 1.0	1000	0	Comp. Ratio = 18.8
N	1.0	0.4	500 – 3000	0	Homogeneous mixture Simulation starts from
EGR	1.0	0.4	1000	0 – 0.4	IVC to EVO

Fig.39 Percent contributions of different NO mechanisms to the total NO emission as a function of engine speed at Φ=0.4, P_{IVC}=1.0, and no EGR
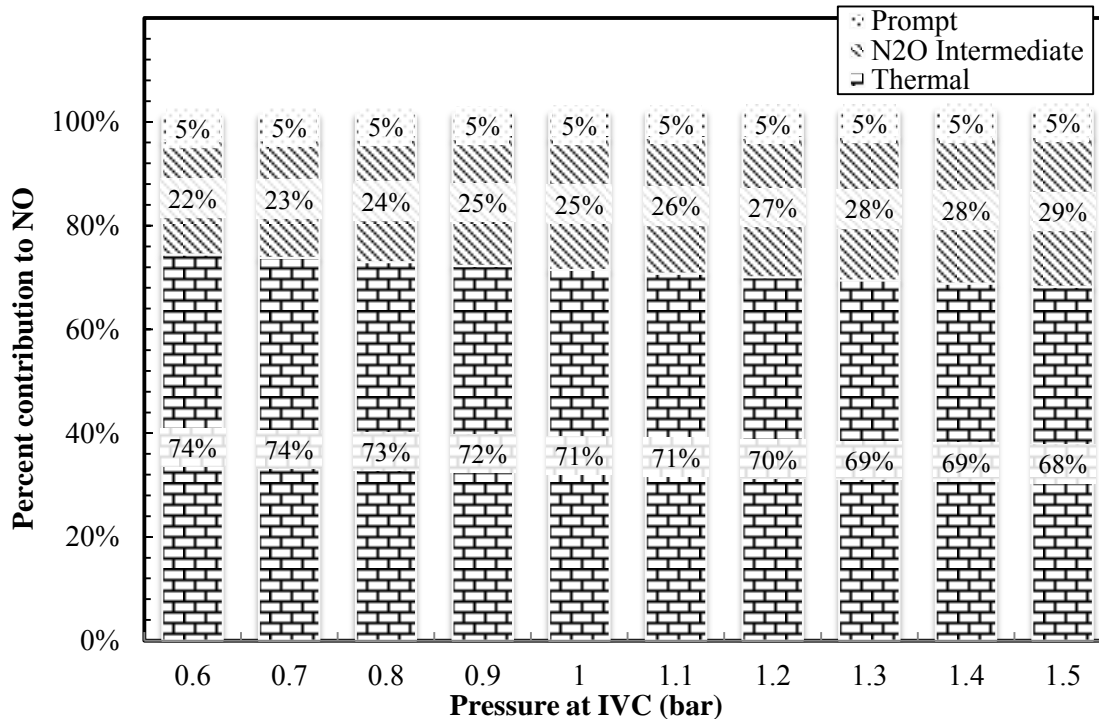
Fig.40   Percent contributions of different NO mechanisms to total NO emission as a function of pressure at IVC at Φ=0.4, RPM=1000, and no EGR

The change in the operating parameters can also affect, to some extent, the contributions of different NO mechanisms. In figure 40, as an example, increasing the initial pressure at intake valve closing increases both the absolute value and the percentage contribution of the NO from N_2O intermediate mechanism. This is because the N_2O intermediate mechanism involves a three-way collision reaction which is enhanced at higher pressure.

In figures 41 and 42, the effects of equivalence ratio and EGR level on the different mechanisms have also been examined. The increase in equivalence ratio restrains the importance of N_2O intermediate mechanism, while enhancing the thermal and prompt mechanisms as the mixture becomes richer, and the gas temperature becomes higher.

Higher EGR percentage greatly reduces the absolute value of NO from each mechanism due to the dilution effect and the lowered temperature. However, the increase in EGR level slightly increases the contribution of N_2O mechanism which is less dependent on temperature than the other mechanisms.
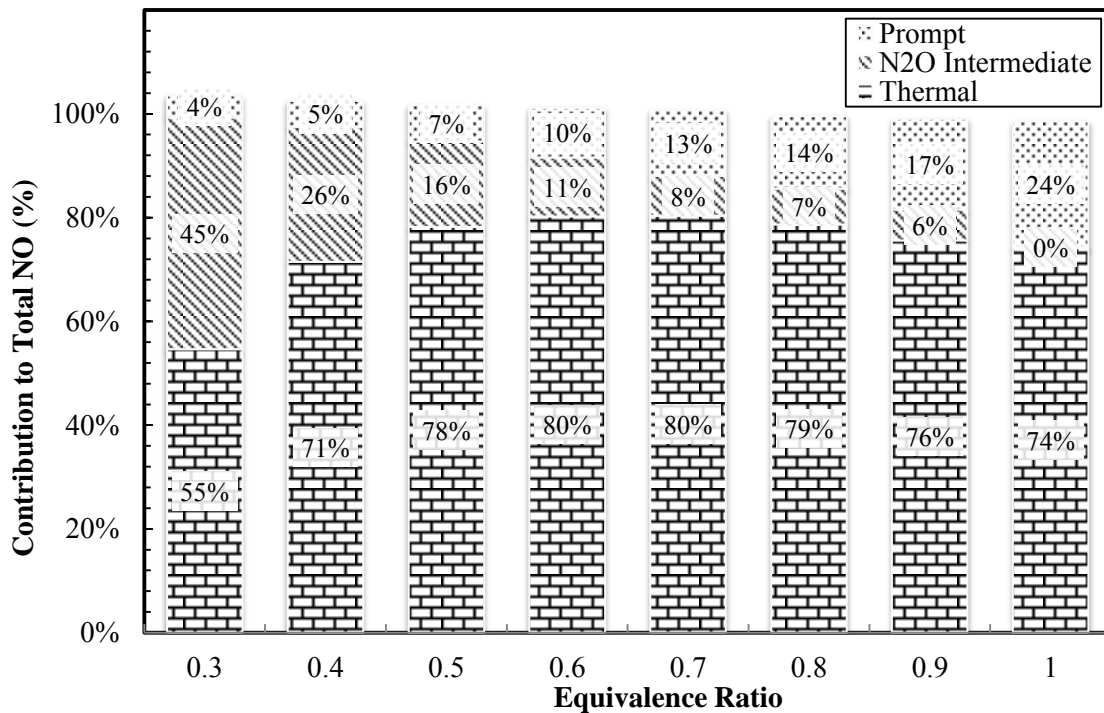
Fig.41 Percent contributions of different NO mechanisms to total NO emission as a function of equivalence ratio at RPM=1000, P_{IVC}=1.0, and no EGR
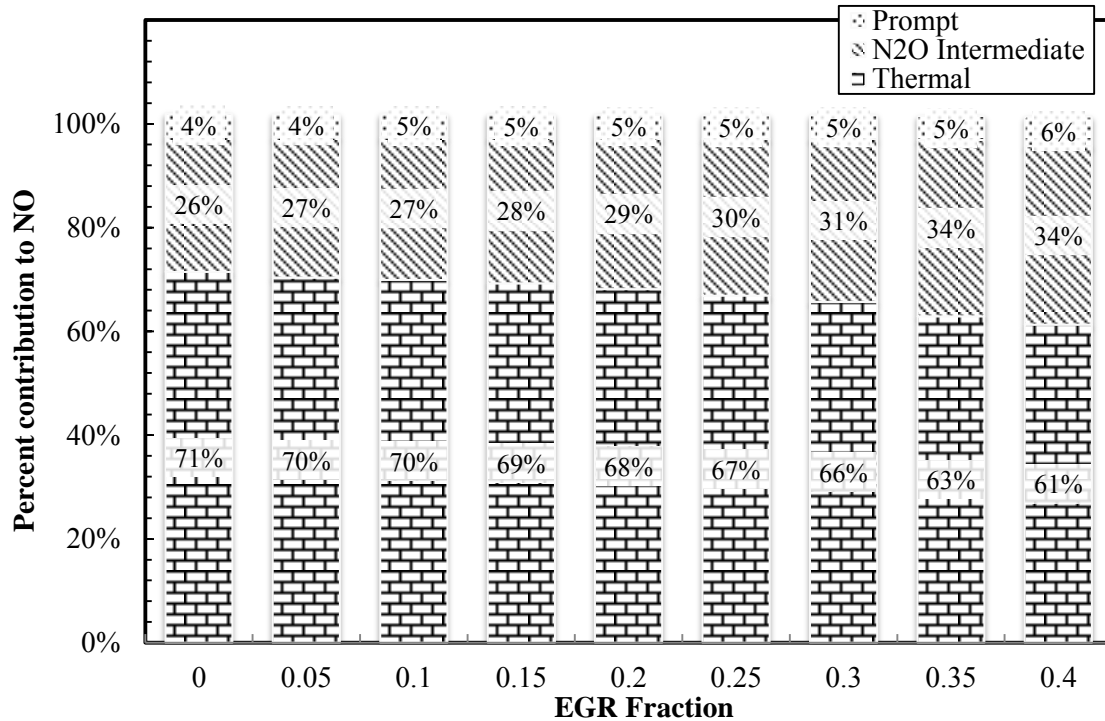
Fig.42 Percent contributions of different NO mechanisms to total NO emission as a function of EGR fraction at $\Phi=0.4$, $P_{IVC}=1.0$, and RPM=800

6.2 Results from cold-flow CFD and multi-zone simulations

In section 6.2, results from the non-reacting computational fluid dynamics simulations and multi-zone simulations have been presented and discussed. First, the in-cylinder distributions of temperature and equivalence ratio at the baseline case are shown, followed by a few parametric studies showing the effect of operating parameters on these two distributions. Then the multi-zone simulation results are shown and compared with the single-zone results to illustrate the effect of temperature and equivalence ratio stratifications on HCCI combustion.

6.2.1   In-cylinder distributions of temperature and equivalence ratio

Contrary to the homogeneous assumption of the single-zone model, the temperature and species concentrations in the cylinder are usually not uniform in real engines. As described in section 4, by employing the two-dimensional non-reacting CFD model, the in-cylinder distributions of temperature and equivalence ratio are obtained.
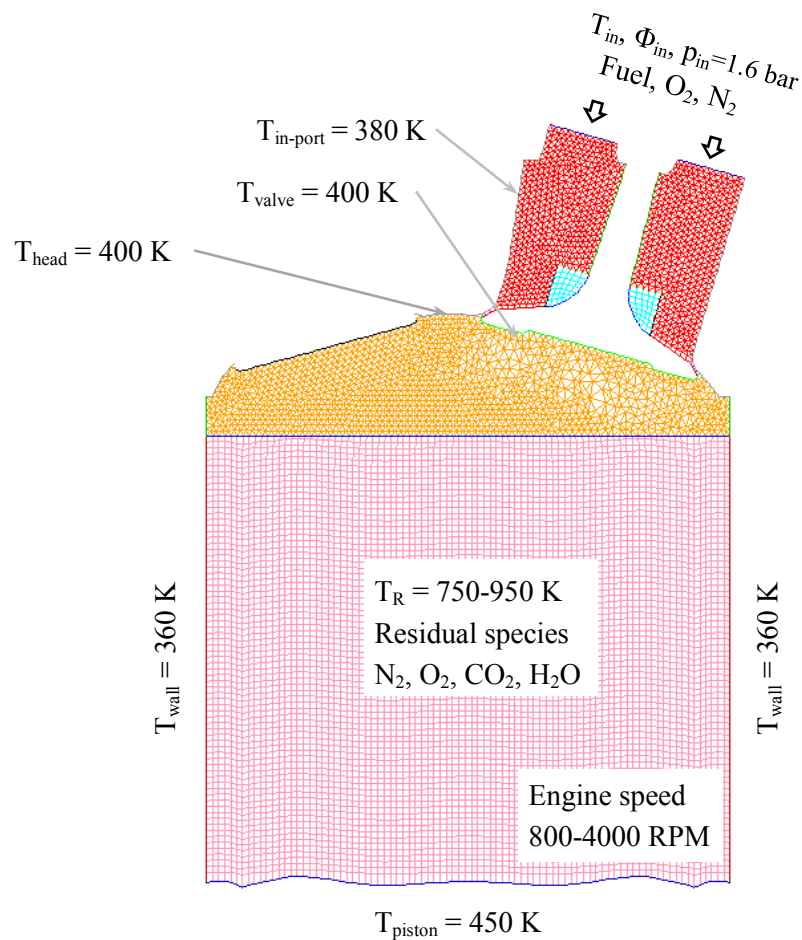
Fig.43   Initialization of the 2-D non-reacting CFD simulation
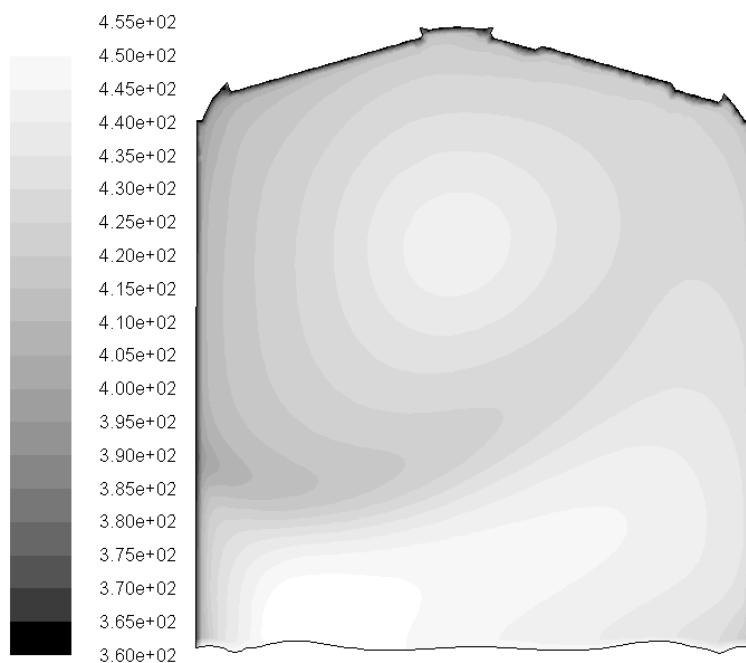
Fig.44 In-cylinder distribution of temperature at IVC from the two-dimensional non-reacting CFD simulation, at RPM=800, Φ_{in}=0.45, T_{in}=380K, and T_R=800K
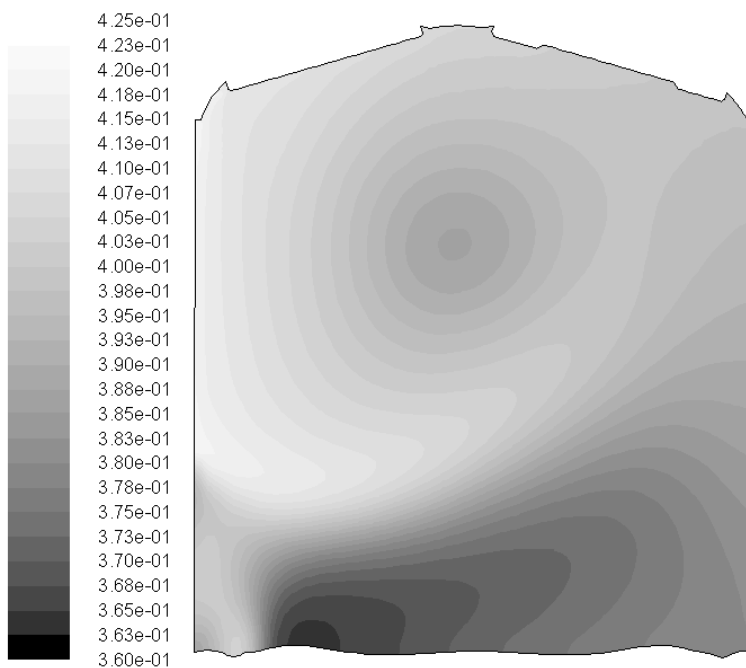
Fig.45 In-cylinder distribution of equivalence ratio at IVC from the 2-D non-reacting CFD simulation, at RPM=800, Φ_{in}=0.45, T_{in}=380K, and T_R=800K

Figure 43 shows the initial setup of the two-dimensional non-reacting CFD simulation. The temperatures at different walls are estimated to be different but remain constant during the simulation. Inlet properties such as the inlet temperature, inlet pressure, and species concentrations are defined. Initial conditions such as the residual temperature and species inside the cylinder are also defined.

Figures 44 and 45 show the in-cylinder distributions of temperature and equivalence ratio at IVC from the two-dimensional non-reacting CFD simulations. By dividing the temperature into several groups and calculating the area that the temperature groups occupy, the distributions of the temperature are then obtained and ready to be employed as inputs in the multi-zone model. Similar processes are done for obtaining the distribution of the equivalence ratio. Figures 46 and 47 show the distribution of temperature and equivalence ratio at 800 RPM, inlet equivalence ratio of 0.45, inlet temperature of 380K, and residual temperature of 800K. The temperature ranges from 360K to 450K, averages at 427K, and is divided into 19 zones. In the near wall region, although there is small volume, the temperature ranges from 360 to 400K. Then those temperature groups ranging from 360K to 400K (in figure 46) represent the zones in the near wall boundary layer. Similarly, the equivalence ratio ranges from 0.36 to 0.42 which is grouped into 11 zones, and the average equivalence ratio is 0.394.
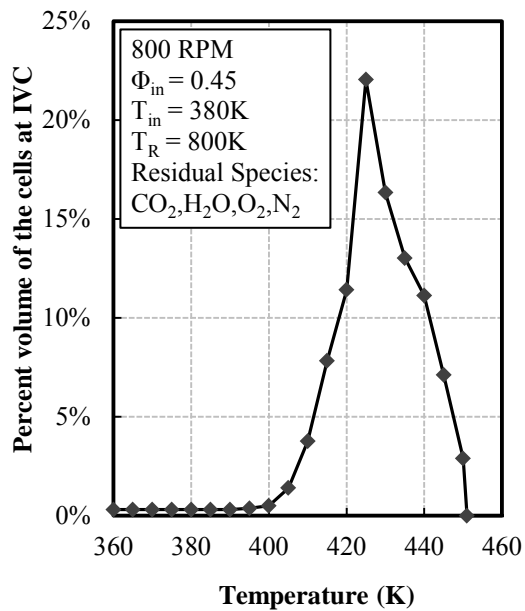
Fig.46 Percent volume of the cells as a function of temperature group at IVC
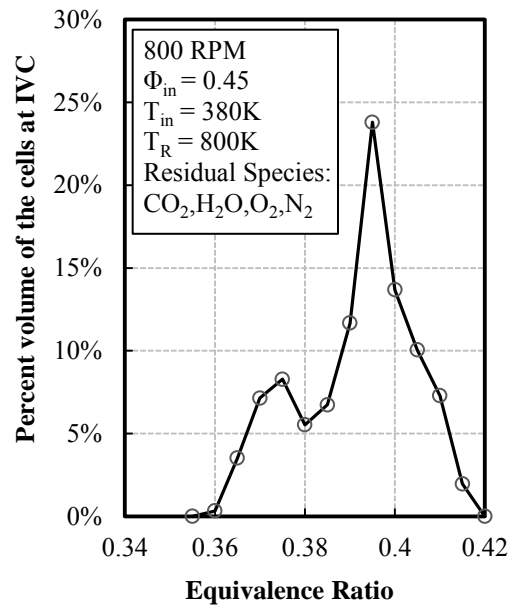
Fig.47 Percent volume of the cells as a function of equivalence ratio group at IVC

6.2.2   Effect of operating parameters on the distribution

The effect of engine speed and residual gas temperature on the temperature distribution and the effect of inlet equivalence ratio on the species concentration distribution are shown in figures 48 to 50.

Figure 48 shows the effect of engine speed on the in-cylinder temperature distribution. As the engine speed increases, the average temperature at IVC increases, and the temperature in the cylinder tends to be more stratified. This could be attributed to less heat loss to the walls and higher inlet velocity at higher engine speed. The change in the temperature distribution very likely will affect the HCCI combustion phasing and other characteristics. The equivalence ratio distribution remains about unaltered as the engine

speed changes and therefore is not shown here.

Figure 49 shows the effect of residual gas temperature on the in-cylinder temperature distribution. Similar to the effect of engine speed, as the residual gas temperature increases the temperature stratification level is higher and the average temperature is higher as well. About 200K increase in the residual gas temperature causes 7K increase in the average in-cylinder temperature. The impact, however, is much smaller than the one of engine speed. The residual gas temperature doesn't have a strong effect on equivalence ratio.

Figure 50 shows the effect of inlet equivalence ratio (Φ_{in}) on the in-cylinder equivalence ratio distribution. Higher Φ_{in} tends to produce wider equivalence ratio at IVC as the standard deviation of Φ increases from 0.010 to 0.014. In addition, the mass averaged equivalence ratio at IVC is always about 0.05 lower than Φ_{in}, which is due to the dilution of the residual gas already present in the cylinder at IVC.
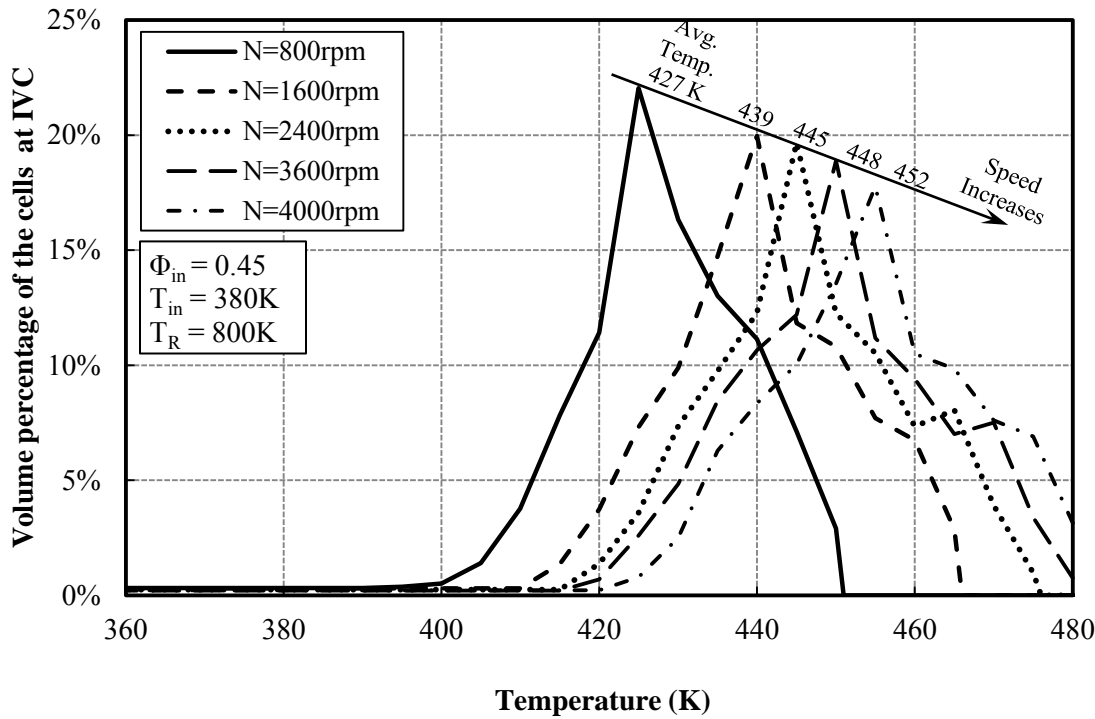
Fig.48 Volume fraction of the cells as a function of temperature category at various engine speeds
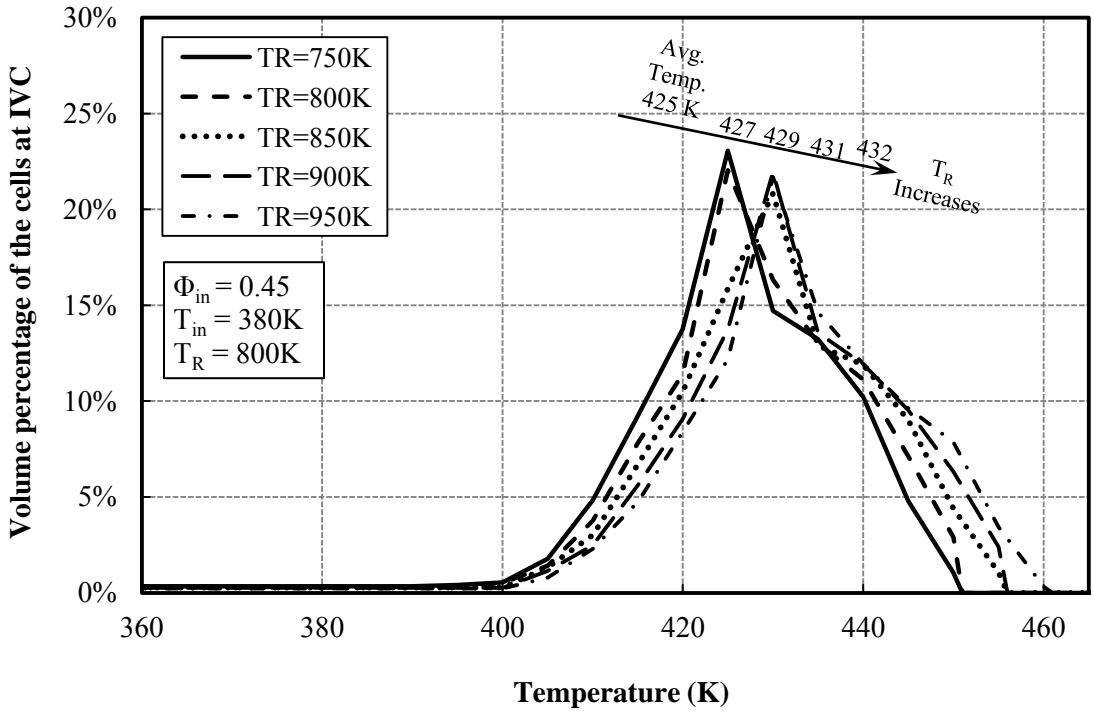
Fig.49 Volume fraction of the cells as a function of temperature category for various residual gas temperatures
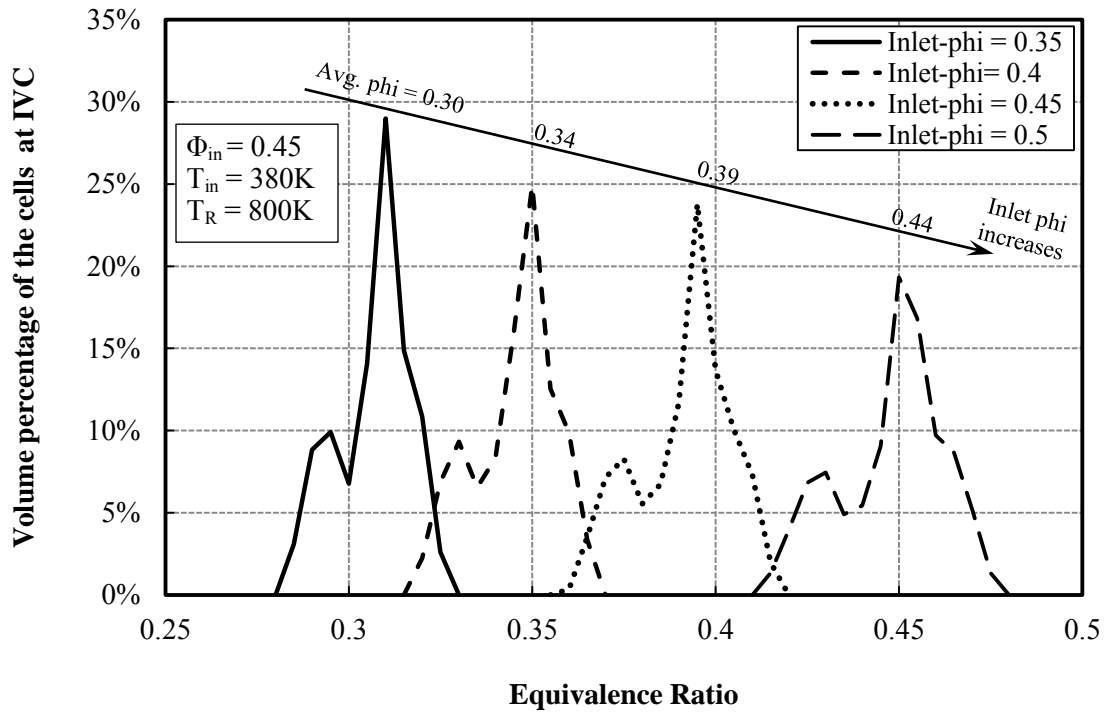
Fig.50 Volume fraction of the cells as a function of equivalence ratio category for various inlet equivalence ratio

6.2.3 Effect of T and Φ stratifications on HCCI combustion

As described in the previous sub-section, by performing the two-dimensional non-reacting CFD simulations the distributions of temperature and equivalence ratio are obtained. In this sub-section, these distributions are fed to the multi-zone model and the effect of these stratifications on HCCI combustion is studied by comparing with the single-zone simulation which employs the homogeneous assumption.
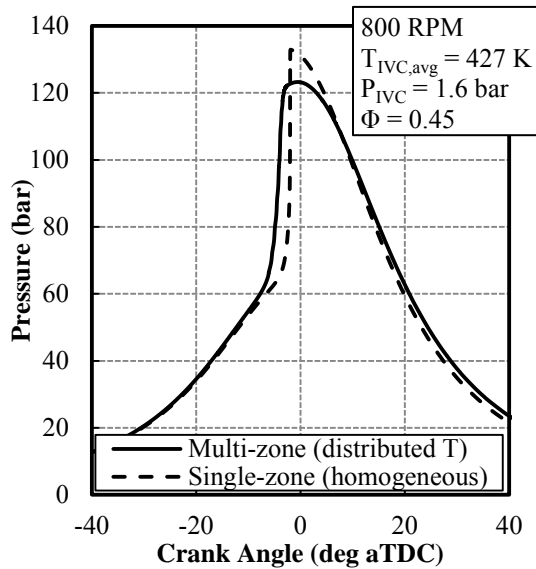
Fig.51 Predicted pressure profiles from single-zone and multi-zone with temperature stratification only
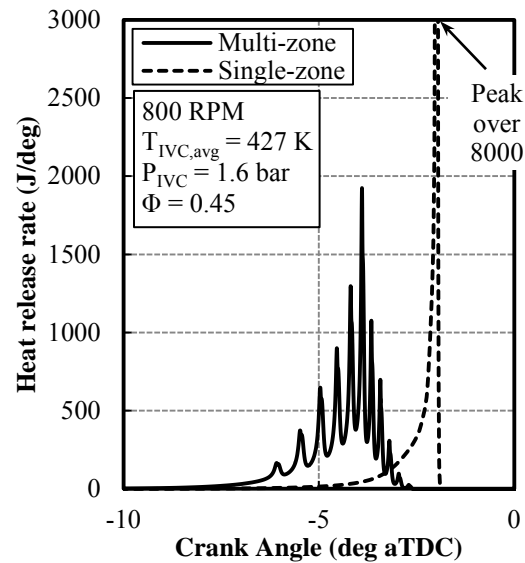
Fig.52 Predicted heat release rates from single-zone and multi-zone with temperature stratification only

Figures 51-55 show the comparison between the single-zone results and the multi-zone simulation with temperature distribution only (equivalence ratio was homogeneous). Figure 51 shows the predicted pressures as a function of crank angle for both the single-zone and multi-zone results. Figure 52 shows the heat release rates as a function of crank angle. Due to the temperature distribution, the multi-zone prediction shows earlier start of combustion and longer combustion duration. The zones with different initial temperatures will auto-ignite at different timings, which spreads the heat release out. This effect will be discussed later in detail. In addition, the peak pressure and peak heat release rate from the multi-zone simulation are also lower than the single-zone results. Figure 53 shows the average temperature as a function of crank angle. Figure 54 shows the NO_x concentration as a function of crank angle. The predicted NO_x concentration from the

multi-zone simulation is about 100 ppm lower than that from the single-zone simulation. Although for the multi-zone results the combustion duration is longer which leaves more time for NO_x formation, the reduction in average temperature and peak temperature still dominates and leads to less NO_x prediction.

Figure 55 shows different zonal temperatures as a function of crank angle. As mentioned, earlier ignitions and higher peak temperatures are observed for the zones with higher initial temperatures. Some zones, such as zone 16 and 19 in figure 55, misfire as the initial temperatures are too low for them to auto-ignite misfire. This is a closer approximation to the case in real HCCI engines in which the fuel usually is not burned simultaneously and completely.
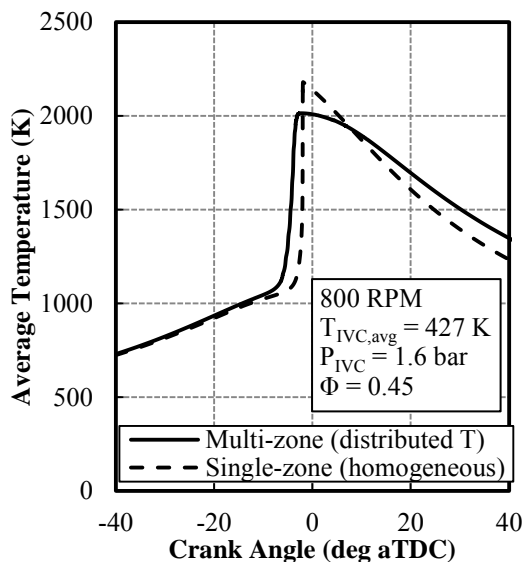
Fig.53 Predicted temperature profiles from single-zone and multi-zone with temperature stratification only
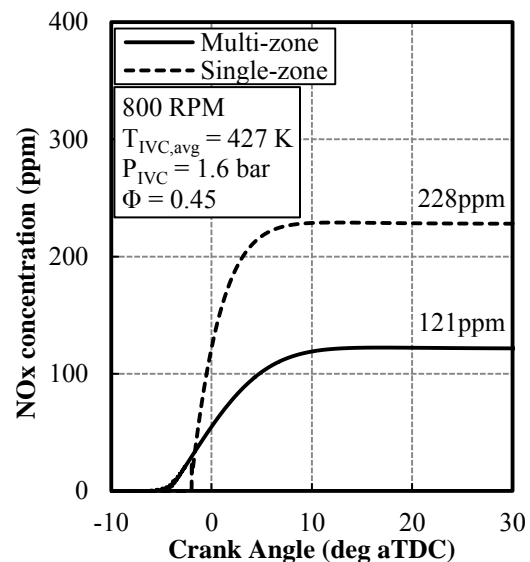
Fig.54 Predicted NO_x emissions from single-zone and multi-zone with temperature stratification only
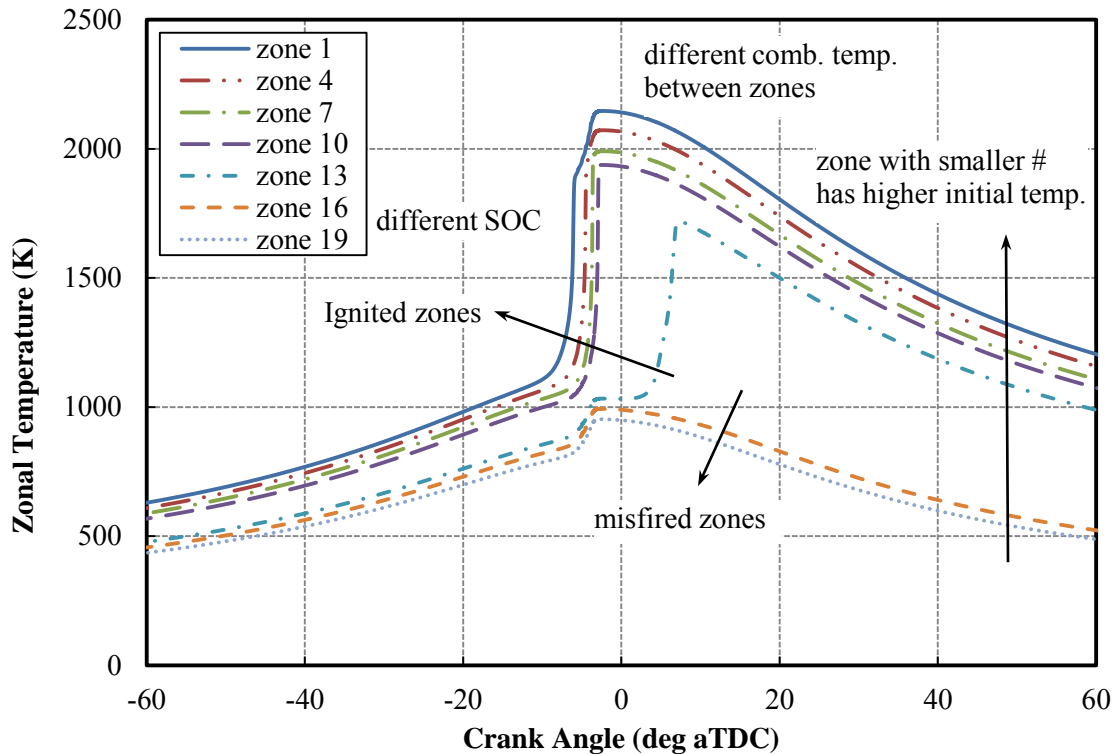
Fig.55   Zonal temperature histories as a function of crank angle for the multi-zone model with temperature distribution only at RPM=800, $\Phi = 0.45$, $T_{IVC,avg}$=427 K, and P_{IVC}=1.6 bar.

Figures 56-60 show the comparison between the single-zone simulation and the multi-zone simulation with equivalence ratio distribution only (uniform gas temperature). Figure 56 shows the predicted pressure as a function of crank angle. Figure 57 shows the heat release rate as a function of crank angle. The pressure and heat release curves from the multi-zone simulation are almost identical of the single-zone results and there is only slight difference in the combustion phasing. This implies that the stratification of equivalence ratio doesn't have a strong effect on the HCCI combustion. Figures 58 and 59 show the average temperature and NO_x concentration as a function of crank angle. Although the two average temperature profiles looks almost the same, the NO_x prediction from the

multi-zone model is about 35 ppm higher than that from the single-zone simulation. This is mainly attributed to non-linear effect of the temperature on NO_x formation. The zones with higher initial temperatures will have higher peak temperature and longer high temperature periods than the zones with lower initial temperatures, as shown in figure 60. Thus the NO_x concentration in these zones will be higher than that of the single-zone, and the reduction in NO_x formation in lower temperature zones cannot fully compensate that increase.
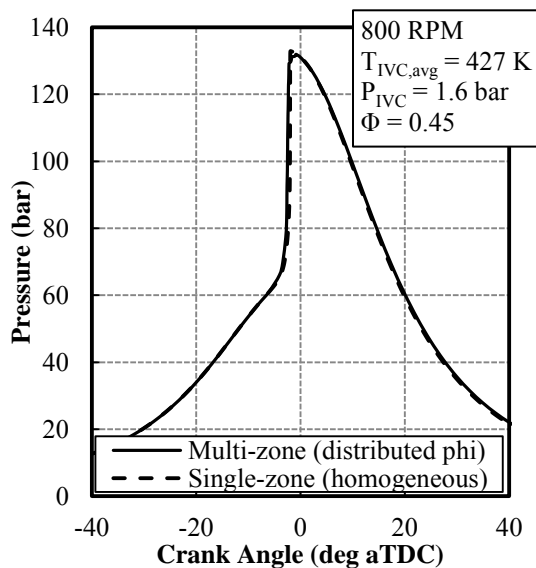
Fig.56 Predicted pressure as a function of crank angle from the single-zone and multi-zone with fuel concentration stratification only
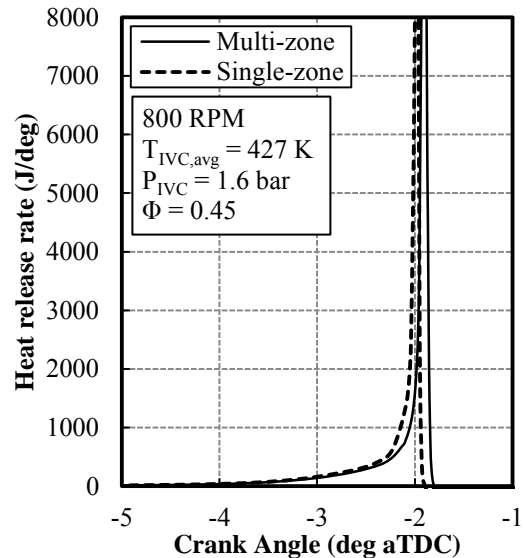
Fig.57 Predicted heat release rates as a function of crank angle from the single-zone and multi-zone with fuel concentration stratification only
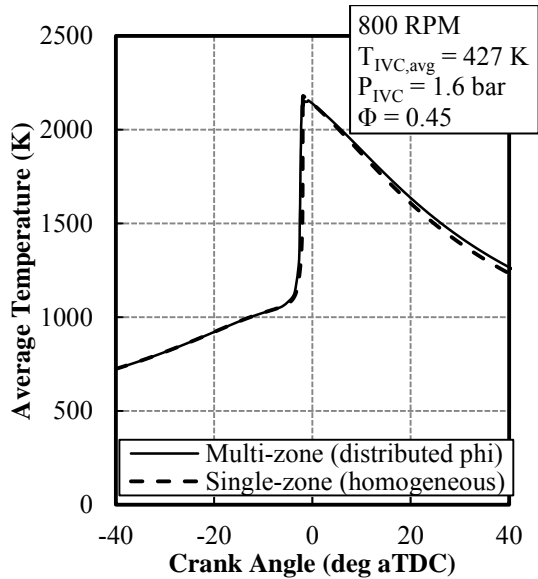
Fig.58 Predicted temperature as a function of crank angle from the single-zone and multi-zone with temperature stratification only
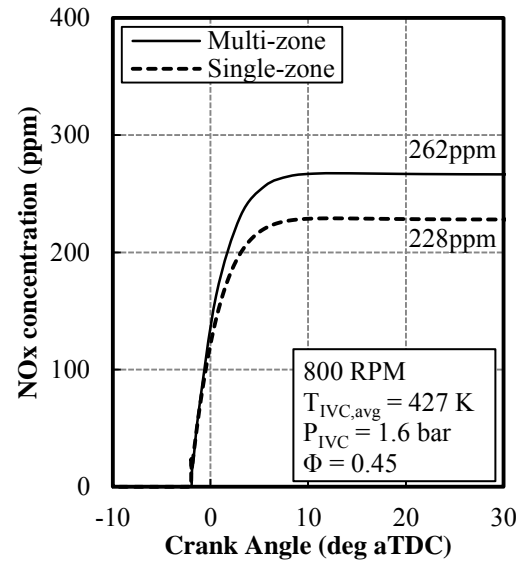
Fig.59 Predicted NO$_x$ emissions as a function of crank angle from the single-zone and multi-zone with temperature stratification only
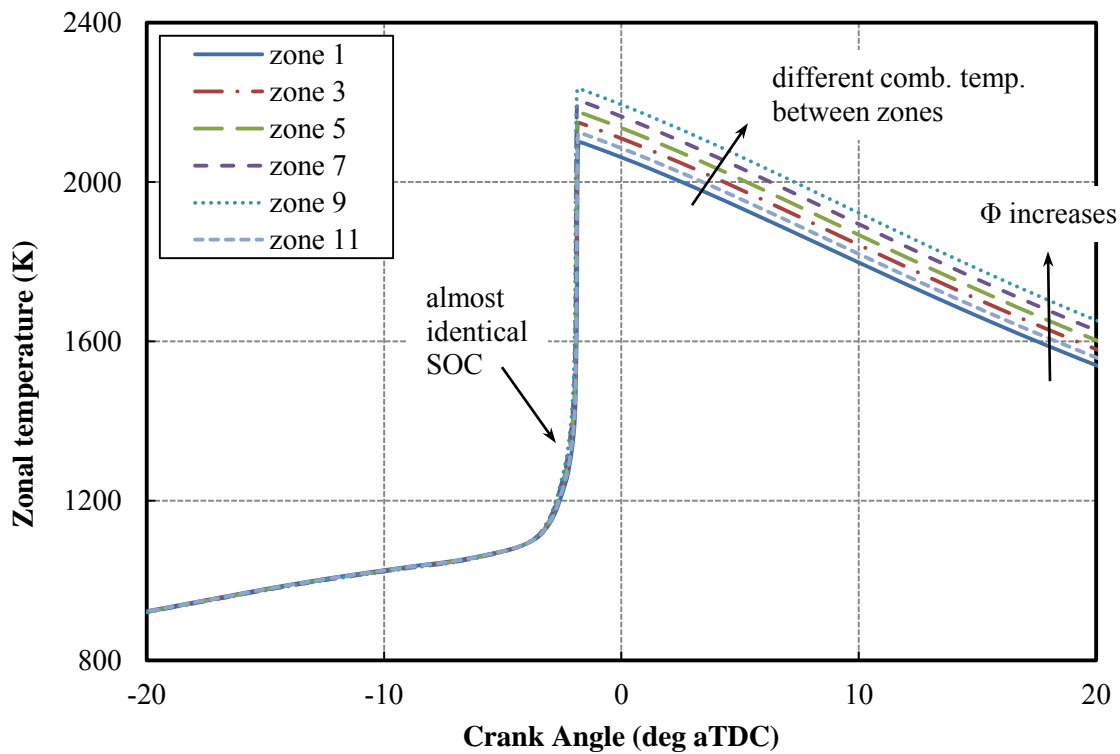
Fig.60 Zonal temperature as a function of crank angle for the multi-zone model with Φ distribution only RPM=800, Φ$_{avg}$ = 0.45, T$_{IVC,avg}$=427 K, and P$_{IVC}$=1.6 bar

Figure 61 compares the CO, UHC, and NO$_x$ predictions from the different models with the experimental measurements from Jun et al. [28]. The CO and UHC predictions from single-zone model and multi-zone with phi distribution only are almost zero. The results from the multi-zone with temperature distribution only start to reflect some CO and UHC emissions, mainly from the misfired zones mentioned earlier. But the absolute value of the CO and UHC predictions are still much lower than the experimental data. This is because not all the crevices such as the piston ring gaps are included in the model and lots of CO and UHC are formed in these crevices in real engine. In addition, in the experiment the combustion rate is lower than the predictions, shown as lower pressure rise rate in figure 7, and a higher percent of the fuel species are partially oxidized to CO and UHC due to the low combustion temperature. In terms of the NO$_x$ emissions, the measurement shows very low NO$_x$ concentration. The discrepancies between the models and the measurements are still mainly due to the differences in the temperature and combustion rate. The models over-predicted the combustion rate which then leads to a higher gas temperature and higher NO$_x$ concentration. Again, the multi-zone model with temperature distribution only shows better capability approaching the experimental value than the other two models. More calibrations specific for NO$_x$ emissions could improve the agreement with the experimental data.
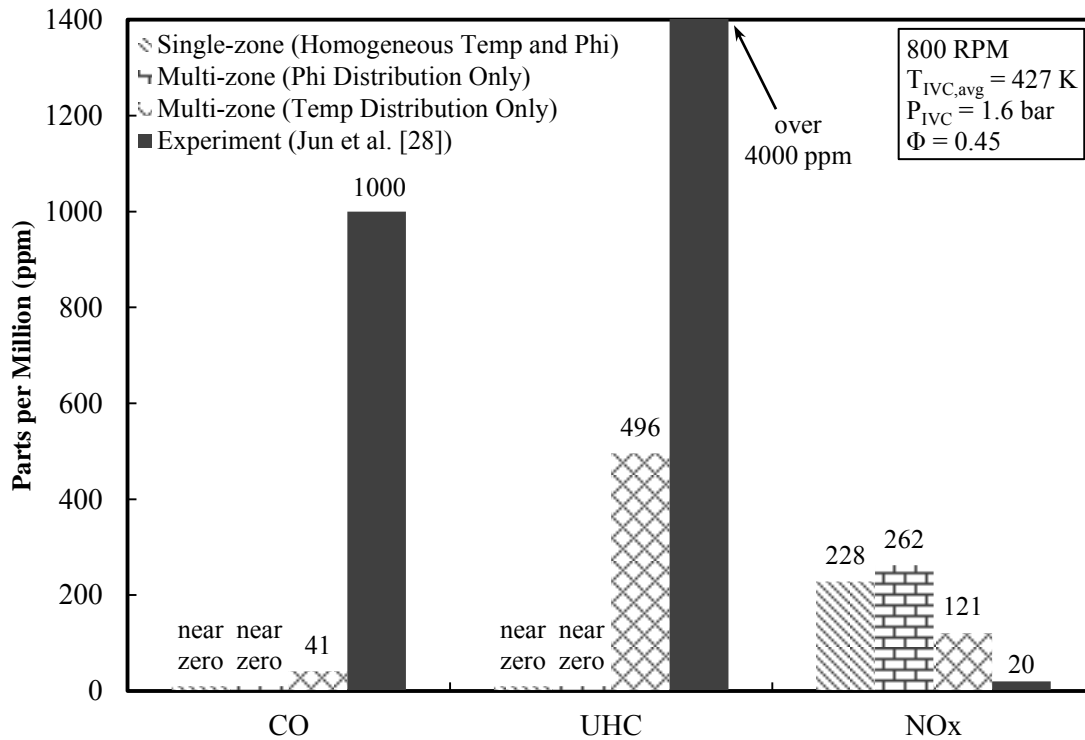
Fig.61 Comparison of the emission predictions and measurements

6.3 Results from two-dimensional combustion CFD simulations

In this sub-section, contour plots obtained from the two-dimensional combustion CFD simulations are shown and discussed for the natural gas HCCI combustion process.

The currently used boundary and initial conditions of the CFD model are shown in figure 62. Figures 63-68 show the contour plots at a few crank angles for the HCCI combustion of natural gas, including the mole fraction of CH_4, C_2H_6, CO, and NO, heat release, and temperature.
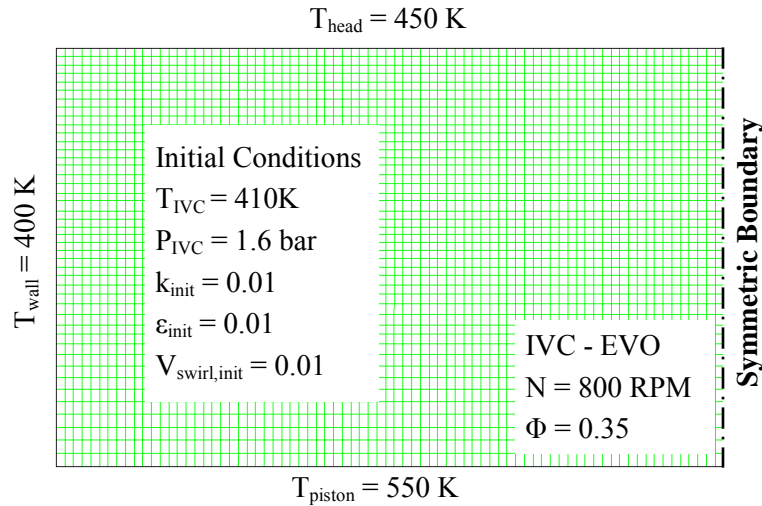
Fig.62 The boundary and initial conditions of the 2-D combustion CFD model

Figure 63 shows the evolution of CH_4 mole fraction contour in the combustion chamber as a function of crank angle from -1.0 deg aTDC to 4.5 deg aTDC. Figure 64 shows the evolution of C_2H_6 mole fraction during the same period. As can be seen in these two figures, during the early stage of ignition, methane and ethane start to be oxidized gradually in the center which has the highest temperature in the cylinder. Ethane is oxidized slightly earlier than methane and helps building up the radical pool for the fast explosion later on. As the ignition is initiated, methane in the center is quickly consumed and releases lots of heat energy which builds up the high temperature center as seen in the following heat release and temperature contours. As the combustion continues, colder regions near the walls are heated by the convection with hot center regions, and the methane mass in those zones start to react until all of them are oxidized or temperature becomes too low to sustain the oxidation as the expansion goes on.

Figures 65 and 66 show the temperature and heat release contours from -1.0 to 5.0

deg aTDC. The temperature quickly builds up from the center to the cylinder walls as a lot of heat is released due to the combustion reactions. The majority of the heat release occurs in a very short period, approximately from 0.5 to 2.5 deg aTDC. The pattern of the heat release is very close to the change in the mole fraction of methane and ethane described earlier.

Figure 67 shows the mole fraction of NO contours from -1.0 to 12.0 deg aTDC. The NO formation is obviously lagged behind the temperature build-up by 2-4 degrees in crank angle. The highest NO concentration exists in the center of the cylinder where the temperature is higher. These observations indicate that the thermal mechanism, which requires relatively long residence times, still dictates the NO formation.

Figure 68 shows the mole fraction of CO contours from -1.0 to 4.0 deg aTDC. A lot of CO builds up around 0.5 deg aTDC and a lot of heat is released when the CO is oxidized to CO_2 shortly. As the main combustion and heat release process is ending, CO is still forming and staying in the corner of the chamber where the temperature are relatively low due to the heat loss to the walls. Finally the CO in these regions will contribute to the CO emissions if they are not oxidized later in the expansion stroke.
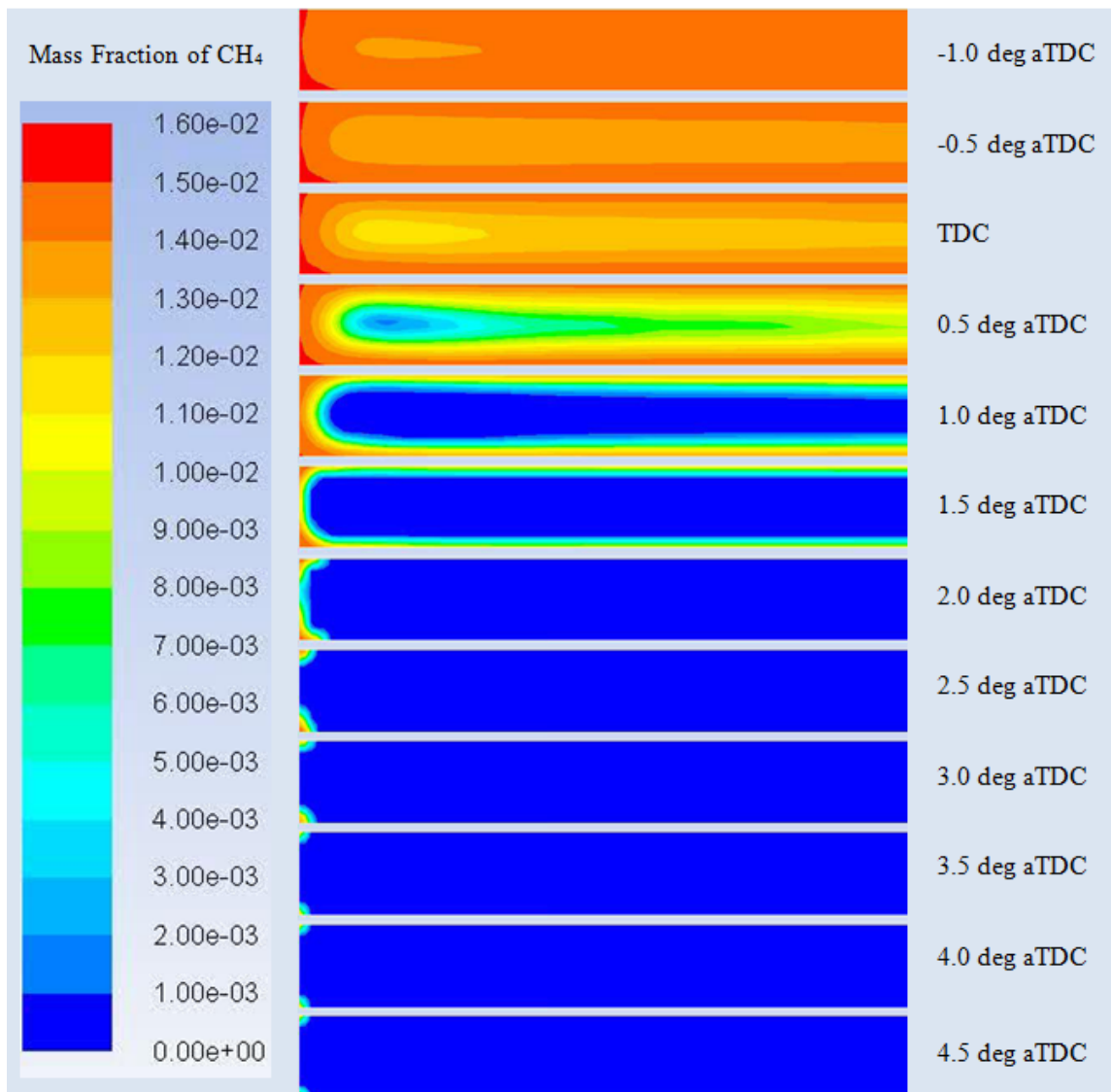
Fig.63 In-cylinder distribution of mass fraction of methane (CH₄) during the natural gas HCCI combustion from CFD model with Gri-mech 3.0 kinetics
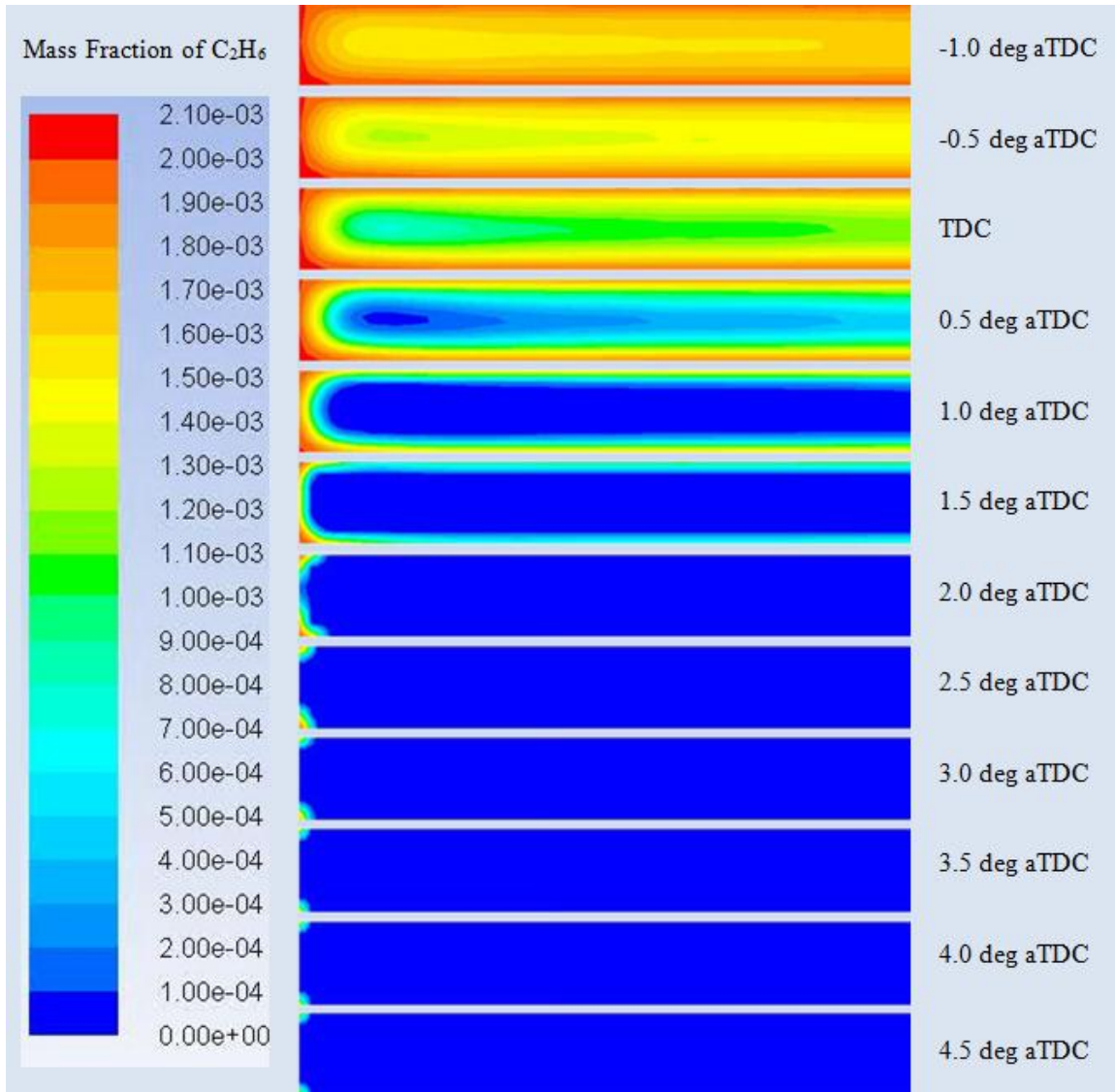
Fig.64 In-cylinder distribution of mass fraction of ethane (C_2H_6) during the natural gas HCCI combustion from CFD model with Gri-mech 3.0 kinetics
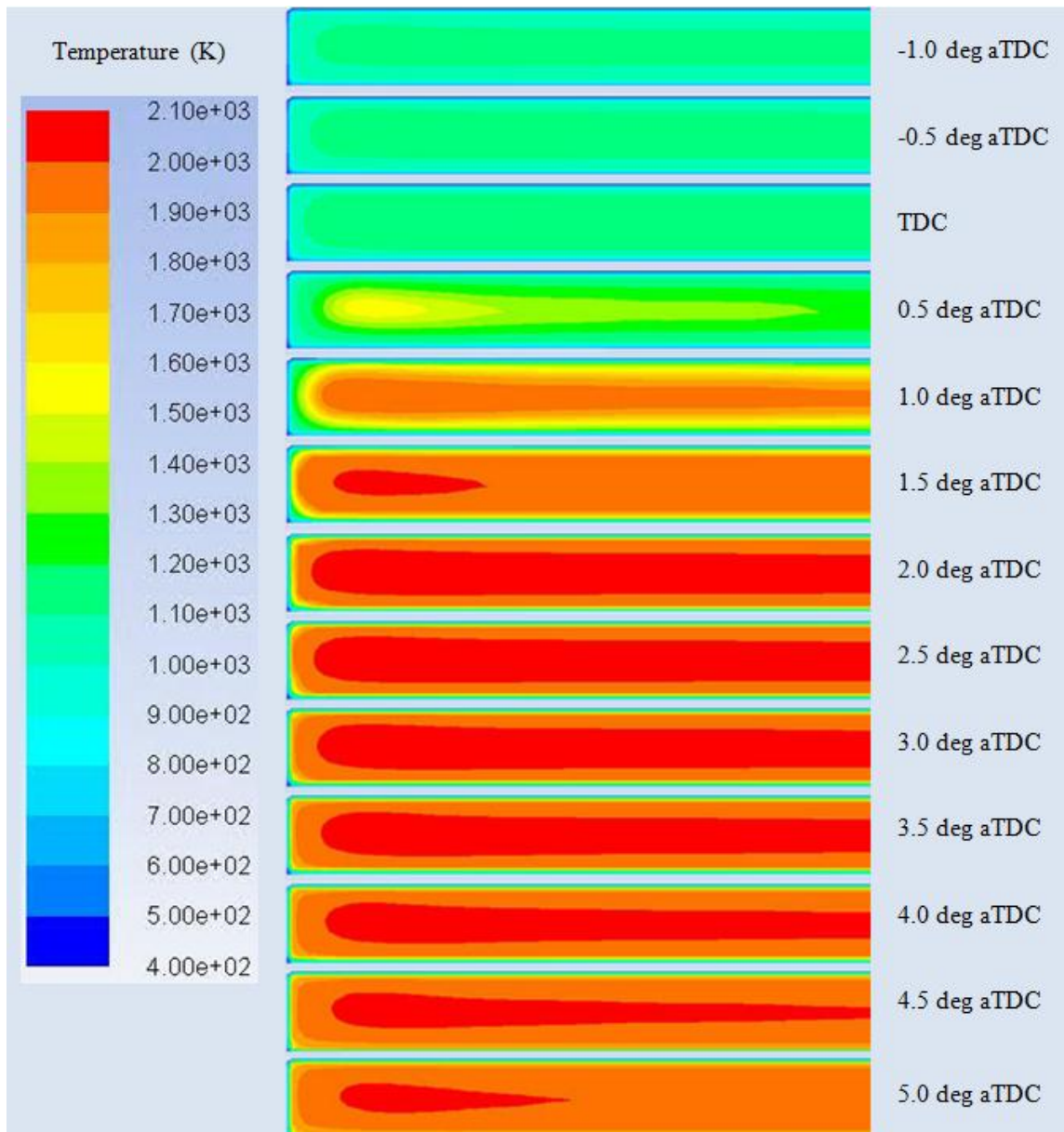
Fig.65 In-cylinder distribution of temperature during the natural gas HCCI combustion from CFD model with Gri-mech 3.0 kinetics
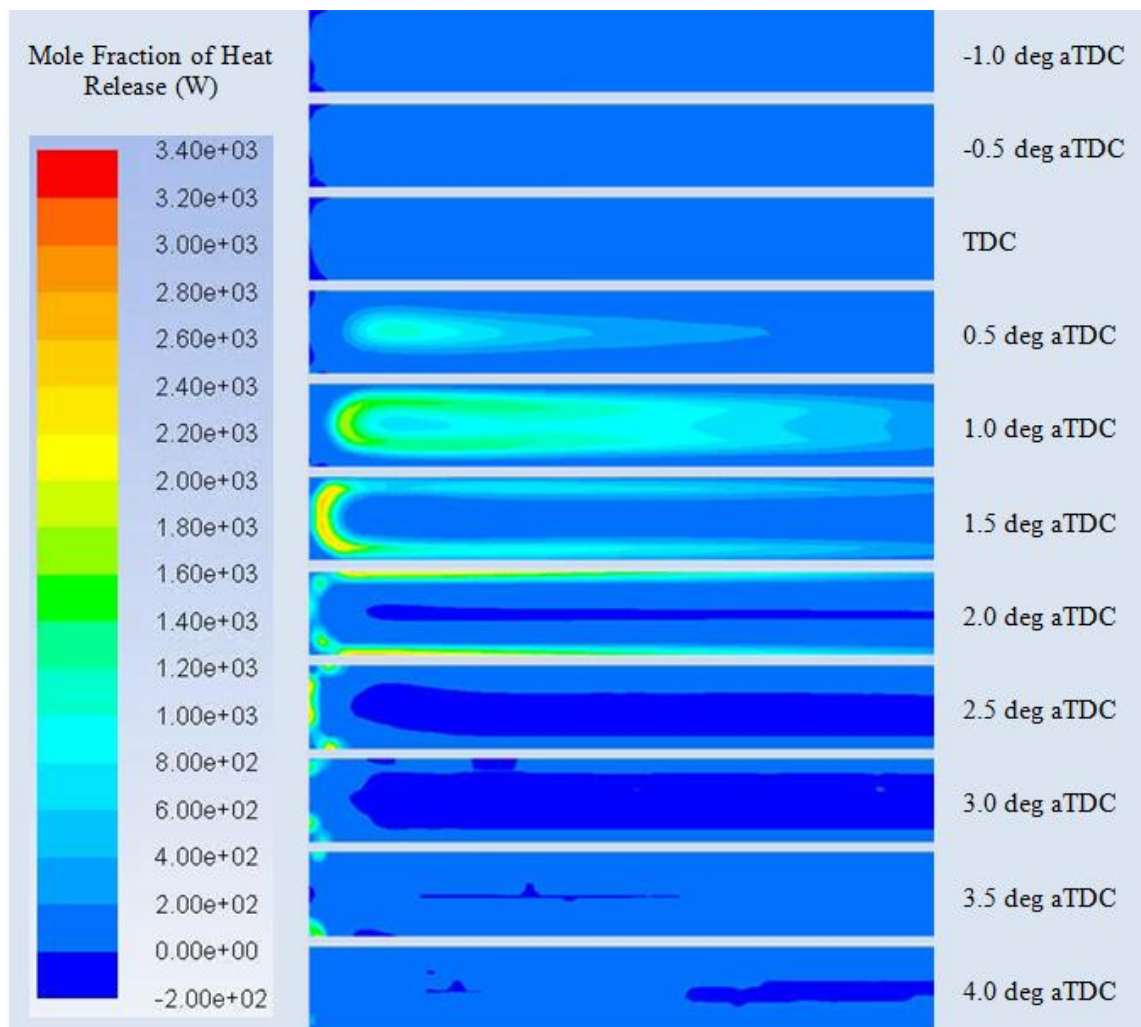
Fig.66 In-cylinder distribution of heat release during the natural gas HCCI combustion from CFD model with Gri-mech 3.0 kinetics
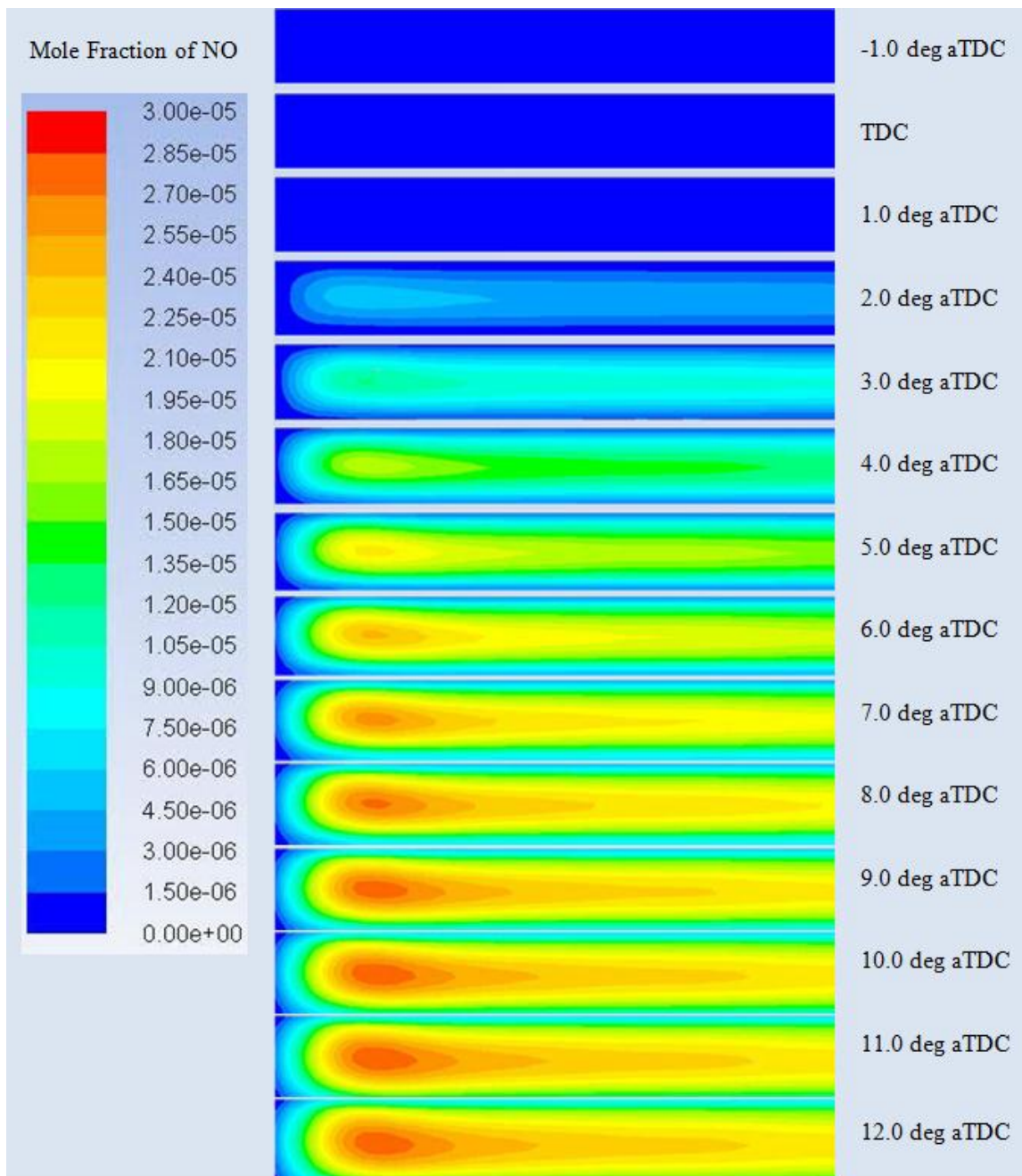
Fig.67 In-cylinder distribution of mole fraction of NO during the natural gas HCCI combustion from CFD model with Gri-mech 3.0 kinetics
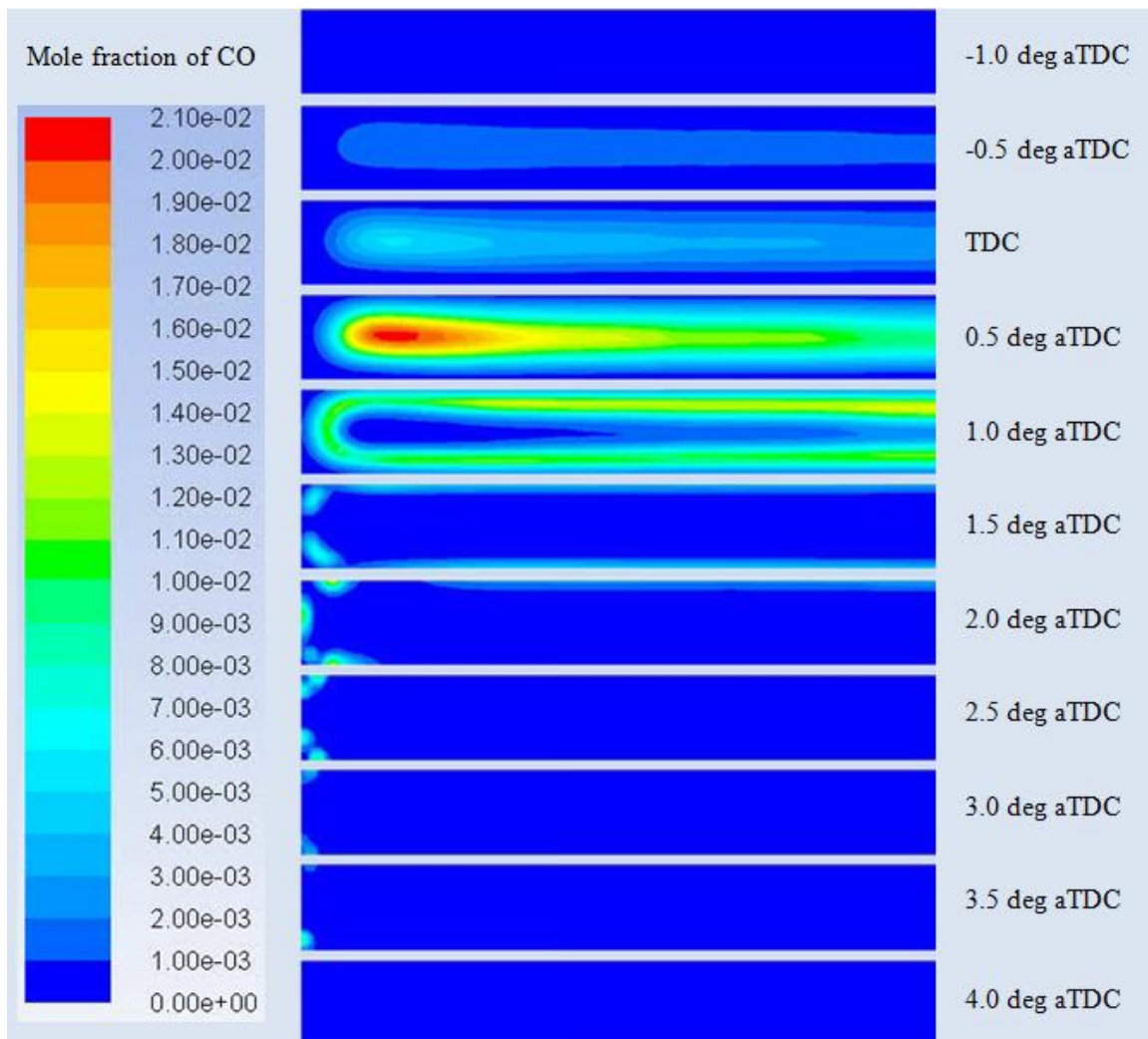
Fig.68 In-cylinder distribution of mole fraction of CO during the natural gas HCCI combustion from CFD model with Gri-mech 3.0 kinetics

7. SUMMARY AND CONCLUSIONS

A single-zone model, a multi-zone model, and a two-dimensional computational fluid dynamics model have been developed and employed to study the potential of using natural gas in HCCI engines. The three models first were calibrated and validated by comparing the predicted pressure profiles with the measurements. The observations and conclusions from the three models are summarized as follows.

Using the single-zone model, the effect of operating conditions on the ignition characteristics, engine performance, thermal efficiency, and NO_x emissions of the HCCI engine has been determined. The results for using natural gas, gasoline, DME, and natural gas/DME blends as the fuel have been compared and discussed. Some of the conclusions are:

1. The operating conditions, including equivalence ratio, engine speed, and intake pressure, have great influences on the HCCI ignition characteristics. The $T_{IVC,min}$ (minimum required temperature at IVC) for auto-ignition and complete combustion, decreases as the equivalence ratio increases and the intake pressure increases, and increases as the engine speed increases. In addition to the operating conditions, compression ratio has an even greater effect on $T_{IVC,min}$. For the natural gas case, the increase in compression ratio from 18 to 22 could reduce the requirement of $T_{IVC,min}$ by 40K. The results implies that to reduce the intake temperature requirement for using

natural gas, higher compression ratio, intake boosting, and relative lower engine speed are desirable.

2. The operating conditions also have great effect on the HCCI engine performance and efficiencies. The volumetric efficiency increases with the increase of equivalence ratio or intake pressure, or the decrease of engine speed or exhaust gas recirculation level. The indicated thermal efficiency peaks at a certain equivalence ratio, and a higher or lower equivalence ratio than this value will decrease the indicated efficiency. The increase in engine speed improves the indicated efficiency while the change in intake pressure and EGR level doesn't have a strong influence on the efficiency. In terms of the volumetric efficiency, intake boosting is a very desirable option to increase the specific power output, and operating at high engine speed is not attractive as it deteriorates the volumetric efficiency. In terms of the indicated efficiency, operating with a relatively lean mixture is still a desirable option for natural gas HCCI engines.

3. The NO_x emissions of the HCCI engine are greatly increased as the equivalence ratio increases or the EGR level decreases. The increase in the engine speed or the intake pressure slightly increases the NO_x emission. Through the study of different NO mechanisms, it is observed that most of the NO (over 70% at most of the conditions) still comes from thermal mechanism in HCCI engines. The increase in intake pressure will make the nitrous oxide intermediate mechanism more important and the increase in the

equivalence ratio toward one will enhance the prompt mechanism.

4. The comparison of natural gas, gasoline, and DME shows that the use of natural gas in HCCI engines requires the highest intake temperatures at IVC to ensure auto-ignition and to reach the best efficiency point. The $T_{IVC,min}$ and $T_{IVC,beff}$ for natural gas are typically 60-100K higher than those for gasoline. Dimethyl ether is very easy to auto-ignite and needs no intake heating at most of the operating conditions. The characteristics of gasoline lie between these two. So adding DME into natural gas greatly reduces the intake temperature requirements. Natural gas with 10% of DME addition in volume requires 20-60K less in $T_{IVC,beff}$ depending on the operating conditions. Furthermore, natural gas blending with DME reduces the NO_x emission as a result of the decreased temperature.

The results from the non-reacting CFD simulation and the multi-zone simulations show the effect of in-cylinder temperature and concentration distributions on HCCI combustion characteristics, such as ignition timing, combustion duration, and NO_x formation. Major observations are summarized below,

1. Both the temperature and equivalence ratio are not homogeneous in the combustion chamber. The results from the two-dimensional non-reacting CFD simulations indicates that the temperature ranges from 360K to 450K and the equivalence ratio ranges from

0.36 to 0.42 at the engine speed equal to 800 RPM, the inlet equivalence ratio equal to 0.45, the inlet temperature equal to 380, and the residual temperature equal to 800K. The change in operating conditions also will affect the distributions in temperature and equivalence ratio. Increasing the engine speed and the residual gas temperature will increase the average temperature in the cylinder and result in a more stratified temperature distribution. Similarly, the increase in inlet equivalence ratio will cause a more stratified concentration distribution.

2. In terms of the HCCI combustion, the stratification of the temperature will advance the ignition timing, extend the combustion duration, and reduce the peak temperature and pressure. The zones with higher temperature will auto-ignite earlier and have higher combustion temperature than the average, while some zones with low temperature will misfire and produce a lot of HC and CO emissions. This implies that introducing temperature stratifications helps to reduce the intake temperature requirement of using natural gas in HCCI engines, and reduces combustion noise. The NO_x prediction is lower for the case with temperature stratifications than the homogeneous case due to the decrease in the average temperature. This decrease in the average temperature is caused by the misfire of those coldest zones.

3. The stratification of the concentration, i.e. equivalence ratio in the current study, doesn't have a strong effect on the HCCI combustion characteristics. The zones with the

same temperature and small difference in the equivalence ratio, the difference of 0.02 as observed, have almost the same combustion phasing. With the equivalence ratio stratification only, the predicted pressure and average temperature are very similar to the single-zone results. The NO_x prediction, however, is higher due to the non-linear effect of temperature on the NO_x formation.

The use of the two-dimensional combustion CFD model enables the visualization of the HCCI ignition and combustion process in the contour plots, including the temperature, species concentration, and heat-release contours. By looking at the heat-release contour plot, it is observed that significant amount of the reaction heat is first released in the center of the combustion chamber where the highest temperature exists and the combustion is initiated. Then the combustion energy is released in the surroundings as the air/fuel mixture is heated up by the initial heat release and is oxidized in the following. Other contour plots, such as the oxidation of methane, temperature, CO and NO_x formation, follow the similar pattern as the heat release contour.

8. RECOMMENDATIONS

The recommendations for future research work concerning the modeling of natural gas HCCI engines are summarized as follows,

1. For the multi-zone model, the number of zones has certain effect on the simulation results as well as the simulation time. Efforts could be made to optimize the number of zones to achieve fastest simulation while maintaining reasonable accuracy.

2. For the computational fluid dynamics simulations, currently two-dimensional geometry is used due to the limitation of the computational time and resources. When supercomputing is available and the computation time is not a crucial factor, three-dimensional geometry could be used to achieve the better accuracy and better reflect the real physics. Furthermore, with more powerful computing capability detailed chemical kinetics could be coupled with the fluid dynamics instead of using reduced mechanism in the current study. In particular, the turbulence-chemistry interaction could be included to gain more insight into the HCCI combustion process.

3. One of the major challenges of HCCI engines is to control the ignition and combustion process since there is no direct control device such as spark plug or high pressure injector. So the HCCI engine model could also be used for the control scheme development. In

this case, the simulation time should be carefully controlled. Very likely more assumptions and simplifications would be made to make models more efficient for control purpose.

4. Engine system simulation could be further developed to study the characteristics of the complete natural gas HCCI engine system. It could include fuel delivery system, intake and exhaust system, external EGR system, intake heating devices, exhaust after-treatment system, and etc.

REFERENCES

1   Energy Information Agency, International Energy Outlook 2011, available: http://www.eia.gov/forecasts/ieo/index.cfm, accessed: 01/14/2012.

2   Union Gas Limited, Chemical composition of natural gas, available: http://www.uniongas.com/aboutus/aboutng/composition.asp, accessed: 01/14/2012.

3   **Noda, T., Foster D.E.** A Numerical Study to Control Combustion Duration of Hydrogen-Fueled HCCI by Using Multi-zone Chemical Kinetics Simulation. SAE paper 2001-01-0250, 2001.

4   **Dec, J. E., Sjöberg, M.** A Parametric Study of HCCI Combustion - the Sources of Emissions at Low Loads and the Effects of GDI Fuel Injection. SAE paper 2003-01-0752, 2003.

5   **Jun, D., Ishii, K., Lida, N.** Combustion analysis of natural gas in a four-stroke HCCI engine using experiment and elementary reactions calculation. SAE paper 2003-01-1089, 2003.

6   **Ricklin, P. U., Kazakov, A., Dryer, F. L., Kong, S. C., Reitz, R.D.** The Effect of NOx Addition on the Auto Ignition Behavior of Natural Gas under HCCI Conditions. SAE paper 2002-01-1746, 2002.

7   **Flowers, D., Aceves, S., Westbrook, C. K., Smith, J.R., Dibble, R.** Detailed Chemical Kinetic Simulation of Natural Gas HCCI Combustion: Gas Composition Effects and Investigation of Control Strategies. *ASME Journal of Gas Turbines and Power*, 2001, **123**(1), 433-439.

8   **Guo, H., Neill, W. S., Chippior, W., Li, H., Taylor, J. D.** An Experimental and Modeling Study of HCCI Combustion Using n-Heptane. *ASME Journal of Gas Turbines and Power*, 2010, **132**(1), 022801.

9   **Bhave, A., Balthasar, M., Kraft, M., Mauss, F.** Analysis of a natural gas fuelled HCCI engine with EGR using a stochastic reactor model. *International Journal of Engine Research*, 2004, **5**(1), 93-104.

10 **Grenda, J. M.** Numerical Modeling of Charge Stratification for the Combustion Control of HCCI Engines. SAE paper 2005-01-3722, 2005.

11 **Machrafi, H., Cavadiasa, S., Guibert, P.** An experimental and numerical investigation on the influence of external gas recirculation on the HCCI autoignition process in an engine, thermal diluting, and chemical effects. *Combustion and Flame*, 2005, **155**(3), 476-489.

12 **Noel, L., Maroteaus, F., Ahmed, A.** Numerical Study of HCCI Combustion in Diesel Engines Using Reduced Chemical Kinetics of N-Heptane With Multidimensional CFD Code. SAE paper 2004-01-1909, 2004.

13 **Amano, T., Morimoto, S., Kawabata, Y.** Modeling of the Effect of Air/Fuel Ratio and Temperature Distribution on HCCI Engines. SAE paper 2001-01-1024, 2000.

14 **Aceves, S., Flowers, D., Espinnosa-Loza, F., Martinez-Frias, J., Dec, J. E., Sjoberg, M., Dibble, R., Hessel, R. P.** (2004). Spatial Analysis of Emissions Sources for HCCI Combustion at Low Loads Using a Multi-zone Model. SAE paper 2004-01-1910, 2004.

15 **Tominaga, R., Morimoto, S., Kawabata, Y., Matsuo, S., Amano, T.** Effects of Heterogeneous EGR on the Natural Gas Fueled HCCI Engine Using Experiments, CFD and Detailed Kinetics. SAE paper 2004-01-0945, 2004.

16 **Babajimopoulos, A., Lavole, G. A., Assanis, D. N.** Modeling HCCI Combustion With High Levels of Residual Gas Fraction - A Comparison of Two VVA Strategies. SAE paper 2003-01-3220, 2003.

17 **Fiveland, S. B., Agama, R., Christensen, M., Johansson, B., Hiltner, J., Mauss, F., Assanis, D. N.** Experimental and Simulated Results Detailing the Sensitivity of Natural Gas HCCI Engines to Fuel Composition. SAE paper 2001-01-3609, 2001.

18 **Kongsereeparp, P., Checkel, M. D.** Investigating the Effects of Reformed Fuel Blending in a Methane- or n-Heptane-HCCI Engine Using a Multi-Zone Model. SAE paper 2007-01-0205, 2007.

19 **Elkelawy, M., Yu-Sheng, Z., El-Din, H., Jing-zhou, Y.** A comprehensive Modeling Study of Natural Gas (HCCI) Engine Combustion Enhancement by Using Hydrogen Addition. SAE paper 2008-01-1706, 2008.

20 **Ng, C. and Thomson, M.** A Computational Study of the Effect of Fuel Reforming, EGR and Initial Temperature on Lean Ethanol HCCI Combustion. SAE paper 2004-01-0556, 2004.

21 **Mamlis, S., Nair, V., Andruskiewicz, P., Assanis, D., Wermuth, N., Najt, P.** Comparison of Different Boosting Strategies for Homogeneous Charge Compression ignition Engines. SAE paper 2010-01-0571, 2010.

22 **Kulzer, A., Lejsek, D., Nier, T.** A Thermodynamic Study on Boosted HCCI, Motivation, Analysis and Potential. SAE paper 2010-01-1082, 2010.

23 **Lee, Y. J., Huh, K. Y.** Simulation of HCCI combustion with spatial inhomogeneities via a locally deterministic approach. *International Journal of Automotive Technology*, 2010, **11**(1), 19-26.

24 **Kong, S., Reitz, R., Christensen, M., Johansson, B.** Modeling the Effects of Geometry Generated Turbulence on HCCI Engine Combustion. SAE paper 2003-01-1088, 2003.

25 **Kerschgens, B., Felsch, C., Vanegas, A., Peters, N.** Applying an Interactively Coupled CFD-Multi-Zone Approach to Study the Effects of Piston Bowl Geometry Variations on PCCI Combustion. *SAE Int. J. Engines*, 2009, **2**(1), 1793-1810.

26 CHEMKIN-PRO Theory Manual, 2010.

27 **Heywood, J. B.** *Internal Combustion Engine Fundamentals*, McGraw-Hill Book Company, New York, NY, 1988.

28 **Jun, D., Ishii, K., Iida, N.** Combustion Analysis of Natural Gas in a Four Stroke HCCI Engine Using Experiment and Elementary Reactions Calculation. SAE paper 2003-01-1089, 2003.

29 **Donato, N., Aul, C., Petersen, E., Zinner, C., Curran, H., Bourque, G.** Ignition and Oxidation of 50/50 Butane Isomer Blends. *Journal of Engineering for Gas Turbines and Power*, 2010, **132**(5), 051502.

30 **Smith, G. P., Golden, D. M., Frenklach, M., Moriarty, N. W., Eiteneer, B., Goldenberg, M., Bowman, C. T., Hanson, R. K., Song, S., Gardiner, Jr., W. C., Lissianski, V. V., Qin, Z.** Available: http://www.me.berkeley.edu/gri_mech/, accessed: 01/14/2012.

31 **Andrae, J. C. G., Brinckb, T., Kalghatgi, G. T.** HCCI experiments with toluene reference fuels modeled by a semidetailed chemical kinetic model. *Combustion and Flame*, 2008, **155**(7), 696-712.

32 **Zhao, Z., Chaos, M., Kazakov, A., Dryer, F. L.** Thermal decomposition reaction and a comprehensive kinetic model of dimethyl ether. *International Journal of Chemical Kinetics*, 2008, **40**(1), 1–18.

33 **Sivaramakrishnan, R., Brezinsky, K., Dayma, G., Dagaut, P.** High pressure effects on the mutual sensitization of the oxidation of NO and CH_4–C_2H_6 blends. *Physical Chemistry Chemical Physics*, 2007, **9**(11), 4230-4244.

34 **Stone, R.** *Introduction to Internal Combustion Engines*, MacMillan Press Ltd., London, UK, 1999.

35 **Correa, S. M.** A Review of NO_x Formation under Gas-Turbine Combustion Conditions. *Combustion Science and Technology*, 1992, **87**(5), 329-362.

36 **Bozzelli, J. W., Dean, A. M.** O+ NNH: A possible new route for NOx formation in flames. *International Journal of Chemical Kinetics*, 1995, **27**(9), 1097-1109.

37 **Konnov, A. A., Colson, G., De Ruyck, J.** New route forming NO via NNH. *Combustion and Flame*, 2000, **121**(1), 548–550.

38 **Konnov, A. A., De Ruyck, J.** A Possible New Route for NO Formation via N_2H_3. *Combustion Science and Technology*, 2001, **168**(1), 1-46.

39 **Annamalai, K., Puri, I. K.** *Combustion Science and Engineering,* CRC Press; 1st edition, 2006.

40 Engineering Tool Box, available: http://www.engineeringtoolbox.com/, assessed: 01/14/2012.

41 ANSYS Fluent Theory Guide, 2010.

NOMENCLATURE

aTDC	After Top Dead Center
A_i	Pre-exponential coefficient of the ith reaction
A/F	Air to fuel
B	Bore
$\bar{c}_p$	Specific heat at constant pressure
c_{pk}	Specific heat at constant pressure of the kth species
C1	Kinetics including only methane
C1-C4	Kinetics including methane, ethane, propane, and butane
CFD	Computational Fluid Dynamics
CH_4	Molecular formula of methane
C_2H_5OH	Molecular formula of ethanol
C_2H_6	Molecular formula of ethane
CH_3OCH_3	Molecular formula of dimethyl ether
C_3H_8	Molecular formula of propane
C_4H_{10}	Molecular formula of butane
$C_6H_5CH_3$	Molecular formula of toluene
$n\text{-}C_7H_{16}$	Molecular formula of n-heptane
$i\text{-}C_8H_{18}$	Molecular formula of iso-octane
CA	Crank Angle

CD	Combustion Duration
CI	Compression-Ignition
CNG	Compressed Natural Gas
CPU	Central Processing Unit
CO	Molecular formula of carbon monoxide
CO_2	Molecular formula of carbon dioxide
CV	Control Volume
deg	Degree
DME	Di-Methyl Ether
E_i	Activation energy of the ith reaction
EGR	Exhaust Gas Recirculation
EVO	Exhaust valve opening
FTP	Federal Test Procedure
$\bar{h}$	Mass averaged specific enthalpy
h_k	Specific enthalpy of the kth species
H_2	Hydrogen
H_2O	Water
H_f°	Enthalpy of formation at the standard condition
H_t	Sensible enthalpy
HCCI	Homogeneous Charged Compression Ignition
IC	Internal Combustion

IVC	Intake Valve Closing
IVO	Intake Valve Opening
k	Turbulence kinetic energy
k_{fi}	Forward rate constant of the ith reactions
k_{ri}	Reverse rate constant of the ith reactions
K_g	Total number of the species in the system
N	Engine speed
N_2	Nitrogen
NEDC	National Economic Development Council (British)
NG	Natural Gas
NO	Molecular formula of nitric oxide
NO_x	Mono-nitrogen oxides, i.e. nitric oxide and nitrogen dioxide
N_2O	Molecular formula of nitrous oxide
NTC	Negative Temperature Coefficient
NVO	Negative Valve Overlap
Nu	Nusselt number
O_2	Oxygen
OH	Hydroxyl radical
p	Instantaneous in-cylinder pressure (bar)
p_m	Motored cylinder pressure (bar)
P	Pressure (kPa or bar)

P_{in}	Intake manifold pressure
P_{IVC}	Pressure at IVC (kPa or bar)
Phi	Φ, equivalence ratio
ppm	Parts per Million
PRF	Primary Reference Fuel
$\dot{Q}_{loss}$	Heat loss from the hot gases to the cylinder wall
$\dot{Q}_{source}$	Heat generation due to the chemical reactions in the control volume
R_c	Universal gas constant
RANS	Reynolds Averaged Navier-Stokes equation
Re	Reynolds number
RG	Reforming gases
RPM	Revolution per Minute
S/B	Stroke to bore ratio
SI	Spark-Ignition
SOC	Start of Combustion
t	Time (s or ms)
T	Temperature (K or ˚C)
T_{in}	Intake manifold temperature
T_{IVC}	Temperature at IVC
$T_{IVC,avg}$	Averaged temperature at IVC in the multi-zone model

$T_{IVC,min}$	Minimum temperature at IVC for complete combustion
$T_{IVC,beff}$	Temperature at IVC for best indicated efficiency
T_R	Residual gas temperature
T_w	Wall temperature
TDC	Top Dead Center
v'_{ki}	Forward stoichiometric coefficient for the kth species in the ith reaction
v''_{ki}	Reverse stoichiometric coefficient for the kth species in the ith reaction
$\bar{v}_p$	Mean piston speed
v_{swirl}	Swirl velocity
V	Volume (m^3 or liter)
V_d	Displacement volume
U	Internal energy
UHC	Unburned hydrocarbon
w	Local average gas velocity
W_k	Molecular weight of the kth species in the system
x_k	Chemical symbol of the kth species in the system
X_k	Molar concentration of the kth species
Y_k	Mass fraction of the kth species in the system

Greek Letters

β Exponential index for the temperature term in Arrhenius expression

γ Ratio of specific heats

Φ Equivalence ratio

Φ_{in} Equivalence ratio in the intake manifold

ρ Density

$\dot{\omega}_k$ Molar rate of production of the kth species

μ Dynamic viscosity

ε Dissipation rate of the turbulence kinetic energy

Superscripts

i The ith zone in the multi-zone model

'   Forward direction of the reaction

"   Backward direction of the reaction

Subscripts

k The kth species in the system

w Wall

i The ith reaction in the system

r Reference state

APPENDIX I

DETAILED EQUATIONS IN THE MULTI-ZONE MODEL [26]

Species equation:

$$\rho^i \frac{dY_k^i}{dt} = \dot{\omega}_k^i W_k \qquad for \ i = 1, 2, .., N \ zones$$

Internal energy equation:

$$\rho^i \bar{c}_p^i \frac{dT^i}{dt} = -\sum_{k=1}^{K_g} \dot{\omega}_k^i W_k^i u_k^i - \frac{P^i}{V^i} \frac{dV^i}{dt} - \frac{h_w^i \left(T^i - T_w\right) A_w^i}{V^i} \qquad for \ i = 1, 2, .., N \ zones$$

New Variable G and the Equation of state:

$$G^i = \sum_j^i P^j V^j$$

$$P^i V^i = M^i R T^i \left(\sum_{k=1}^{K_g} \frac{Y_k^i}{W_k}\right)$$

$$\begin{cases} G^1 = P^1 V^1 & for \ i = 1 \\ G^i = G^{i-1} + M^i R T^i \left(\sum_{k=1}^{K_g} \frac{Y_k^i}{W_k}\right) & for \ i = 2, 3, ..., N \end{cases}$$

Uniform pressure constraint:

$$P^i = P^{i+1} \qquad for \ i = 1, 2, .., N-1$$

$$P^N = \frac{G^N}{\sum_{i=1}^N V^i}$$

These equations are solved simultaneously to obtain zone properties.

APPENDIX II

GOVERNING EQUATIONS FOR THE COMPUTATIONAL

FLUID DYNAMICS SIMULATION [41]

Continuity equation for 2-D axisymmetric geometries:

$$\frac{\partial \rho}{\partial t} + \frac{\partial}{\partial x}(\rho v_x) + \frac{\partial}{\partial r}(\rho v_r) + \frac{\rho v_r}{r} = S_m$$

Axial momentum equation for 2-D axisymmetric geometries:

$$\frac{\partial}{\partial t}(\rho v_x) + \frac{1}{r}\frac{\partial}{\partial x}(r\rho v_x v_x) + \frac{1}{r}\frac{\partial}{\partial r}(r\rho v_r v_x) = -\frac{\partial p}{\partial x} + \frac{1}{r}\frac{\partial}{\partial x}\left[r\mu\left(2\frac{\partial v_x}{\partial x} - \frac{2}{3}(\nabla \cdot \vec{v})\right)\right]$$
$$+ \frac{1}{r}\frac{\partial}{\partial x}\left[r\mu\left(\frac{\partial v_x}{\partial r} + \frac{\partial v_r}{\partial x}\right)\right] + F_x$$

Radial momentum equation for 2-D axisymmetric geometries:

$$\frac{\partial}{\partial t}(\rho v_r) + \frac{1}{r}\frac{\partial}{\partial x}(r\rho v_x v_r) + \frac{1}{r}\frac{\partial}{\partial r}(r\rho v_r v_r) = -\frac{\partial p}{\partial r} + \frac{1}{r}\frac{\partial}{\partial r}\left[r\mu\left(2\frac{\partial v_r}{\partial r} - \frac{2}{3}(\nabla \cdot \vec{v})\right)\right]$$
$$+ \frac{1}{r}\frac{\partial}{\partial x}\left[r\mu\left(\frac{\partial v_r}{\partial x} + \frac{\partial v_x}{\partial r}\right)\right] - 2\mu\frac{v_r}{r^2}(\nabla \cdot \vec{v}) + \rho\frac{v_{swirl}^2}{r} + F_r$$

Transport equation for the turbulence kinetic energy:

$$\frac{\partial}{\partial t}(\rho k) + \frac{\partial}{\partial x_i}(\rho k u_i) = \frac{\partial}{\partial x_j}\left[\left(\mu + \frac{\mu_t}{\sigma_k}\right)\frac{\partial k}{\partial x_j}\right] + G_k + G_b - \rho\varepsilon - Y_M + S_k$$

Transport equation for the rate of dissipation of turbulence kinetic energy:

$$\frac{\partial}{\partial t}(\rho\varepsilon) + \frac{\partial}{\partial x_i}(\rho\varepsilon u_i) = \frac{\partial}{\partial x_j}\left[\left(\mu + \frac{\mu_t}{\sigma_\varepsilon}\right)\frac{\partial \varepsilon}{\partial x_j}\right] + C_{1\varepsilon}\frac{\varepsilon}{k}(G_k + C_{3\varepsilon}G_b) - C_{2\varepsilon}\rho\frac{\varepsilon}{k} + S_\varepsilon$$

The energy equation with heat transfer and reaction heat:

$$\frac{\partial}{\partial t}(\rho E) + \nabla \cdot \left[\vec{v}(\rho E + p)\right] = \nabla \cdot \left[k_{eff}\nabla T - \sum h_k \vec{J}_k + \left(\bar{\bar{\tau}}_{eff} \cdot \vec{v}\right)\right] + S_h$$

The species transport equation:

$$\frac{\partial}{\partial t}(\rho Y_k) + \nabla \cdot (\rho \vec{v} Y_k) = -\nabla \cdot \vec{J}_k + R_k + S_k$$

VITA

Name: Junnian Zheng

Address: Texas A&M University
               Department of Mechanical Engineering
               3123 TAMU
               College Station, TX 77843-3123

Email: junnian.zheng@gmail.com

Education: B.A., Mechanical Engineering, Shanghai Jiao Tong University, 2007
               M.S., Mechanical Engineering, Texas A&M University, 2009
               Ph.D., Mechanical Engineering, Texas A&M University, 2012